

**Interplay between Piezo1-mediated mechanosensing and  
the chemical guidance cue Semaphorin3A during  
development of the embryonic nervous system**



**Eva K. Pillai**  
**St John's College**

**Department of Physiology, Development and Neuroscience**  
**University of Cambridge**  
**Supervisor: Dr Kristian Franze**

**This dissertation is submitted for the degree of Doctor of Philosophy**

**May 2020**

# *DECLARATION*

This dissertation is the result of my own work and includes nothing, which is the outcome of work done in collaboration except where specifically indicated in the text. It has not been previously submitted, in part or whole, to any university or institution for any degree, diploma, or other qualification.

In accordance with the guidelines of the Degree Committee of the School of Biological Sciences, this thesis does not exceed 60,000 words.

Signed:

Date: 11<sup>th</sup> May 2020

Eva K. Pillai  
Cambridge

Interplay between Piezo1-mediated mechanosensing and the chemical guidance cue Semaphorin3A during development of the embryonic nervous system

## SUMMARY

During nervous system development, growing neurons extend axons over long distances to defined targets. Despite decades of research dedicated to understanding how neurons are guided along the correct pathways, we still do not fully understand the mechanisms underlying axon pathfinding. In this project, I used the embryonic *Xenopus laevis* optic pathway as a model to study how axons navigate so precisely to their destination. Here, retinal ganglion cells (RGCs) send their axons out of the retina, to cross with axons of the opposite eye in the optic chiasm and continue their journey through the diencephalon as an optic tract, before reaching their target, the optic tectum. During formation of the optic tract, RGC axons respond to both chemical and mechanical signals in the environment. A key player in sensing mechanical cues is the mechanosensitive ion channel (MSC) Piezo1. Perturbations of Piezo1 resulted in aberrant axon guidance *in vivo*. When I studied Piezo1 downregulation further, I found that it regulates not only axon pathfinding but also mechanical tissue properties.

Tissue-specific downregulation of Piezo1 in either optic tract axons or in the surrounding neuroepithelia both resulted in optic pathway defects. The former suggests that Piezo1 is required by the axons themselves to sense physical cues from their environment. The latter suggests that non-cell autonomous processes are also mechanosensitive. Since Piezo1 is thought to respond exclusively to mechanical signals, I therefore set out to determine if tissue stiffness, cellular mechanosensing, or both were affected by Piezo1 downregulation.

I found that knocking down Piezo1 softened brain tissue, suggesting that the axons were encountering an environment with altered mechanical properties, and therefore mechanical signalling was affected. As I previously observed that cell body density scaled with tissue stiffness, I investigated if there was decreased cell body density in Piezo1 downregulated brain tissue but found that it was not significantly different from control brain tissue, suggesting that other factors were at play.

In addition to tissue softening, the downregulation of Piezo1 dramatically altered the expression of *semaphorin3A* mRNA (*sema3A*), a chemical guidance cue known to be critical in axon pathfinding. Thus, both chemical and mechanical signals encountered by the axons were altered when Piezo1 was less abundant in the brain. To determine if tissue softening was caused by decreased Sema3A expression, I downregulated Sema3A and measured brain mechanics. However, I found that tissue stiffness actually increased, suggesting that the tissue softening observed in Piezo1-depleted brains was not the result of decreased Sema3A. While decreasing or increasing tissue stiffness did not significantly alter *sema3A* levels *in vivo*, increasing substrate stiffness *in vitro* resulted in an increase in *sema3A* levels in culture neuroepithelia, suggesting that expression and availability of this signalling molecule may still be modulated by tissue mechanics.

My results suggest that Piezo1 plays critical cell autonomous and non-cell autonomous roles in axon guidance, and that perturbing this MSC results in alterations in both mechanical and chemical signalling. Furthermore, preliminary results suggest that mechanical signalling potentially regulates the transcription of chemical signalling molecules during development, implying that mechanical and chemical signalling are inextricably linked. This could have major implications for understanding the regulation of key biological processes in development, physiology, and pathophysiology.

# *LIST OF PUBLICATIONS*

*Pillai, E. K., Thompson, A. J., McGinn, R., Mooslehner, K., Franze, K.  
Piezo1-mediated mechanical regulation of the chemical guidance cue  
Semaphorin3A in nervous system development (in preparation).*

*Thompson, A. J. \*, Pillai, E. K. \*, Dimov, I. B., Foster, S. K., Holt, C. E., Franze,  
K. (2019). Rapid changes in tissue mechanics regulate cell behaviour in the  
developing embryonic brain. eLife 8, e39356*

*(\* these authors contributed equally to this work)*

*Koser, D.E., Thompson, A.J., Foster, S.K., Dwivedy, A., Pillai, E.K., Sheridan,  
G.K., Svoboda, H., Viana, M., Costa, L.D., Guck, J., Holt, C.E., Franze, K.  
(2016). Mechanosensing is critical for axon growth in the developing brain.  
Nature Neuroscience 19, 1592-1598.*

# *ACKNOWLEDGEMENTS*

I would like to thank my supervisor, Kristian, for making this project possible and for his guidance and dedication throughout this process. He has been extraordinarily encouraging and supportive, both academically and pastorally. Kristian, thank you for keeping a sense of humour when I sometimes lost mine.

I am grateful to my advisor Nick Brown for his support, and for the many useful scientific discussions we had. I would also like to thank Christine Holt for her time, advice and expertise throughout this PhD.

Past and present members of the Franze lab were a delight to work with and brilliant to learn from:

Francesco Barone, Julia Becker, Lars Bollman, Alejandro Carnicer-Lombarte, Andrea Dimitracopoulos, Ivan Dimov, Sarah Foster, H el ene Gautier, Ryan Greenhalgh, Maximilian Jakobs, Eva Kreysing, David Mafullul, Ross McGinn, Rachel Mckeown, Katrin Mooslehner, Sudipta Mukherjee, Rasha Rezk, Johannes Rheinlander, Rajesh Shahapure, Jana Sipkova, Vanesa Sokleva, Joy Thompson, Isabel Weber, Liz Williams, Omer Wagner, Alex Winkel.

I would like to especially acknowledge:

- Sarah, Joy, Max, Philippe Bujold, Julia, Jana, and Ryan for proofreading sections of this thesis.
- Katrin and Alex for their molecular biology and AFM help. Also, Katrin and Ross for being extra pairs of (skilled) hands when I was injured.
- Joy for Amelia-rating the long AFM sessions and being a Joy to work with.
- Sarah for Fostering my scientific growth, and for many instances of help and kindness throughout this journey.
- Liz for keeping the lab running smoothly and, for the wisdom and warmth of her friendship.
- Max for Aloys being there for me: for being a scientific sounding board and for the friendship and love.

I would like to also thank the Harris/Holt lab for generously sharing their equipment and expertise with me. I am particularly indebted to Asha Dwivedy for sharing her incredible wealth of *Xenopus* technique knowledge, and must also thank Toshiaki Shigeoka, Hovy Wong, Julie Lin, Jean-Michel Cioni, and Max Koppers.

I am grateful to Rue Jones and Tomasz Dyl for the excellent frog care and would also like to thank various members of PDN for sharing their expertise, especially Martin Minarik (Baker Lab) and the people at the Cambridge Advanced Imaging Centre (CAIC).

Finally, the CSHL *Xenopus* folk were instrumental in schoolin' me in the ways of the frog.

Outside of science, I must thank many wonderful people for their support and love throughout my PhD:

My parents, Kanagesvaran Thuraiappah and Lucy Barrock, for encouraging the curiosity, being supportive, and always celebrating my endeavours. My siblings, Tharun and Yovin(a) for inspiring me with the courage of their convictions. Sri Nithyananda Paramashivam and Ma NithyaAtmadayananda, for being there for me. My aunt, Leela Barrock, for her guidance and backing before and during my time in Cambridge. Rahel Barrock for being a ray of sunshine. Elisha Chng (RIP), Suman Pillai (RIP), and various members of my extended family, whose life journeys inspired my interest in neuroscience.

Philippe Bujold for being the best other person in our two people cohort. Emilija Leinarte and Isabella Gariboldi. whose exuberance of spirit and many coffees and teas sustained me in Cambridge. Julia Faló-Sanjuan and the rest of the Happy Hour crew for bringing beers and cheer to PDN. Chathuri Dissanayake and Anitha Andiappan for their friendship. Alexander Yap, Andrew Pereira, Choo Ben Luke, and Lee Su Yee for keeping me on my toes and being a mere phone call away. Andrea (DM extraordinaire), Jana, Max, Susie McLaren, Francesco, and Alex Campbell for being the sort of D&D group that would keep everyone (but Francesco) alive. Kevin Chalut, whose advice led to the fruition of my studentship with Kristian. The Maypole, where it all began.

Dr David Stuart, my college tutor, and Mrs Aileen Jordan, the PDN Graduate Administrator, for exceptional pastoral care and support throughout this PhD. Allan and Marilyn Treacy who have been very kind and helpful in this time. Dr Anil Seal and the Malaysian Commonwealth Studies Centre for the generous funding.

# CONTENTS

<b>1 INTRODUCTION .....</b>	<b>1</b>
1.1 MAKING AND CONNECTING AN EMBRYONIC BRAIN.....	1
1.2 AXON GROWTH AND GUIDANCE (THE MACHINERY).....	2
1.3 CHEMICAL GUIDANCE CUES IN AXON PATHFINDING.....	3
1.3.1 <i>Semaphorin3A</i> .....	6
1.4 THE MECHANICAL ENVIRONMENT OF A NEURON .....	13
1.4.1 <i>Mechanics of materials</i> .....	13
1.4.2 <i>Mechanical cues in axon guidance</i> .....	14
1.4.3 <i>Mechanics in neuronal development, growth, and connectivity</i> .....	15
1.4.4 <i>Cellular mechanosensing and transduction</i> .....	16
1.4.5 <i>Piezo1</i> .....	17
1.5 THE <i>XENOPUS LAEVIS</i> RETINOTECTAL SYSTEM AS MODEL OF AXON GROWTH AND PATHFINDING.....	23
1.5.1 <i>Journey to the tectum: the growth of RGC axons</i> .....	23
1.5.2 <i>Chemical guidance of Xenopus RGC axons</i> .....	24
1.5.3 <i>Mechanosensitivity of Xenopus RGC axons in vitro</i> .....	27
1.5.4 <i>In vivo brain mechanics</i> .....	29
1.5.5 <i>Mechanosignalling via Piezo1 is crucial in in vivo axon pathfinding</i> .....	33
1.6 AIM OF THIS STUDY.....	35
<b>2 METHODS .....</b>	<b>37</b>
2.1 MANIPULATING THE <i>XENOPUS</i> EMBRYO .....	37
2.1.1 <i>Xenopus husbandry</i> .....	37
2.1.2 <i>Exposed brain preparation of Xenopus embryos</i> .....	37
2.1.3 <i>In vivo chemical treatments</i> .....	38
2.1.4 <i>In vivo eye primordia ablation</i> .....	39
2.1.5 <i>In vitro eye primordia cultures</i> .....	39
2.1.6 <i>In vitro neuroepithelia cultures</i> .....	40
2.1.7 <i>Translation blocking by morpholino blastomere injections</i> .....	40
2.1.8 <i>Visualising the optic tract in intact brains</i> .....	42
2.1.9 <i>Cryosectioning Xenopus embryos</i> .....	43
2.1.10 <i>Brain targeted electroporation</i> .....	43
2.2 ALTERING AND MEASURING THE MECHANICAL ENVIRONMENT .....	44
2.2.1 <i>Compliant tissue culture substrate (hydrogel) fabrication</i> .....	44
2.2.2 <i>Atomic Force Microscopy Measurements</i> .....	45
2.3 RNA VISUALIZATION AND QUANTIFICATION .....	47
2.3.1 <i>Preparation of Digoxegenin-labelled RNA probes</i> .....	47

2.3.2 RNA synthesis of probe .....	48
2.3.3 Whole embryo in situ hybridization.....	49
2.3.4 Whole brain in situ hybridization.....	50
2.3.5 Quantitative polymerase chain reaction (qPCR) .....	51
2.4 PROTEIN QUANTIFICATION AND VISUALIZATION .....	54
2.4.1 Western blots.....	54
2.4.2 Wholemount brain immunohistochemistry .....	55
2.4.3 Immunohistochemistry tissue cross-sections .....	55
2.4.4 Immunocytochemistry of RGC axons in vitro .....	56
2.5 ANALYSIS.....	58
2.5.1 OT phenotype analysis.....	58
2.5.2 OT elongation analysis .....	58
2.5.3 AFM data analysis.....	58
2.5.4 In situ hybridization.....	59
2.5.5 Analysis of the brain cross-section .....	60
2.5.6 Cell body density analysis.....	60
2.6 STATISTICS .....	61
<b>3 PIEZO1 IN THE XENOPUS EMBRYONIC BRAIN .....</b>	<b>63</b>
3.1 PIEZO1 IS FOUND IN NEUROEPITHELIA .....	63
3.2 PIEZO1 IS FOUND IN RGC AXONS .....	63
3.3 TRANSLATION BLOCKING MORPHOLINOS DOWNREGULATE PIEZO1 PROTEIN EXPRESSION.....	66
3.4 CELL AUTONOMOUS AND NON-CELL AUTONOMOUS REGULATION OF AXON GUIDANCE THROUGH PIEZO1 SIGNALLING .....	67
3.5 DISCUSSION .....	71
3.5.1 Verifying Piezo1 presence and depletion.....	71
3.5.2 Piezo1 depletion in axon pathfinding defects.....	73
ACKNOWLEDGMENTS .....	74
<b>4 CHARACTERIZATION OF PIEZO1-DOWNREGULATED BRAIN TISSUE .....</b>	<b>75</b>
4.1 BRAIN TISSUE STIFFNESS DECREASES WITH PIEZO1 DOWNREGULATION.....	75
4.2 SEMAPHORIN3A mRNA EXPRESSION DECREASES WITH PIEZO1 DOWNREGULATION IN THE CNS.....	79
4.3 DISCUSSION .....	83
4.3.1 Piezo1 downregulation and alterations in tissue mechanics.....	83
4.3.2 Piezo1 downregulations affects sema3A mRNA expression .....	84
ACKNOWLEDGMENTS .....	85
<b>5 CELL BODY DENSITY CONTRIBUTES TO TISSUE MECHANICS .....</b>	<b>87</b>
5.1 BRAIN TISSUE STIFFNESS CORRELATES WITH CELL DENSITY .....	88

5.2 TISSUE STIFFNESS CHANGES <i>IN VIVO</i> CORRELATE WITH LOCAL CELL BODY DENSITIES IN THE DEVELOPING BRAIN.....	90
5.3 BLOCKING MITOSIS <i>IN VIVO</i> RESULTS IN REDUCED LOCAL CELL BODY DENSITY, DIMINISHED STIFFNESS GRADIENTS, AND DECREASED OPTIC TRACT ELONGATION .....	92
5.4 DECREASED TISSUE STIFFNESS IN PIEZO1 DOWNREGULATED TISSUE IS NOT THE RESULT OF ALTERED NUCLEI DENSITY.....	96
5.5 DISCUSSION.....	98
5.5.1 <i>Cell body density as a readout of tissue stiffness</i> .....	98
5.5.2 <i>Piezo1 depletion and tissue softening</i> .....	99
<b>6 A NEW AND IMPROVED MORPHOLINO.....</b>	<b>103</b>
6.1 PIEZO1 IS DOWNREGULATED BY THE <i>X. LAEVIS</i> <i>PIEZO1.L</i> MORPHOLINO (PzL MO) .....	104
6.2 PIEZO1 DOWNREGULATION WITH BOTH MORPHOLINOS RESULTS IN <i>IN VIVO</i> AXON PATHFINDING DEFECTS .....	105
6.3 BRAIN TISSUE STIFFNESS DECREASES WITH PIEZO1 DOWNREGULATION USING PzL MO.....	106
6.4 <i>SEMA3A</i> RNA EXPRESSION IS ATTENUATED WITH PzL MO DEPLETION OF PIEZO1 IN THE CNS .....	108
6.5 SUMMARY .....	110
ACKNOWLEDGMENTS .....	111
<b>7 THE RELATIONSHIP BETWEEN TISSUE MECHANICS, SEMA3A, AND PIEZO1 .....</b>	<b>113</b>
7.1 THE EFFECT OF SEMA3A DOWNREGULATION ON TISSUE MECHANICS .....	113
7.2 THE EFFECT OF ENVIRONMENTAL STIFFNESS ON <i>SEMA3A</i> RNA LEVELS .....	117
7.2.1 <i>Softening brain tissue in vivo does not significantly alter sema3A RNA levels</i> .....	118
7.2.2 <i>Substrate stiffness modulates sema3A RNA levels in vitro</i> .....	120
7.2.3 <i>In vitro substrate stiffness affects sema3A RNA expression in cells that do not usually produce sema3A in vivo</i> .....	120
7.3 THE EFFECT OF PIEZO1 ACTIVITY ON BRAIN TISSUE STIFFNESS AND <i>SEMA3A</i> RNA LEVELS .....	121
7.3.1 <i>Piezo1 inhibition</i> .....	121
7.4 DISCUSSION .....	122
7.4.1 <i>Sema3A as a regulator of tissue stiffness</i> .....	122
7.4.2 <i>Environmental stiffness as a modulator of sema3A RNA levels</i> .....	124
7.4.3 <i>Understanding the spatio-temporal dynamics of Sema3A</i> .....	127
7.4.4 <i>Piezo1 activity in tissue mechanics and sema3A expression</i> .....	128
ACKNOWLEDGMENTS .....	129
<b>8 CONCLUSIONS.....</b>	<b>131</b>
8.1 KEY FINDINGS .....	131
8.2 CHARACTERIZING THE MECHANICAL ENVIRONMENT OF CELLS .....	133
8.3 MAKING SENSE OF PIEZO1 DOWNREGULATION .....	135
8.4 PIEZO1 AND SEMA3A IN OTHER TISSUES .....	136

8.5 FINAL REMARKS.....	137
<b>9 REFERENCES.....</b>	<b>139</b>

# *LIST OF TABLES*

TABLE 1 <i>IN VIVO</i> DRUG TREATMENTS USED IN EXPOSED BRAIN PREPARATIONS.....	39
TABLE 2 MORPHOLINO SEQUENCES TO DOWNREGULATE PIEZO1.....	41
TABLE 3 MORPHOLINO SEQUENCES FOR BRAIN ELECTROPORATIONS.....	44
TABLE 4 COMPOSITION OF ACRYLAMIDE, BIS-ACRYLAMIDE, AND HYDROXY-ACRYLAMIDE IN 500 $\mu$ L OF GEL PREMIX.	45
TABLE 5 PCR PRIMERS USED IN AMPLIFYING SPECIFIC REGIONS OF THE PLASMID AND FOR ARTIFICIALLY INSERTING A T3 RNA POLYMERASE PROMOTER SITE.....	48
TABLE 6 KITS USED FOR RNA EXTRACTIONS.....	52
TABLE 7 SUMMARY OF PRIMARY AND SECONDARY ANTIBODIES USED.....	57

# LIST OF FIGURES

FIGURE 1-1 ANATOMY OF A GROWTH CONE.....	2
FIGURE 1-2 SEMA3A SIGNALLING ALTERS ACTIN DYNAMICS AND STIMULATES ENDOCYTOSIS IN XENOPUS RGC GROWTH CONE COLLAPSE. ....	10
FIGURE 1-3 SEMA3A REPULSIVE TURNING IN GROWTH CONES.....	12
FIGURE 1-4 STRUCTURE OF MOUSE PIEZO1.....	17
FIGURE 1-5 PIEZO1 STIMULATION BY EXTERNAL AND INTERNAL MECHANICAL FORCES.....	19
FIGURE 1-6 PIEZO1 AND OTHER PLAYERS IN CELLULAR AND TISSUE MECHANOTRANSDUCTION.....	22
FIGURE 1-7 AXON GUIDANCE IN THE XENOPUS RETINOTECTAL PATHWAY.....	24
FIGURE 1-8. CANONICAL CHEMICAL GUIDANCE CUES IN THE DEVELOPING XENOPUS OPTIC PATHWAY.....	26
FIGURE 1-9 RGC AXONS ARE MECHANOSENSITIVE IN VITRO. ....	28
FIGURE 1-10 BRAIN TISSUE MECHANICS IN VIVO DEMONSTRATE THAT TISSUE STIFFNESS IS HETEROGENOUS AND CHANGES ACROSS DEVELOPMENT.....	30
FIGURE 1-11 DEVELOPMENT OF THE STIFFNESS GRADIENT PRECEDES AXON TURNING.....	32
FIGURE 1-12 PERTURBING MSCs RESULTS IN ABERRANT AXON PATHFINDING. ....	34
FIGURE 3-1 PIEZO1 IS PRESENT IN THE NEUROEPITHELIA AND IN THE AXONS OF THE OPTIC TRACT. ....	64
FIGURE 3-2 COLOCALIZATION OF Gt AND Rb ANTI-PIEZO1. ....	66
FIGURE 3-3 PIEZO1 MORPHOLINOS DOWN REGULATE PROTEIN EXPRESSION. ....	67
FIGURE 3-4 PIEZO1 IS REQUIRED IN BOTH THE AXONS AND THE SURROUNDING NEUROEPITHELIA FOR ACCURATE AXON PATHFINDING.....	71
FIGURE 4-1 PIEZO1 DOWNREGULATION RESULTS IN DECREASED TISSUE STIFFNESS.....	77
FIGURE 4-2 SEMA3A mRNA EXPRESSION IN THE BRAIN IS ALTERED WHEN PIEZO1 IS DOWNREGULATED IN THE CNS. ....	80
FIGURE 4-3 SEMA3A mRNA EXPRESSION IN THE WHOLE EMBRYO AT STAGE 40. ....	82
FIGURE 5-1 INCREASED CELL BODY DENSITY CORRELATES WITH TISSUE STIFFNESS.....	89
FIGURE 5-2 RELATIVE CELL BODY DENSITY INCREASES IN THE REGION ROSTRAL TO THE OPTIC TRACT, AS THE EMBRYONIC BRAIN DEVELOPS. ....	91
FIGURE 5-3 BI2536 TREATMENT ARRESTS CELLS IN MITOSIS AND DECREASES BRAIN CROSS-SECTIONAL AREA. ....	93
FIGURE 5-4 BI2536 TREATMENT RESULTS IN A DECREASE OF RELATIVE CELL DENSITY AND AFFECTS OT ELONGATION. ....	95
FIGURE 5-5 PIEZO1 DOWNREGULATION DOES NOT ALTER LOCAL CELL BODY DENSITIES. ....	97
FIGURE 6-1 VALIDATION OF PIEZO1 DOWNREGULATION USING PzL MO.....	104
FIGURE 6-2 CHARACTERIZING THE OPTIC TRACT OF PIEZO1 DOWNREGULATED EMBRYOS. ....	106
FIGURE 6-3 TISSUE STIFFNESS AND NUCLEI DENSITY DISTRIBUTION IS VERY SIMILAR BETWEEN PzT MO AND PzL MO KNOCKDOWN BRAINS. ....	107
FIGURE 6-4 SEMA3A RNA EXPRESSION IS ATTENUATED WHEN PIEZO1 IS DOWNREGULATED. ....	109
FIGURE 7-1 SEMA3A DOWNREGULATION IN THE NEUROEPITHELIA RESULTED IN TISSUE STIFFENING.....	114

FIGURE 7-2 ELECTROPORATION ITSELF DOES NOT CAUSE TISSUE STIFFENING.....	117
FIGURE 7-3 CS TREATMENT DECREASES BRAIN TISSUE STIFFNESS BUT DOES NOT SIGNIFICANTLY ALTER <i>SEMA3A</i> RNA LEVELS. ....	119
FIGURE 7-4 PERTURBING IN VIVO TISSUE STIFFNESS MAY ALTER <i>SEMA3A</i> RNA TRANSCRIPTION. ....	126
FIGURE 8-1: SUMMARY OF THE FINDINGS OF THIS PROJECT. ....	132
FIGURE 8-2 SUMMARY OF RESULTS FOR INDEPENDENT PERTURBATION OF <i>SEMA3A</i> RNA EXPRESSION AND ENVIRONMENTAL STIFFNESS. ....	133
FIGURE 8-3 STIFFNESS AND STERIC HINDRANCE THAT AXONS MAY ENCOUNTER FROM THE ENVIRONMENT.....	135

# *LIST OF ABBREVIATIONS AND ACRONYMS*

<b>AFM</b>	Atomic Force Microscope
<b>Br KD</b>	Neuroepithelia (brain tissue) knockdown
<b>C</b>	Caudal
<b>cAMP</b>	Cyclic adenosine monophosphate
<b>cDNA</b>	Complementary deoxyribonucleic acid
<b>cGMP</b>	Cyclic guanosine monophosphate
<b>CNGC</b>	Cyclic nucleotide-gated channels
<b>CNS</b>	Central nervous system
<b>CS</b>	Chondroitin sulphate
<b>Ctrl</b>	Control
<b>Da</b>	Dalton
<b>DAB</b>	Diaminobenzidine
<b>DAPI</b>	4',6-diamidino-2-phenylindole
<b>Dbl KD</b>	Double knockdown (knockdown in both the neuroepithelia and optic tract)
<b>DCC</b>	Deleted in colorectal cancer
<b>DIG</b>	Digoxigenin
<b>DiI</b>	1,1'-Dioctadecyl-3,3,3',3'-Tetramethylindocarbocyanine Perchlorate
<b>DNA</b>	Deoxyribonucleic acid
<b>E</b>	Young's modulus
<b>ECM</b>	Extracellular matrix
<b>EDTA</b>	Ethylenediaminetetraacetic acid
<b>ELISA</b>	Enzyme-linked immunosorbent assay
<b>F-Actin</b>	Filamentous actin
<b>FAK</b>	Focal adhesion kinase
<b>FARP2</b>	FERM, ARH/RhoGEF, and Pleckstrin domain protein 2
<b>FGF</b>	Fibroblast Growth Factor
<b>FIJI</b>	Fiji is just ImageJ
<b>G</b>	Shear Modulus
<b>g</b>	Gram

<b>GAP</b>	GTPase activating protein
<b>GPI</b>	glycosylphosphatidylinositol
<b>GsMTx4</b>	Grammastola spatulata mechanotoxin #4
<b>GTP</b>	Guanosine triphosphate
<b>HBSS</b>	Hank's Balanced Salt Solution
<b>hNSPC</b>	Human neural stem/progenitor cells
<b>HRP</b>	Horse Radish Peroxidase
<b>HUA</b>	Hydroxyurea/aphidicolin
<b>HUVECs</b>	Human umbilical vein endothelial cells
<b>k</b>	Spring constant
<b>K</b>	Apparent elastic modulus
<b>KD</b>	Knockdown
<b>L</b>	Litre
<b>L1CAM</b>	L1 immunoglobulin superfamily adhesion molecule
<b>LB</b>	Luria Broth
<b>m</b>	Metre
<b>M</b>	Molar
<b>MAB</b>	Maleic acid buffer
<b>MBS</b>	Modified Barth's Saline
<b>mcts1</b>	Malignant T-cell amplified sequence 1
<b>MO</b>	Morpholino
<b>mRNA</b>	Messenger ribonucleic acid
<b>MS222</b>	Tricaine methanesulfonate
<b>MSC</b>	Mechanosensitive ion channel
<b>mtch2</b>	Mitochondrial carrier 2
<b>MW</b>	Molecular weight
<b>N</b>	Newton
<b>NA</b>	Numerical Aperture
<b>NFPC</b>	NF-proto cadherin
<b>Npn1</b>	Neuropilin1
<b>OCT</b>	Optimum Cutting Temperature compound
<b>ONH</b>	Optic nerve head
<b>OT</b>	Optic tract

<b>OT KD</b>	Optic tract knockdown
<b>Pa</b>	Pascal
<b>PBS</b>	Phosphate buffered solution
<b>PCR</b>	Polymerase chain reaction
<b>PDL</b>	Poly-D-lysine
<b>PFA</b>	Paraformaldehyde
<b>pH3</b>	Phospho-Histone H3 (Ser10)
<b>PIP</b>	Phosphatidylinositol phosphate
<b>PlxA1</b>	Plexin A1
<b>PSF</b>	Penicillin-Streptomycin-Amphotericin B
<b>Pz1</b>	Piezo1
<b>PzL</b>	Xenopus laevis piezo1.L
<b>PzS</b>	Xenopus laevis piezo1.S
<b>PzT</b>	Xenopus tropicalis piezo1
<b>qPCR</b>	Quantitative polymerase chain reaction
<b>R</b>	Rostral
<b>RGC</b>	Retinal ganglion cell
<b>RNA</b>	Ribonucleic acid
<b>Robo</b>	Roundabout
<b>ROCK</b>	Rho-associated protein kinase
<b>ROI</b>	Region of Interest
<b>Scr</b>	Scrambled control
<b>Sema3A</b>	Semaphorin 3A
<b>siRNA</b>	Small interfering RNA
<b>slc35b1</b>	Solute carrier family 35 member B1
<b>Sox2</b>	SRY (sex determining region Y)-box 2
<b>sub1</b>	SUB1 homolog, transcriptional regulator
<b>t-RNA</b>	Transfer ribonucleic acid
<b>TAZ</b>	Transcriptional coactivator with PDZ binding motif
<b>Tec</b>	Tectum
<b>Tel</b>	Telencephalon
<b>TRPC1</b>	Transient Receptor Potential Channel 1
<b>TUNEL</b>	Terminal deoxynucleotidyl transferase dUTP nick end labeling

**UNC** Uncoordinated

**UV** Ultraviolet

**v** Poisson's ratio

**VE-cadherin** Vascular endothelial cadherin

**YAP** Yes-associated protein

**$\gamma$**  Strain

**$\sigma$**  Stress

**Units: p, n,  $\mu$ , m, c, M, G** pico-, nano-, micro-, milli-, centi-, mega-, giga-

**Ions:  $\text{Ca}^{2+}$ ,  $\text{Mg}^{2+}$**  Divalent calcium ion, divalent magnesium ion

# 1 INTRODUCTION

## 1.1 Making and connecting an embryonic brain

The early embryo is a relatively featureless sphere of cells. This ball of cells divides and grows, eventually losing its radial symmetry, and reshaping to form a complex, multi-layered organism with distinct tissues and organ systems. These transitions are reliant on the embryonic cells' sensing and responding to precise spatiotemporally controlled cell-intrinsic and environmental signals, that ensure appropriate differentiation, growth, and migration.

The brain and nervous system are highly organized and very precisely connected; much of this organization occurs throughout development. In the developing nervous system, newborn neurons extend neurites (protrusions that differentiate into axons or dendrites) that will eventually wire and connect the nervous system to its prospective target. These neuronal projections transmit information rapidly, across immense distances throughout the body. Hence, the correct formation of these networks during development is highly critical. This relies on neurites navigating accurately during development to their distant targets, with the help of various guidance cues from the environment. Defective axon guidance can be disastrous and is linked to numerous developmental disorders in humans (Engle, 2010; Nugent et al., 2012). Beyond development, accurate axon growth and guidance is also important in central and peripheral nervous system regeneration post-injury (Bradbury et al., 2000; Franze and Guck, 2010).

## 1.2 Axon growth and guidance (the machinery)

The distal end of the axon is tipped by a highly sensitive and motile apparatus called the growth cone (Figure 1-1). The growth cone senses, integrates, and responds to cues from the external environment to navigate unerringly towards its target. It is mostly made up of filamentous-actin (F-actin) that forms highly branched lamellipodia, and finer, exploratory protrusions called filopodia (Lowery and Vactor, 2009). The axon shaft connecting to the growth cone contains tightly bundled microtubules. The growth cone cytoskeleton is continuously remodelled throughout growth and pathfinding. F-actin assembly at the leading edge of the lamellipodium provides the driving force for the forward movement of the axon. Concurrently, actin filaments are continuously drawn away from the leading edge towards the axon shaft by myosin II motors (Medeiros et al., 2006), resulting in retrograde flows of actin in the growth cone. These rapid cytoskeletal dynamics, comprising assembly and disassembly of F-actin and local selective modification of microtubule dynamics at the growth cone (Buck and Zheng, 2002), in response to extrinsic cues, accounts for the growing and turning behaviour of axons.

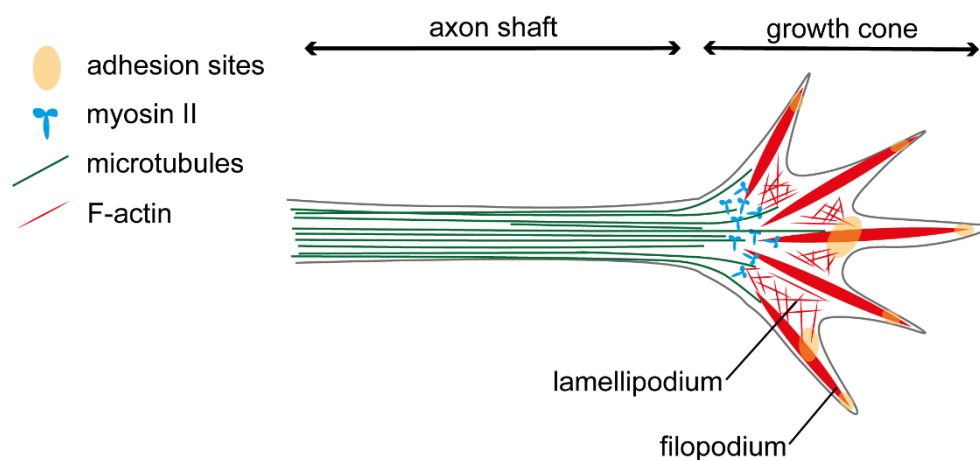


**Figure 1-1 Anatomy of a growth cone.**

*The growth cone is the distal most tip of the axon. It consists of a flat lamellipodium and fine protrusions called filopodia. These structures are mainly made up of actin filaments. Microtubules can also extend into the growth cone, from the axon bundles. The cytoskeleton couples to the external environment at adhesion sites. Myosin II motors are important in drawing acting filaments towards the shaft, in a ‘retrograde’ flow. Cartoon based on schematic in (Franze and Guck, 2010).*

The growth cone can assemble macromolecular adhesion complexes called ‘point contacts’ (similar to immature focal adhesion complexes) to attached to the surrounding substrate (Myers et al., 2011). Point contacts have integrins that link the cytoskeleton inside the growth cone to the extracellular matrix (ECM) outside. The coupling of continuous retrograde actin flow in the growth cone (Betz et al., 2011), with the point contacts ‘clutching’ the substrate, allow for forward movement of the growth cone (Chan and Odde, 2008). Meanwhile, asymmetric activation of specific receptors at the surface of growth cones in response to guidance cues from the environment activates intracellular signalling events that cause axon turning by locally affecting growth cone cytoskeletal organization. For instance, when presented with a repulsive cue, cytoskeletal elements in the growth cone proximal to the cue disassemble more quickly than on the side away from the cue, resulting in axons turning ‘away’ from the cue (Erskine and Herrera, 2007).

Besides the cytoskeletal elements that drive axon growth, and the point contacts and receptors at the growth cone that allow for cue responses from the environment, the axons also contain the basic machineries of protein translation and degradation, including endoplasmic reticulum (Luarte et al., 2018), and various messenger ribonucleic acids (mRNAs) (Zivraj et al., 2010) along with key translation machinery (Giuditta et al., 2002) and mitochondria (Smith and Gallo, 2018). This enables translation independent of the nucleus as the cell body is typically too far away for efficient diffusion of materials produced at the nucleus to be transported to the growth cone on the timescale at which axon guidance occurs. Blocking protein translation was shown to result in the inhibition of both attractive and repulsive turning (Campbell and Holt, 2001), while local mRNA translation mediated the adaptive response of axons to extrinsic signals *in vivo* (Shigeoka et al., 2016). Furthermore, guidance cues rapidly restructure the local proteome in axons, in a cue-dependent manner (Cagnetta et al., 2018), highlighting that the growth cone response to chemical guidance cues is multifaceted and still not fully understood.

### 1.3 Chemical guidance cues in axon pathfinding

Axonal growth direction can be altered by the binding of signalling molecules, called guidance cues, to growth cone receptors, that act as attractive or repulsive signals. These guidance cues can be short range, substrate bound molecules, or longer-range cues that are secreted by surrounding cells. There are four canonical families of axon guidance cues: Netrins, Slits, Ephrins, and Semaphorins. Early studies of these cues categorized them

rather simplistically as ‘repulsive’ or ‘attractive’. However, growth cone’s are able to adapt their response to the cues based on both cell intrinsic and extrinsic factors, thereby displaying a broad range of behaviours to a relatively small number of cues. Some of the factors that determine how a growth cone responds to a particular cue includes the temporal translation of receptors at the growth cone, the intracellular ratio of cyclic-AMP (cAMP) to cyclic-GMP (cGMP), and previous exposure to cues (reviewed in van Horck, Weinl, & Holt, 2004).

In addition to these canonical chemical guidance molecules and their various receptor complexes, a whole host of developmental morphogens (e.g. Sonic hedgehog (Trousse et al., 2001), and fibroblast growth factor signalling (Atkinson-Leadbetter et al., 2010; McFarlane et al., 1995; Yang et al., 2019)), proteoglycan components of the ECM (Holt and Dickson, 2005), and adhesive complex components (e.g. N-cadherin and integrins (Stone and Sakaguchi, 1996)), also affect axon pathfinding.

For most of the classical guidance cues, second messenger elevation acutely affects turning response. Upon cue-receptor binding, an elevation of cAMP or cGMP occurs. This is followed by a calcium influx, which in turn determines the growth cone turning response. Large elevations in calcium usually correspond to attraction while smaller calcium elevations correspond to repulsion. Therefore both cyclic nucleotide levels (Nishiyama et al., 2003; Song et al., 1997) and calcium (Hong et al., 2000; Zheng, 2000) are regulators that can switch the guidance response from attractive to repulsive, or conversely, from repulsive to attractive. The following is restricted to a brief review of the four major families of axon guidance cues and their receptors mainly in the context of the retino-tectal system (the model system investigated in this thesis, see section 1.5).

## **Netrins**

Netrins are a family of secreted matrix-binding proteins that can act as attractants and repellents depending on the cAMP:cGMP ratio; a high ratio favours attraction while a low one favours repulsion (Nishiyama et al., 2003). Receptors for netrins include DCC (deleted in colorectal cancer) and UNC5 homologues. DCC is thought to mediate chemoattraction while UNC5 is thought to be required in chemorepulsion (Moore et al., 2007). One of the first cues encountered by RGC axons is netrin-1. At the optic nerve head (ONH), neuroepithelial cells secrete netrin-1, which acts as an attractive cue, guiding the axons

out of the eye and onwards along the optic pathway. RGC axons express DCC receptors that mediate an attractive response to netrin-1. Deletion of netrin-1 and DCC genes in mice caused axon pathfinding errors: RGC axons reached the ONH but failed to exit the eye, growing instead to the other side of the retina (Deiner et al., 1997). However, the response to netrin is not always attractive in the *Xenopus* retino-tectal system, it becomes neutral and even repulsive later in development. As the axons progress along more distal parts of the optic pathway, a decline in cAMP levels and reduction of DCC receptor levels at the growth cone lead to a repulsive response to netrin-1 in the posterior tectum, preventing axons from overshooting the tectum (Shewan et al., 2002).

### **Ephrins**

There are two major classes of ephrins: ephrin-As which are anchored to cell membranes by glycosylphosphatidylinositol (GPI), and ephrin-Bs which have a transmembrane and cytoplasmic domain. The receptors of ephrins, EphA's and EphB's are similarly membrane-bound. Gradients of Ephs and ephrins in the retina and tectum are important in the formation of highly organized topographic maps. The temporo-nasal axis of the retina maps along the anterior-posterior axis of the tectum, while the ventro-dorsal retinal axis maps to the dorso-ventral axis of the tectum. The anterior-posterior axis mapping is thought to be dependent on repulsive activity of ephrinA cues on EphA-expressing axons (Huot, 2004) while ephrinB and EphB receptors are essential in establishing dorsoventral topography (Huot, 2004; Mann et al., 2002).

### **Slits**

Slits are large secreted proteins that are usually implicated in mediating axonal repulsion and also play an important role in axon branching (Brose and Tessier-Lavigne, 2000). The receptor family that mediates Slit-repulsion is Roundabout (Robo). Slit is expressed along the dorsal midline and at the anterior and posterior margins of the optic tectum in *Xenopus* (Piper et al., 2006). These are regions of the brain that RGC axons avoid, which is thought to result from Slits' repulsive effect. Slit/Robo binding leads to increased local protein synthesis of cofilin (a family of actin binding proteins usually involved in actin filament disassembly), in turn causing cytoskeletal rearrangements of the growth cone and a collapse response (Piper et al., 2006). Through this mechanism, Slit-Robo signalling is

essential in preventing axons from straying off the optic pathway into the telencephalon or other brain regions.

## **Semaphorins**

Semaphorins are one of the largest families of phylogenetically conserved guidance cues (Goodman et al., 1999). This protein family includes over 20 members that can be either secreted, transmembrane or cell-surface bound guidance cues. Semaphorins were first discovered for their role in axon guidance (Kolodkin et al., 1992; Luo et al., 1993), but they are now known to act as an important signalling molecule in a wide variety of contexts throughout the body (reviewed in (Yazdani and Terman, 2006)). In retino-tectal axon guidance, Semaphorins often act as repulsive cues during neuronal development through plexin receptors and neuropilin co-receptors. Semaphorin3A (Sema3A), a secreted guidance cue that plays a key role in the guidance of axons along the optic pathway in *Xenopus*, is of especial relevance to this thesis. Hence, I will elaborate on Sema3A in the following subsection.

### **1.3.1 Semaphorin3A**

There are eight members in the secreted class 3 Semaphorins, this section discusses Sema3A, one of the first Semaphorins to be discovered (and a guidance cue that is studied in this thesis). In the early 1990's, Raper and his colleagues isolated a protein that caused neuronal growth cones to undergo a dramatic morphological transformation and retract their actin rich filopodia and lamellipodia. They named this protein Collapsin after its ability to 'collapse' growth cones, this was later renamed Sema3A (Luo et al., 1993). It was quickly discovered that, in addition to its collapsing effects, this protein also caused axon turning when growth cones were asymmetrically stimulated (Fan and Raper, 1995). Additionally, Sema3A was also found to facilitate dendrite branching and synapse formation (reviewed in (Goshima et al., 2016)). Sema3A signalling was furthermore found to be crucial in early migration events that shape the nervous system, for example in the migration and segregation of neural crest cells (Osborne et al., 2005).

In addition to its role in the nervous system, Sema3A expression and function is highly diverse. Sema3A is also expressed in a range of other tissues (e.g. bones, epithelia, cartilage, adipose, muscle (Geiger et al., 2009; Giordano et al., 2003; Wright et al., 1995)), and in various organs (e.g. heart, kidneys, lungs, uterus (Ito et al., 2000; Marzioni et al.,

2004; Villegas and Tufro, 2002; Wright et al., 1995)). Some of the physiological functions of Sema3A signalling include bone and vascular formation (Behar et al., 1996; Serini et al., 2003), mesothelial and neural crest cell proliferation and migration (Catalan et al., 2004; Osborne et al., 2005), and endothelial cell adhesion and aggregation (Kashiwagi et al., 2005; Serini et al., 2003). The best characterized Sema signalling cascades, including those active in axon guidance, enact their function by initiating signalling networks that modulate cell adhesion and cytoskeletal structure and assembly, leading to profound effects on cell shape, fate, motility, and survival (reviewed in (Alto and Terman, 2017)).

### 1.3.1.1 The Sema3A receptor complex

All members of the Semaphorin family have a member of the plexin family as part of their receptor complex. However, in nearly all cases they also require a co-receptor. In particular, Class 3 semaphorins bind to neuropilins, Sema3A typically binds neuropilin1 (Npn1) and A-type Plexins (PlxA) (Huber et al., 2003). Binding of Sema3A to the Npn1-plexin A complex results in activation of the cytoplasmic domain of plexin resulting in various downstream signalling cascades. In addition to neuropilins and plexins, various other signalling proteins can also form a part of the Sema3A holoreceptor complex including L1CAM (L1 immunoglobulin superfamily adhesion molecule) (Castellani et al., 2000), integrins (Serini et al., 2003), calcium channels (Behar et al., 1999; Togashi et al., 2008), a whole host of kinases, and more summarized in (Yazdani and Terman, 2006). The composition of these molecules at the complex affect downstream Sema3A signalling. For example, when L1CAM in the membrane associates with Npn1, Sema3A binding to this receptor complex results instead in attraction rather than repulsion (Castellani et al., 2000). In addition to the molecules that participate in Sema3A signalling, lipid rafts (cholesterol and sphingolipid enriched membrane microdomains) are critical in regulating Sema3A activity. When lipid raft integrity was perturbed, the axons' response to Sema3A was affected; depleting membrane cholesterol blocked Sema3A induced axon repulsion (Guirland et al., 2004). The structural properties of lipid domains, along with physical clustering of various combinations of the Sema3A holoreceptor complex, e.g. calcium channels and integrins, may be important in regulating the diversity of Sema3A signal transduction.

### 1.3.1.2 Sema3A in axon turning

The molecular mechanisms by which Sema3A mediates its functional effects have not been completely elucidated; some of the signalling cascades downstream of Sema3A binding are reviewed in (Alto and Terman, 2017; Tran et al., 2007). The activation of neuropilin and plexin receptor complexes by Sema3A binding initiates intracellular signalling events that lead to redistribution of cytoskeletal elements and endocytosis of parts of the growth cone (Fournier et al., 2000). The following describes some of the downstream events of Sema3A signalling related to growth cone repulsive turning, as this is of particular relevance to this project.

While initially discovered as a collapsing factor, Sema3A is now known to induce a spectrum of responses in neurites, ranging from attraction and repulsion to branching and pruning (Pasterkamp and Giger, 2009; Tran et al., 2007). A host of downstream signalling molecules are known to contribute to these responses. Both repulsive and attractive signalling modalities involve elevation of cGMP, changes in membrane potential and subsequently calcium ion,  $Ca^{2+}$ , influxes (which is a second messenger to many processes). The Sema3A signalling cascade converges on the regulation of cytoskeleton and adhesion sites, where it changes actin contractility and polymerization, microtubule dynamics and so on, to cause changes in growth cone morphology and behaviour. In the case of the mid-optic tract bend in the *Xenopus* retinotectal system (discussed in section 1.5.2) Sema3A is thought to act as a repulsive cue that turn axons ‘away’ by disrupting the aforementioned processes on the side of the growth cone proximal to the cue. Some key components of this pathway are shown in Figure 1-2 and are discussed briefly below.

*In vitro*, stimulation of *Xenopus* spinal neuron growth cones with Sema3A triggers the production of intracellular cGMP, leading to membrane hyperpolarization (Nishiyama et al., 2008). Intracellular cGMP then activates cGMP-gated cyclic nucleotide gated calcium channels, resulting in increased calcium ion ( $Ca^{2+}$ ) entry into the cell (Togashi et al., 2008). Changes in intracellular  $Ca^{2+}$  and cyclic nucleotide levels result in a number of downstream effects through various kinases, phosphatases, and Rho-family small GTPases. For example, Sema3A induces local translation of the small GTPase RhoA, which regulates actin contractility via RhoA Kinase (ROCK), thus contributing to growth cone collapse or retraction (Wu et al., 2005). As seen in a number of other repulsive guidance cues as well, increased RhoA and therefore ROCK increases myosin II activity, potentially leading to an increase in actin retrograde flow in the growth cone, thereby

## Chapter 1: Introduction

reducing leading edge protrusions and resulting in growth cone collapse (Gomez and Letourneau, 2014; Shamah et al., 2001; Swiercz et al., 2002). RhoA activation also results in the inhibition of cofilin (an actin-binding factor), which in turn reduces F-actin barbed ends, thereby affecting actin polymerization (Aizawa et al., 2001). The combination of impaired actin turnover with increased actomyosin contractility at the growth cone contribute to collapse or retraction of the structure.

In addition to *Sema3A* binding regulating actin stability in the growth cone, *Sema3A* also stimulates endocytosis, inducing large scale membrane restructuring proximal to the cue, redirecting membrane adhesion and cytoskeletal components asymmetrically across the growth cone, and therefore biasing the direction of axon extension (Fournier et al., 2000; Tojima et al., 2011). *Sema3A* induced endocytosis is dose dependent; it is clathrin-mediated at low doses or macropinocytosis-mediated at higher doses (Kabayama et al., 2009; Piper et al., 2005) .

One reported endocytic pathway is through FERM, ARH/RhoGEF, and Pleckstrin domain protein 2 (FARP2, a guanine nucleotide exchange factor) recruitment to the PlxA-Npn1 complex. When *Sema3A* binds to the complex, FARP2 is dissociated and it then activates Rac (another Rho-family GTPase) (Toyofuku et al., 2005). Endocytosis then proceeds in a way that was found to require Rac activation (Jurney et al., 2002). A Rac downstream effector, Pak1, is thought to induce macropinocytosis by actin reorganization (Kabayama et al., 2011). Furthermore, the direct binding of Rac to Plexin is thought to induce a conformational change in the Plexin cytoplasmic tail, enhancing receptor endocytosis (Hall and Lalli, 2010; Turner et al., 2004)

Endocytosis is also crucial in the temporal control of repulsive turning. *Sema3A* exposure attenuates a growth cones collapse response when exposed to a second *Sema3A* stimulus (Piper et al., 2005). This desensitization is probably important in time-limiting an axon's response to a single cue, enabling it to then respond to the next cue it encounters as it grows. Piper et al. found that this rapid desensitization to *Sema3A* was due to *Sema3A*-induced depletion of *Sema3A*-bound receptor complexes from the growth cone surface via endocytosis.

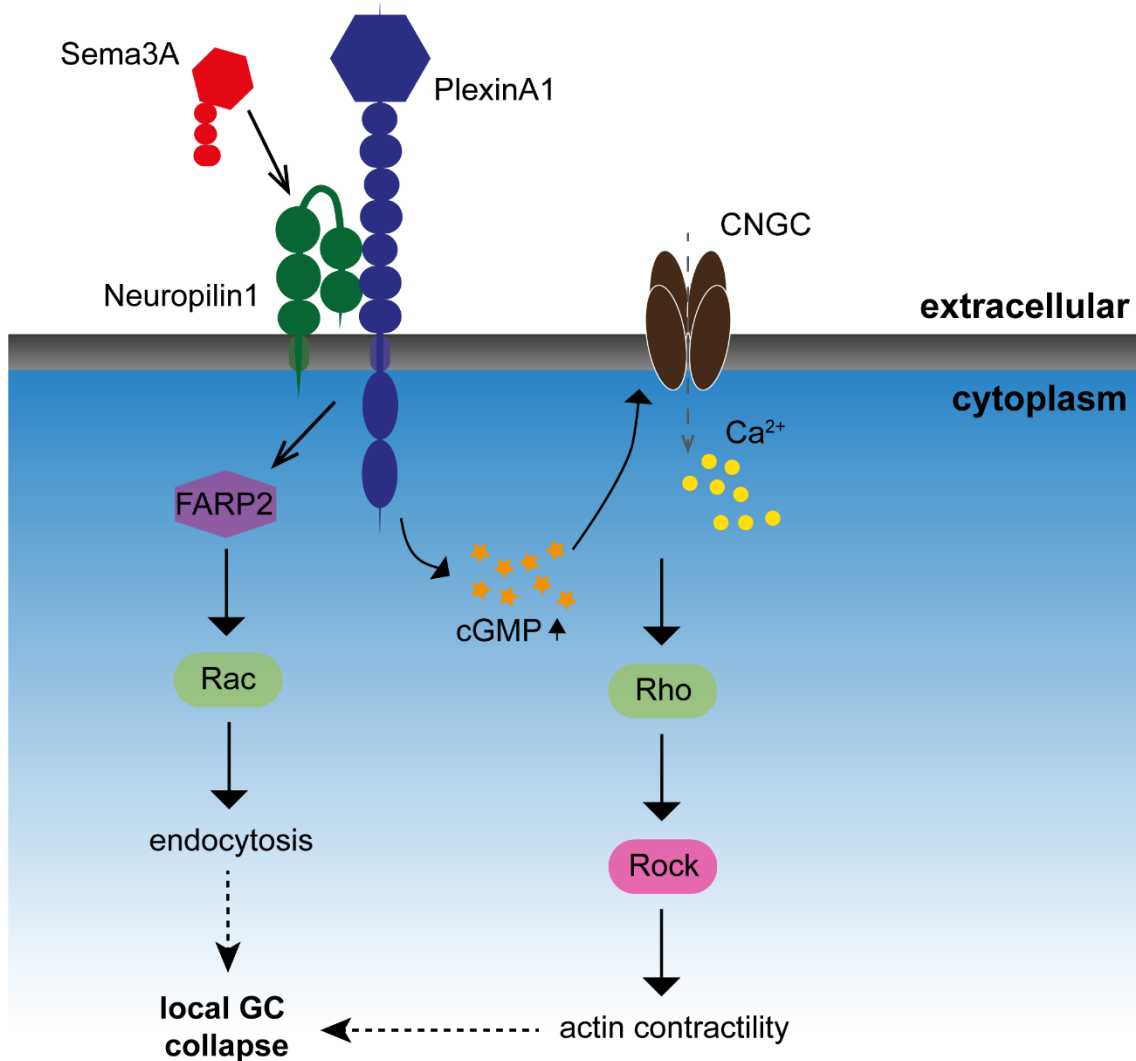


**Figure 1-2 Sema3A signalling alters actin dynamics and stimulates endocytosis in *Xenopus* RGC growth cone collapse.**

*FARP2 dissociates from the Npn1-PlxnA1 receptor complex and activates Rac, leading to endocytosis. Sema3A binding to the Npn1-PlxnA1 receptor complex results in an increase of intracellular cyclic GMP (cGMP) and Ca<sup>2+</sup> (potentially through cyclic nucleotide-gated channels, CNGCs). These intracellular second messengers regulate various downstream processes in the cell. Small GTPases are important downstream effectors of Sema3A e.g. RhoA is activated upon Sema3A binding to neuropilin-plexin and leads to downstream alterations of cytoskeletal dynamics, resulting in collapse or turning behaviour of growth cones. GC: growth cone, Npn1: Neuropilin1, PlxnA1: PlexinA1.*

## Chapter 1: Introduction

In addition to alterations of cytoskeleton dynamics, the growth cone collapse and repulsive turning responses involve disruption of adhesion sites on the side of the growth cone closer to the stimulus. Sema3A signalling modulates integrin activity via Ras GTPases. Sema3A induces the dissociation of Rac GEF FARP2 from the PlxA1/neuropilin complex promoting the recruitment of Rnd1 to PlxA1 (Hall and Lalli, 2010). The Rnd1/PlxA1 interaction opens R-Ras GAP domains in PlxA1 leading to Ras inactivation. Ras GTPases in turn can affect integrin mediated cell adhesion (Kinbara et al., 2003). Therefore, when Sema binds, plexin-GAP activity towards R-Ras reduces levels of active GTP-bound forms of R-Ras, leading to reduced integrin activation.

Sema3A also activates calpain (Kaczmarek et al., 2012; Qin et al., 2010), a protease that cleaves regulatory and cytoskeletal proteins. An increase in calpain activity can promote the disassembly of focal adhesion components such as talins and focal adhesion kinase (FAK) (Kerstein et al., 2017), resulting in decreased adhesion. However, Sema3A does not decrease all forms of adhesion. In the *Xenopus* retinotectal system (discussed in 1.5.2), Sema3A induces the local translation of NF-protocadherin (NFPC, a homophilic cell adhesion molecule) in RGC axons. The adhesion of the axons to the neuroepithelia at a specific point facilitates axon turning at the mid-optic tract.

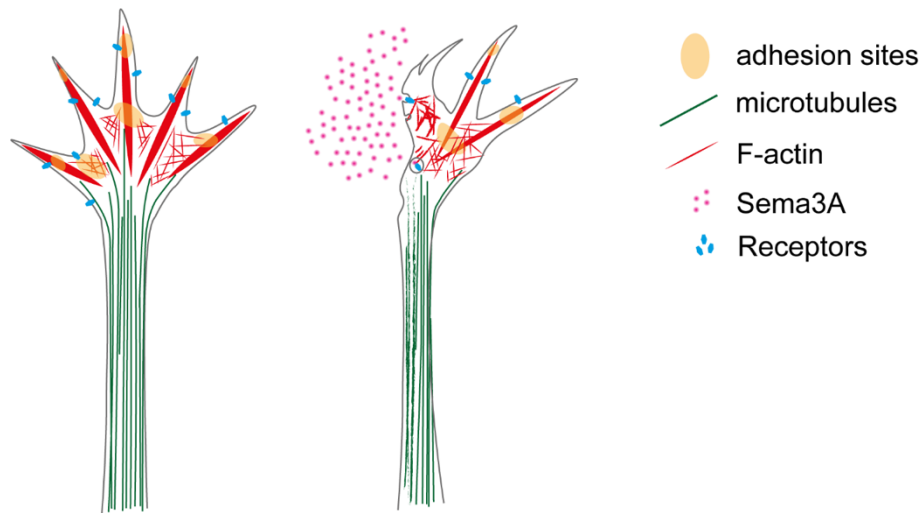


**Figure 1-3 Sema3A repulsive turning in growth cones.**

***Sema3A results in cytoskeletal disruption, increased endocytosis, and decreased adhesions proximal to the cue. Repulsive turning is a more polarized or local form of collapse.***

### 1.3.1.3 Sema3A in the nervous system

More broadly, Sema3A guidance plays an important role in establishing nervous system patterning during development, as the arrangement of neuronal projections that evolve during development are constrained by repulsive domains delineated by Semas. For instance, axons of mice with null mutations in Class 3 semaphorin genes projected abnormally, resulting in innervation of non-target tissue (Behar et al., 1996). Earlier still in development, Sema3A was found to affect axon/dendrite specification; exogenous Sema3A promoted dendritic growth and suppressed axonal growth.

In the system studied here, the developing *Xenopus* retinotectal system (see chapter 1.5), a repulsive region of Sema3A ensures that RGCs do not enter the mid-diencephalon but instead turn towards their target, the optic tectum (Campbell et al., 2001). Sema3A depletion led to partial stalling at the optic tract caudal turn and axon misprojection defects (Leung et al., 2013), or, when coupled with downregulation of *slit1*, resulted in dramatic stalling. In another study, where *sema3A* mRNA was downregulated alongside another critical guidance cue *slit1*, axons stalled dramatically at the caudal turn (Atkinson-Leadbetter et al., 2010), indicating that Sema3A is crucially involved in both axon growth

and turning. Campbell et al. postulated that once RGC axons reached the optic tectum, Sema3A there is likely to stimulate terminal branching (Campbell et al., 2001).

### 1.4 The mechanical environment of a neuron

Neuronal growth and development is not only dependent on chemical signals, but also on the biophysical properties of the environment (Franze et al., 2013). In this section, I will briefly introduce some terms used in this thesis to describe the mechanical properties of materials. This is followed by a brief review of the role of mechanics in axon guidance and nervous system development, and a discussion on cellular mechanosensing and the mechanosensitive ion channel Piezo1.

#### 1.4.1 Mechanics of materials

Methods to measure mechanics in this thesis, focus on the elastic properties of the material, be it compliant cell culture substrates or in vivo brain mechanics. Elastic materials are materials which deform linearly in response to an applied force and return to their original conformation when the force ceases. The force exerted per unit area of a material is referred to as stress ( $\sigma$ , units: Pa = N/m<sup>2</sup> = pN/ $\mu$ m<sup>2</sup>).

The application of stress will result in measurable strain  $\gamma = \Delta L/L$  (the relative deformation of a material under stress, whereby  $L$  is the original size of the object and  $\Delta L$  the absolute deformation). The ratio of stress to strain ( $\sigma/\gamma$ ) is a measure of the stiffness of the material and, in case of a force that is normal to the surface of the material, is called the elastic or Young's modulus ( $E$ , **unit:** Pa) of the material.

In this thesis, the stiffness of compliant substrates, for in vitro cultures, is reported in shear modulus ( $G$ , unit: Pa).  $G$  quantifies the elastic resistance ( $\sigma/\gamma$ ) of a material to shear deformations, i.e. under forces that act in parallel to the material surface.

For an isotropic elastic material,  $E$  can be converted to  $G$  using  $E = 2G(1 + \nu)$ , whereby  $\nu$  is the Poisson's ratio of a material. The Poisson's ratio ( $\nu$ ), quantifies a materials elastic resistance to elongation or compression. It is the ratio of transverse expansion (elongation) to axial compression. Most materials have a  $\nu$  between 0 and 0.5 with biological materials typically have a  $\nu$  between 0.4 and 0.5 (Franze, 2013).

Biological tissues are unlikely to be purely elastic, in that they do not “snap” back to their original state after being deformed. These materials are likelier to have both elastic and

viscous components. Viscosity is the resistance of a fluid to flow (e.g. honey has a relatively high viscosity while water has a relatively low viscosity). However, the elastic response of tissue dominates in short time scales and with small deformations (Fung, 1993). Thus, the Young's modulus as a measure of tissue stiffness is reasonable if experimental parameters are carefully controlled.

For brain stiffness measurements in this thesis, reduced apparent elastic modulus values,  $K$ , (equivalent to  $E/1-\nu^2$ ) are used, instead of  $E$ .  $K$  can be calculated from AFM indentation measurements using the Hertz Model for spherical indenters (described in 2.5.3). Expressing tissue stiffness in  $K$  rather than  $E$  is advantageous, as it does not require measuring or assuming a value for  $\nu$ .

#### 1.4.2 Mechanical cues in axon guidance

Prior to the development of biochemical and genetic means of studying guidance molecules, early theories of axon guidance suggested that mechanical cues were important in guiding axons and organizing them into nerves and tracts pathfinding (Harrison, 1910; Weiss, 1934; Weiss, 1945). Cells that were grown on the collagen fibres of fish scales, along plasma clots, or on culture dishes etched with grooves on the surface, strikingly followed the orientation of the substrates topography (Ohara and Buck, 1979; Weiss, 1934; Weiss, 1945). However, the anisotropy between these conditions extended beyond topology and included the chemistry of the environment (arguably collagen fibre of fish scales and an etched cell culture dish are chemically rather different). With recent micro- and nano-fabrication methods, cellular response to topography can be tested in a much more controlled and refined fashion (reviewed in (Simitzi et al., 2017)). Topographical cues such as alternating grooves and ridges (or parallel aligned fibers) strongly enhanced axon guidance and orientation along the grooves (or along the fiber axis) (Simitzi et al., 2017). In addition to topographical cues, axons also respond to environmental stiffness, both *in vitro* and *in vivo* (discussed in detail in sections 0 and 1.5.4). For example, axons on soft (0.1 kPa) substrates are less fasciculated and shorter than axons on stiff (1 kPa) substrates. Substrate stiffness of the hydrogels used here (and in the rest of this thesis, unless otherwise stated) is reported as shear modulus,  $G$ . Similarly, softening brain tissue resulted in shorter and more splayed retinal ganglion cell axons *in vivo* (Koser et al., 2016). These results suggest that environmental stiffness modulates axon behaviour in growth, bundling, and ultimately, pathfinding.

### 1.4.3 Mechanics in neuronal development, growth, and connectivity

Beyond axon pathfinding, mechanical cues can affect various processes early in axonal development. From the late 1970's, Dennis Bray pioneered a set of experiments demonstrating that growth cones of neurons exert tension and that mechanical tension stimulated axon growth *in vitro* (Bray, 1979; Bray, 1984). A microelectrode was attached to a growth cone and pulled slowly and progressively, resulting in axonal elongation, without a decrease in diameter. The maintenance of the axon's diameter suggested that neurons detected the applied mechanical tension and stimulated the addition of new materials (e.g. membrane/cytoskeletal elements) along the axon. Besides axon growth, transient tension applied to minor neurites resulted in axon specification (Lamoureux et al., 2002) in cultured rat hippocampal neurons.

Axon fasciculation (bundling of individual axons to its neighbours) is also regulated dynamically by mechanical forces along the axon shaft. In fact, the bundling behaviour is regulated by competition between mechanical tension within individual axons and axon-axon adhesions in the bundle (Šmít et al., 2017); adhesion forces favoured fasciculation while intrinsic tension promoted unbundling from the group.

In addition to axon specification, growth and bundling, mechanics may also control axon branch pruning as neural networks form (Anava et al., 2009). Anava et al. found that axons that attached to anchoring sites -patterned on a substrate- straightened out (suggesting an increase in tension) and other branches of the axon retracted, resulting in an elimination of redundant processes in the network. Moreover, mechanical tension was also shown to modulate the accumulation of neurotransmitter containing vesicles at presynaptic terminals, therefore regulating synaptic plasticity (Siechen et al., 2009).

In addition to tension, substrate mechanics also influences neuronal differentiation and maturation. Rodent neural stem cells exhibited higher neurogenesis on softer substrates (< 1 kPa) and preferentially differentiated into glia/oligodendrocytes on stiffer (>5 kPa) substrates (Leipzig and Shoichet, 2009; Saha et al., 2008), substrate stiffness was reported in Young's Modulus,  $E$ . Additionally, unpublished work from our group has shown that substrate mechanics alter neuronal maturation. Primary rat hippocampal neurons developed functional electrical properties more quickly, and formed synapses earlier on softer substrates, compared to neurons cultured on stiffer substrates (Hélène Gautier and Eva Kreysing, personal communication).

Thus, at multiple scales, mechanics plays a crucial role in regulating neuronal development, growth, and connectivity. The area of neuronal development most pertinent to this thesis is that of axon guidance. In this thesis, I more closely investigate how mechano-sensing and -signalling regulates axon pathfinding.

#### 1.4.4 Cellular mechanosensing and transduction

Mechanical signals from the intracellular and external environment of a cell are both diverse and ubiquitous. For example, cells both perceive external forces in their environment, while also generating intracellular forces (e.g. when moving, dividing, elongating, or adjusting to osmotic changes in the environment). Some of the ways in which cells sense and respond to mechanical stimuli are through structural elements (i.e. the cytoskeleton), linkage proteins (e.g. integrins), mechanosensitive ion channels, transcription factors (e.g. YAP and TAZ), and more (Cox et al., 2019).

Cells couple their intracellular cytoskeletal elements to the extracellular environment via transmembrane proteins such as integrins or other cell adhesion molecules (e.g. NCAMs) at focal adhesions. Integrins at focal adhesion sites (or ‘point contacts’ in neurons) directly bind to and transmit external forces from the ECM to the actin cytoskeleton and *vice versa*. Many proteins found in adhesion complexes, which link integrins to cytoskeletal elements, are themselves inherently mechanosensitive (e.g., talin) (Goult et al., 2018). Talin can regulate the strength of integrin adhesions, sense matrix rigidity, and increase focal adhesion size and maturation, in response to forces (Reviewed in (Klapholz and Brown, 2017)). Besides talin, there are a multitude of other proteins associated with the integrin complex (including kinases, phosphatases, and other adaptor proteins); these signalling proteins enable a wide range of biochemical cascades to occur in response to the physical forces experienced. Hence, focal adhesion dynamics affect not only cytoskeletal structure but also cellular morphology, fate, and behaviour (Geiger et al., 2009).

In addition to the linkage proteins and the cytoskeleton, mechanosensitive ion channels (MSCs) are key players in cellular mechanosensing and mechanotransduction. MSCs are pore-forming membrane proteins that respond to mechanical stimuli. MSCs are both sensors and effectors, as they sense mechanical cues from the environment and transduce this information into biochemical or electrical signals that lead to various downstream cellular processes. MSCs are gated by mechanical stimuli, and are one of the most rapid signal transducers known, converting mechanical signals into biologically relevant signals

within milliseconds (Cox et al., 2019). External mechanical cues include sound (i.e. pressure) waves, shear forces, stretching/bending/torsion, osmotic pressure, and touch. As environmental mechanical cues are ubiquitous and diverse, both specialized mechanosensory cells (that are dedicated to detecting external cellular forces, e.g. auditory hair-cells or Meissner's corpuscle cells) and non-specialized cells are likely to have diverse populations of MSCs (Peyronnet et al., 2014). A variety of MSCs have been found (reviewed in (Ranade et al., 2015)), however, the one of most relevance to this study is Piezo1, which I will describe in more detail in the following section.

#### 1.4.5 Piezo1

Piezo1 was identified as a mechanically activated ion channel that induced currents in a neuroblastoma cell line, Neuro2A, via membrane stretch and indentation (Coste et al., 2010). Piezo1, at 900 kDa and over 2500 amino acids, is a gargantuan channel. Cryogenic electron microscopy studies have shown that Piezo1 is a homotrimeric channel with three curved propeller-like blades at the extracellular domain surrounding a central pore module, and three intracellular beams (Coste et al., 2012; Ge et al., 2015; Saotome et al., 2018; Zhao et al., 2018).

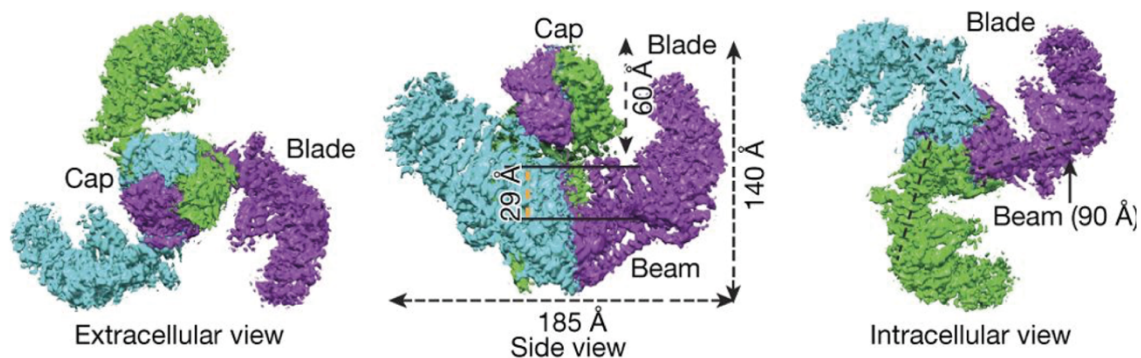


**Figure 1-4 Structure of mouse Piezo1.**

*The cartoons show the three subunits of Piezo1 (colour coded), from the extracellular, side, and intracellular views. Piezo1 is a complex homotrimer, with a central cap, three peripheral blades and three intracellular beams. Adapted from (Zhao et al., 2019).*

Piezo1 responds to a variety of external mechanical cues including shear stress (Li et al., 2014; Ranade et al., 2014), membrane stretch (Coste et al., 2010), osmotic shock (Lacroix

et al., 2018; Syeda et al., 2016), pulling forces (Gaub and Müller, 2017), membrane indentation (Coste et al., 2010; Cox et al., 2016), cell stretching (Gudipaty et al., 2017), and substrate stiffness (Pathak et al., 2014), and also to intrinsic cues such as cell-generated traction forces (Ellefsen et al., 2019) (Figure 1-5). Piezo1 is permeable to cations, with a preference for  $\text{Ca}^{2+}$  (Gnanasambandam et al., 2015). Intracellular  $\text{Ca}^{2+}$  is an essential second messenger in physiological processes, ranging from gene transcription and differentiation, to cell shape changes and apoptosis (Clapham, 2007), suggesting that the downstream response of Piezo1 activation is varied and complex.

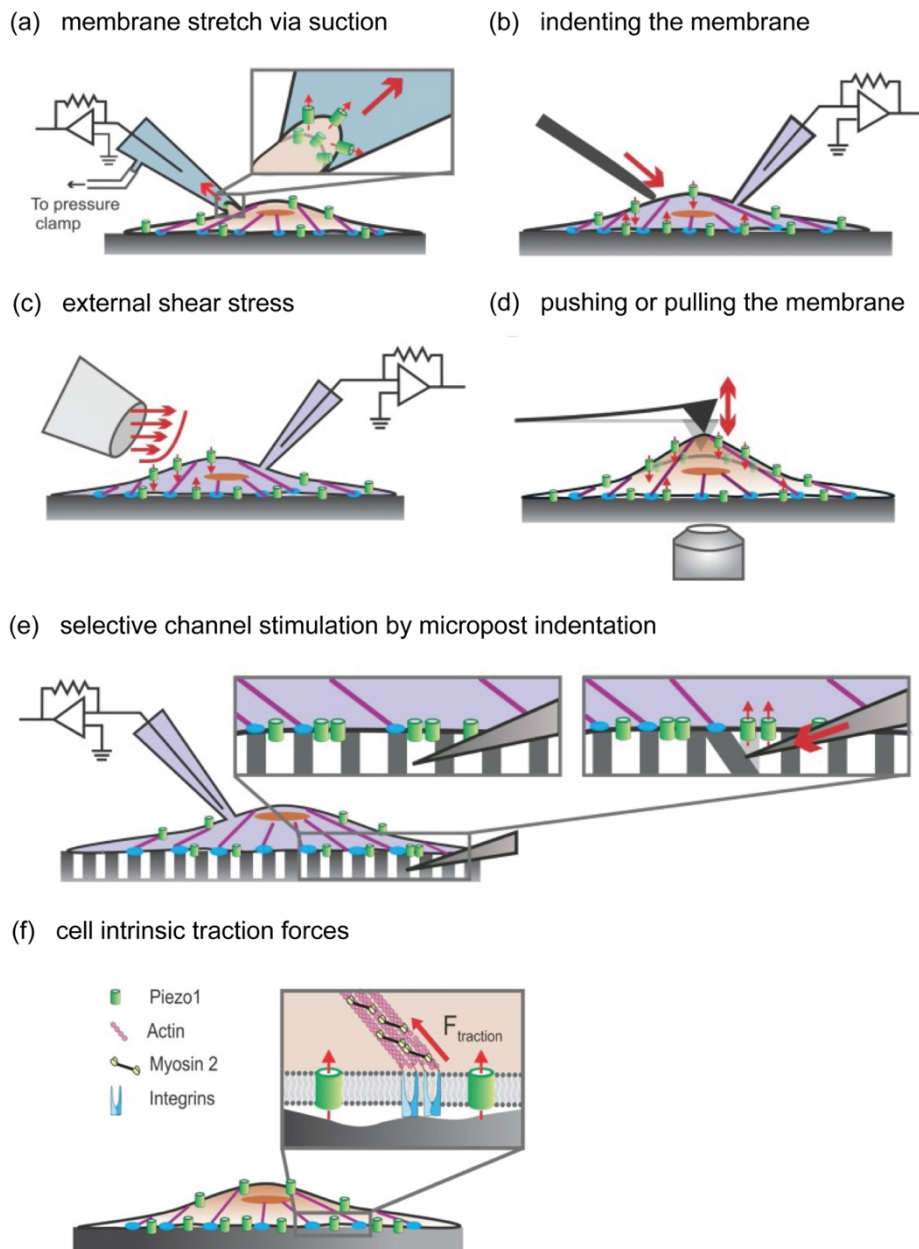


**Figure 1-5 Piezo1 stimulation by external and internal mechanical forces.**

*(a-e) Piezo1 transduces ‘outside-in’ mechanical forces. (a) Membrane stretch by suction pulses imparted by a high-speed pressure clamp, Piezo1 activity is measured in cell-attached patch clamp mode. (b-c) Piezo activity is measured from whole-cell patch clamp. (b) Membrane stretch by cell indentation, using a glass probe. (c) Shear stress by fluid flow from a perfusion pipette. (d) The cell surface is pushed or pulled using an atomic force microscope (AFM) cantilever, Piezo1 activity is measure using  $Ca^{2+}$  imaging with a confocal microscope. (e) Cells are seeded on micropost arrays, a probe is used to deflect single microposts, to mechanically stimulate a small number of*

*channels near the post. Piezo1 electrical activity is measured in whole-cell patch clamp. (f) Piezo1 also transduces 'inside-out' mechanical forces. Piezo1 is activated by traction forces (solid red arrow) generated at integrin-rich focal adhesion sites by myosin 2 molecules, along the actin cytoskeleton. Actin filaments are indicated in purple, focal adhesions in blue, and Piezo1 in green. Solid red arrows show force application, while small arrows indicate ionic conduction through Piezo1. Adapted from (Nourse and Pathak, 2017)*

The precise gating mechanism of Piezo1 *in vivo* is not completely understood. However, when Piezo1 was reconstituted into lipid droplets, lipid bilayer tension alone was sufficient to activate it (Syeda et al., 2016). The results from this highly simplified system suggest that Piezo1 is inherently mechanosensitive and can be gated via the force-from-lipids paradigm, i.e. by force transmission through the membrane bilayer in the absence of other cellular components.

However, several other studies have implicated the cytoskeleton in Piezo1 gating. For instance, when actin polymerization was inhibited through cytochalasin D application, Piezo1 current amplitudes were strongly reduced, suggesting that the actin cytoskeleton played a role in transmitting mechanical stimuli from the indentation probe to Piezo1 (Gottlieb et al., 2012). To more closely examine the role of the cytoskeleton in Piezo1 gating, Cox et al. compared Piezo1 activation in cell-attached patches (which retained the connections between the membrane and the cytoskeleton) to that in membrane blebs (which lacked cytoskeletal elements) and found that bleb attached patches could be more easily activated. These results suggested that the cytoskeleton plays a mechanoprotective effect on Piezo1, making it harder to open the channel (Cox et al., 2016). While this finding is contradictory to that seen in Gottlieb et al.'s results, the methodologies used were different. The Cox et al. study utilized cell attached patches whereby pressure was applied as currents were recorded, whereas Gottlieb et al, mechanically stimulated the cell with an external probe and recorded whole cell currents. The whole cell compared with patch environment are likely to be quite different. Nonetheless, both studies suggest that the cytoskeleton also modulates Piezo1 activity.

## Chapter 1: Introduction

In addition to Piezo1's response to cell-extrinsic cues, a recent study examined endogenous Piezo1 activity in response to cell-intrinsic forces instead. In the absence of external mechanical forces, Piezo1 signal was found to localize around focal adhesions, at regions of high cell-generated traction forces (Ellefsen et al., 2019), though how the force generated at focal adhesions is transmitted is not yet known.

Piezo1 trimers also inherently curve the membrane, and this curvature is thought to amplify the sensitivity of Piezo1 to changes in membrane tension (Guo and MacKinnon, 2017; Haselwandter and MacKinnon, 2018). Membrane mechanics however is also dependent on membrane composition, different lipid populations and cholesterol levels can affect the fluidity, ordering of the membrane, bending rigidity and elasticity of the membrane (Needham and Nunn, 1990). Piezo1 gating is sensitive to alterations in membrane lipid composition, as disrupting membrane cholesterol domains impairs Piezo1 signalling (Ridone et al., 2019). Thus, a bidirectional relationship exists, whereby the membrane influences Piezo1 activity and similarly Piezo1 influences local properties of the membrane it sits in.

In addition to the interaction between Piezo1 and cell intrinsic components such as the plasma membrane composition and cytoskeletal elements, the presence of ECM proteins were found to sensitize Piezo1's response to mechanical forces (Gaub and Müller, 2017). ECM organization pathways were also significantly enriched when Piezo1-correlated genes were studied in human glioma datasets (Chen et al., 2018).

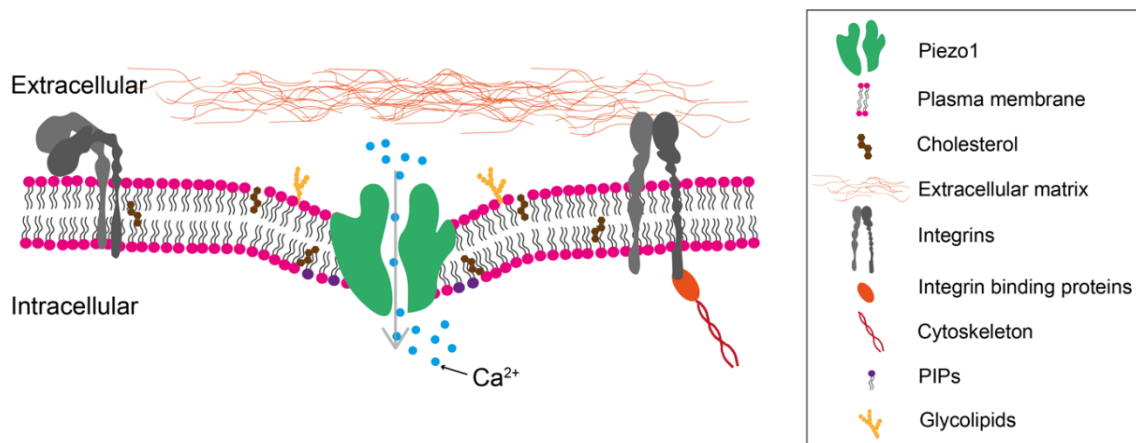


**Figure 1-6 Piezo1 and other players in cellular and tissue mechanotransduction.**

***Piezo1 induces membrane curvature and interacts with extracellular matrix (ECM) proteins. PIP: phosphatidylinositol phosphate.***

When Piezo1 was discovered, it was found to be highly evolutionarily conserved, as it is present in animals, plants and protists. It is also expressed in a wide-variety of tissues, including the bladder, brain, lungs, vascular and skeletal systems (Coste et al., 2010). Some of the physiological roles of Piezo1 in various cell-lines and model organisms have been elucidated by gain-of-function or depletion studies. Piezo1 is critical in development, as global knockout in mice result in embryonic lethality due to devastating vascular defects (Li et al., 2014; Ranade et al., 2014). Piezo1 is also important in differentiation as it affects the lineage choices of mesenchymal (Sugimoto et al., 2017) and neural stem cells (Pathak et al., 2014). Furthermore, Piezo1 is crucial in regulating cell numbers in CNS development (Segel et al., 2019), red blood cell volume regulation (Cahalan et al., 2015), arterial remodelling (Retailleau et al., 2015), lymphatic valve (Nonomura et al., 2018) and bone (Li et al., 2019; Sun et al., 2019) formation, and axon guidance (Koser et al., 2016).

Piezo1's role in axon guidance is of particular relevance to this thesis as I followed up Piezo1's role in regulating the interplay between mechanical and chemical signalling in axon guidance. For my studies, I used the well-characterized *Xenopus* retinotectal system, which is described in the following chapter.

## 1.5 The *Xenopus laevis* retinotectal system as model of axon growth and pathfinding

For the experiments presented in this thesis, I studied the developing *Xenopus laevis* (African claw-toed frog) retinotectal system. Here, retinal ganglion cells (RGC) send out axons from the eye to the optic tectum, the centre for processing visual information in the *Xenopus* brain.

*Xenopus* are an excellent model organism for studying development in general, and axon guidance in particular. Some of the advantages include easy husbandry, high fecundity, and simple *ex utero* fertilization. Many large embryos are produced, and the system is highly amenable to cell and embryological studies. Of especial value to this project is that axon guidance cues have been extensively characterized and studied, particular in the retinotectal system. Furthermore, *Xenopus* embryonic brains can be easily exposed and subjected to various treatments. RGC axons grow superficially at the surface of the neuroepithelia, which is relatively flat when the whole embryo is mounted laterally, this renders the system uniquely suitable for *in vivo* visualisation of fluorescently labelled RGC axons and atomic force microscopy-based measurements of brain tissue mechanics.

In the following sections, I briefly describe the *in vivo* pathway taken by these axons, the chemical guidance cues encountered, and the *in vivo* and *in vitro* responses of these axons to environmental stiffness.

### 1.5.1 Journey to the tectum: the growth of RGC axons

RGCs are born at around stage 24 in the embryonic retina (Holt et al., 1988), developmental stages used in this thesis are based on stages described in (Nieuwkoop and Faber, 1994). These axons grow along the surface of retina to the optic nerve head (ONH), where they then exit the eye as optic nerves. Optic nerves cross completely into the contralateral brain hemisphere in the optic chiasm, which they reach at around stage 32 (Holt, 1989). Subsequently RGC axons grow relatively superficially in a tightly bundled tract (optic tract, OT) through the diencephalon towards the optic tectum. At ~stage 35/36, the OT makes a highly stereotypical caudal turn in the mid-diencephalon before reaching the tectum at ~stage 40 (McFarlane and Lom, 2012). Here the axons defasciculate and connect with their target cells.

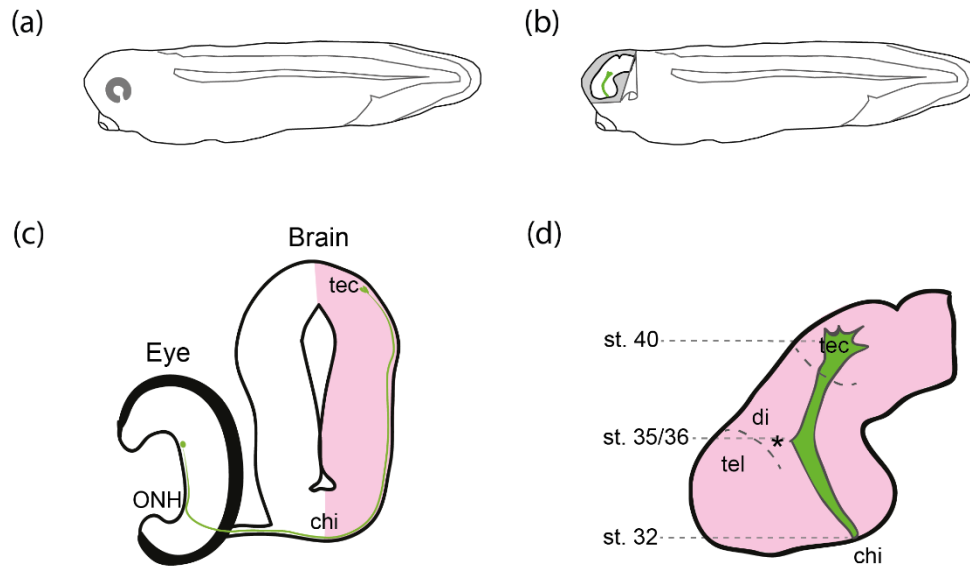


**Figure 1-7 Axon guidance in the *Xenopus* retinotectal pathway.**

*(a) Cartoon of an intact *Xenopus* embryo, (b) shows the embryo, with the epithelia and underlying dura mater removed to expose the brain and the OT is shown in green. (c) Cartoon (in the cross-section of the embryo) of a single RGC axon's path, starting from the eye to the optic tectum in the brain (green). The contralateral brain hemisphere is indicated in pink. (d) Lateral view of the brain, with the OT (bundle of all the RGC axons from the opposite side) shown in green. The axons cross the optic chiasm at stage 32, grow across the neuroepithelia, making a highly stereotypical bend (\*) at stage s35/36 and terminate at the tectum at stage 40. Cartoons based on (McFarlane and Lom, 2012). Chi: optic chiasm, di: diencephalon, ONH: optic nerve head, OT: optic tract, st: stage, tec: optic tectum, tel: telencephalon.*

### 1.5.2 Chemical guidance of *Xenopus* RGC axons

The neuroepithelia, across which axons grow, are a rich and diverse environment, containing a multitude of cues that provide instructive and modulatory signals to the growing axons. Experiments in the 1980s revealed that chemical cues, locally present at the neuroepithelia, guided RGC axon growth. For example, when regions of the neuroepithelia were rotated clockwise or counter-clockwise by 90°, RGC axons that later grew into that region also turned 90°, in correspondence with the direction of rotation (Harris, 1989). These results demonstrate that a local guidance cue, present at the neuroepithelia, strongly instructed axon growth direction. Quite remarkably, when eye

primordia were removed and re-implanted some distance away (such that they could not project along their regular pathway) retinal axons still made tectal projections (Harris, 1986). These results strongly suggest that the axons were homing into an attractive long-range cue found at the tectum.

Since then, many groups have identified and studied different chemical cues and the RGC axons response to them (reviewed in (Erskine and Herrera, 2007)). Some of the main chemical guidance cues directing axon pathfinding in this system are elucidated here.

RGC axons in the optic fibre layer of the retina first navigate through the retina to the optic nerve head. At the optic nerve head, the surrounding neuroepithelial cells secrete netrin-1, which is sensed by DCC receptors on the RGCs. In this context, the netrin-DCC signalling is thought to be attractive, ensuring the proper exit of RGC axons from the eye (Deiner et al., 1997). In an age-related switch, upon leaving the eye, RGC axons lose their attraction to the netrin-1 gradient, enabling entry to the brain (Shewan et al., 2002).

In the brain, axons at the optic chiasm project to the contralateral brain hemisphere. The chiasm is enriched by temporally controlled inhibitory signals of sonic hedgehog (Trousse et al., 2001) and Slits (Erskine et al., 2000; Plump et al., 2002), that redirect aberrantly growing RGC axons, ensuring axons project completely contralaterally in *Xenopus* embryonic development.

From the chiasm to the tectum, the axons are constrained along a narrow path by Slit/Robo signalling and repulsive chondroitin sulfate proteoglycans in the telencephalon, while repulsive sonic hedgehog prevent axons from straying too far caudal to the OT (Gordon et al., 2010; Hutson and Chien, 2002; Ichijo and Kawabata, 2001). Partway between the chiasm and the tectum, the mid-OT bend is associated with gradients of secreted Slits1 and 2 and Sema3A (Atkinson-Leadbeater et al., 2010; Campbell et al., 2001). The Sema3A and Slit cues are thought to be repulsive, guiding the axons away from the diencephalon towards the tectum.

The response to Sema3A is age-dependent: younger axons (stage 24-28) do not respond to an external Sema3A cue whereas older axons (>stage 33/34) show a repulsive response as neuropilins begin to be expressed only from this timepoint (Campbell et al., 2001). The activation of neuropilin and plexin receptor complexes by Sema3A binding initiates intracellular signalling events that lead to axon turning (see 1.3.1 for mechanistic details). The increased local translation of RhoA leads to complete or partial growth cone collapse on the side proximal to the cue.

Furthermore, *Sema3A* induces local translation of NFPC, a homophilic cell adhesion molecule that promotes OT adhesion to the neuroepithelia from the bend onwards (Leung et al., 2013), further guiding the OT along a highly specific path. Depletion of NFPC or *Sema3A* results in splaying and straying from their usual tract or stalling (Atkinson-Leadbeater et al., 2010; Leung et al., 2013). Finally, axons reach the tectum, where Eph/ephrin signalling determines the topographic mapping of the axons (Mann et al., 2002). The initial position of the RGC cell body in the retina determines the synaptic partner at the tectum. Some of the key guidance cues discussed in this section are illustrated in Figure 1-8.

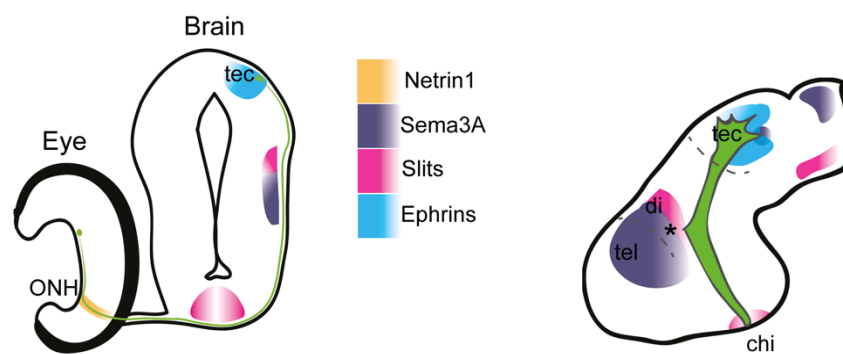


**Figure 1-8. Canonical chemical guidance cues in the developing *Xenopus* optic pathway.**

*The cartoon shows the approximate localization of some critical chemical guidance cues that guide RGC axons from the eye to the tectum. Cartoon based on (McFarlane and Lom, 2012).*

### 1.5.3 Mechanosensitivity of *Xenopus* RGC axons *in vitro*

Axonal growth is a highly dynamic process. In order for a GC to move, it needs to exert physical forces on its environment and mechanically interact with it. Such mechanical interactions are important regulators of axon growth. For example, *in vitro*, RGC axons respond strongly to changes in substrate stiffness (Koser et al., 2016). Eye primordia (early embryonic eye tissue) were cultured on soft (0.1 kPa) and stiff (1.0 kPa) substrates, and the axonal outgrowth was compared (Figure 1-9 a, b). On stiff substrates, axons were longer than on soft substrates, regardless of the substrate ECM coating (Figure 1-9 f); laminin and fibronectin were used (both these ECM molecules engage different populations of integrins). Overall, axons grew faster, but less directionally on soft substrates, while directional persistence was higher on stiff substrates, ensuring more efficient outgrowth (Figure 1-9 d, e). Furthermore, axonal fasciculation was also stiffness-dependent. On stiffer substrates, axons bundled better and preferentially adhered to neighbouring axons while on softer substrates, axons were less likely to fasciculate and showed more exploratory behaviours (Figure 1-9 g, h).

Mechanosensitive ion channels (MSCs) are vital players in sensing and transducing the mechanical cues from the environment. Grammastola spatulata mechanotoxin #4 (GsMTx4), a selective inhibitor of MSCs, reduced axonal outgrowth on stiff substrates (Figure 1-9 c, f). The phenotype was in fact similar to axons on soft substrates, suggesting that MSCs are more active on stiffer substrates, and play an instructive role in the regulation of axon growth. In summary, substrate stiffness alters axon growth behaviour *in vitro* and MSCs are involved in mechanosensing.

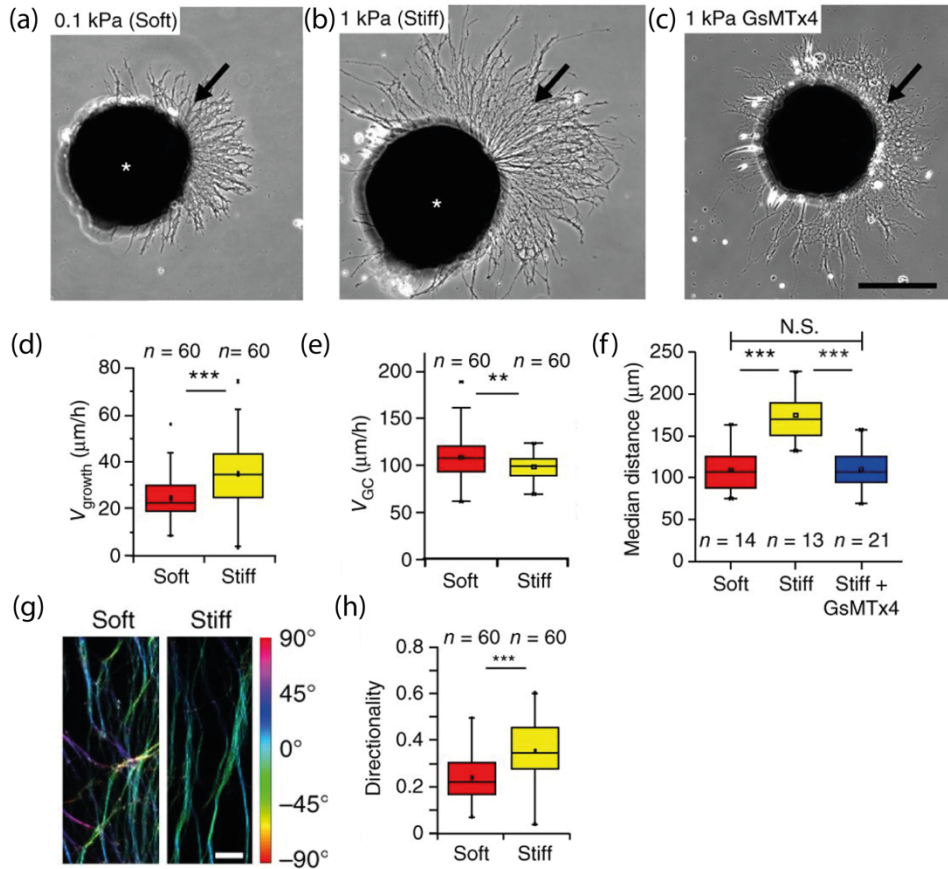


**Figure 1-9 RGC axons are mechanosensitive *in vitro*.**

*(a,b) Cultures of Xenopus eye primordia (asterisks) on (a) soft (0.1 kPa) and (b) stiff (1 kPa) substrates. Arrows indicate axons. (c) Eye primordium grown on a stiff substrate and treated with GsMTx4. Scale bar is 200  $\mu\text{m}$ . (d) The extension velocity of axons ( $v_{\text{growth}}$ ) was significantly higher on stiff substrates. (e) On soft substrates, growth cones (GC) were more exploratory and migrated significantly faster than on stiff ones. (f) Median distances of axon length. Axons were significantly longer on stiffer substrates than either on soft ones or after GsMTx4 treatment. Neurons grown on stiff substrates and treated with GsMTx4 resembled neurons grown on soft substrates. (g) Processed fluorescence images of  $\beta$ -tubulin-labeled RGC axons; color represents local angular orientation of axonal segments. On soft substrates, axons grew less directionally persistently (from bottom to top). (h) On stiff substrates, axon growth was more directed (i.e., straighter) than on soft substrates. Scale bar: 15  $\mu\text{m}$ . Boxes show the 25th, 50th (median), and 75th percentiles; whiskers show the spread of the data (excluding outliers), and an 'O' the mean score for a group.  $n$  = number of eye primordia from*

*three biological replicates. \*\*P = 0.00867; \*\*\*P < 10<sup>-5</sup>; N.S., nonsignificant. This figure is adapted from (Koser et al., 2016).*

#### 1.5.4 *In vivo* brain mechanics

As *Xenopus* RGCs are mechanosensitive *in vitro*, their mechanical environment was characterized using an *in vivo* atomic force microscopy (AFM)-based approach to map local tissue stiffness of exposed intact developing brains at different developmental stages (Koser et al., 2016) (Figure 1-10 a, b). AFM measurements were made at stage 33/34, when axons first left the optic chiasm and grow across the contralateral neuroepithelia and at stage 39 to 40, when axons first reached the optic tectum (Figure 1-10 c). In general, *Xenopus* brain tissue is inherently mechanically heterogeneous. When regions of tissue on either side of the OT were studied more closely, at stage 33/34, this region is relatively homogeneous. By stage 40, however, a stiffness gradient perpendicular to the OT emerged. At this later stage, the tissue region rostral to the mid-OT bend was significantly stiffer than the region caudal to it (Figure 1-10 d). When RGC axons were ablated, this stiffness gradient still formed, suggesting that the stiffness was independent of axon growth in the region. Tissue stiffness was found to scale with cell body density in the brain, as the stiffer region rostral to the OT had a higher cell body density than the region caudal to the OT (Figure 1-10 e, f).

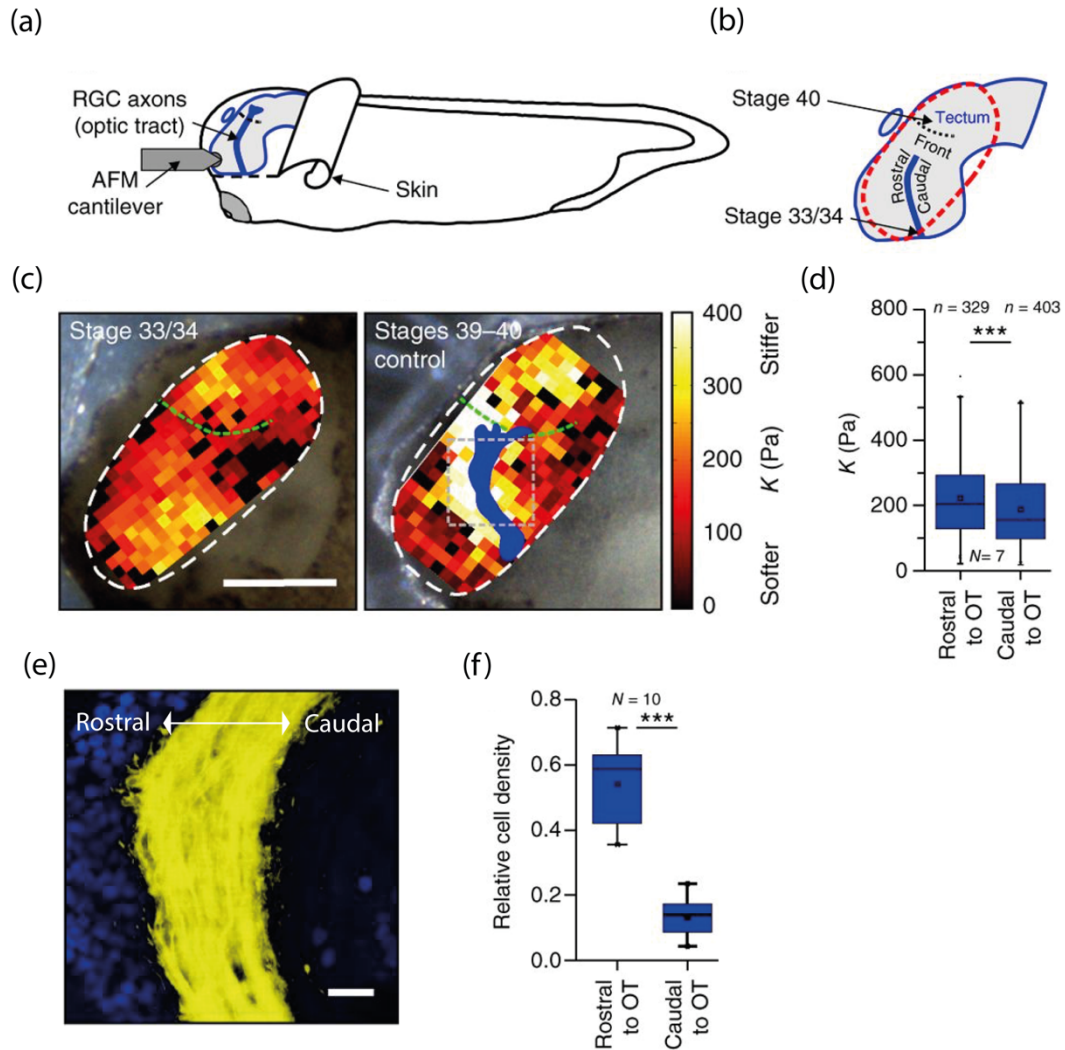


**Figure 1-10 Brain tissue mechanics *in vivo* demonstrate that tissue stiffness is heterogenous and changes across development.**

(a) *Schematic of the experimental setup.* (b) *Xenopus brain. The dashed red line indicates the stiffness map area.* (c) *Images of Xenopus embryos with overlaid AFM-based stiffness maps of exposed *in vivo* brain tissue. Colour encodes the apparent elastic modulus  $K$  assessed at an indentation force of 7 nN. Blue shape in shows the OT location. Scale bar: 200  $\mu\text{m}$ . At both stage 33/34 (left) and stages 39 and 40 (right), brain tissue was mechanically heterogeneous and displayed visible stiffness gradients. Green dashed lines indicate tectum boundaries. The grey dashed square in the stage 39-40 image indicates the region shown in (e).* (d) *At stages 39 and 40, tissue rostral to the OT was significantly stiffer than caudal to it.* (e) *Immunohistochemistry demonstrated a significantly higher density of cell nuclei (blue) rostral to the OT (yellow) than caudal*

*to it. Scale bar: 20  $\mu\text{m}$ . (f) Quantification of cell densities on both sides of the OT; cell density was significantly higher rostral to the OT.  $n$  = number of measurements,  $N$  = number of animals. Boxes show the 25th, 50th (median), and 75th percentiles; whiskers show the spread of the data (excluding outliers), and an 'O' the mean score for a group. \*\*\* $P < 10^{-4}$ . This figure is adapted from (Koser et al., 2016).*

The formation of the mid-OT stiffness gradient was studied more closely using time lapse AFM (Thompson, Pillai et al., 2019). RGC axons were fluorescently labelled and a region of interest at ~the mid-OT bend of the neuroepithelia was mapped in the same embryo, before, during and after OT bending. We found that the formation of the stiffness gradient preceded RGC axon turning, demonstrating that the stiffness gradient was likely to provide an instructive turning cue to the axons Figure 1-11. When the stiffness gradient was abrogated by disrupting mitosis, axon pathfinding was aberrant. Similarly, when tissue mechanics was altered by exogenous softening treatments or by inducing ectopic stiffening in the brain, axon pathfinding was affected (Koser et al., 2016). Therefore, stiffness gradients that develop *in vivo* influence axon growth, and alterations to these mechanical gradients affect axon pathfinding.

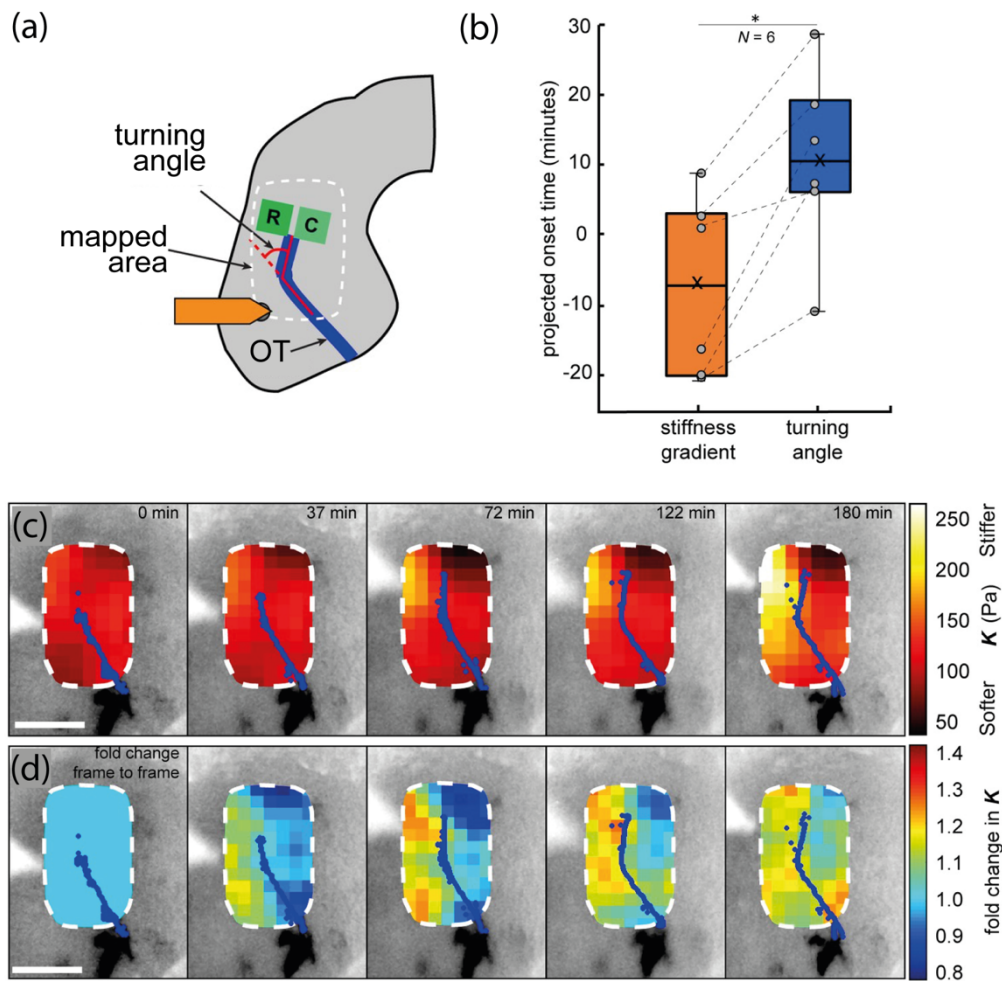


**Figure 1-11 Development of the stiffness gradient precedes axon turning.**

*(a) Diagram of the brain, showing the approximate region mapped by AFM (white dashed line), within which optic tract (OT) axons (blue) turn caudally. Also shown are the regions of interest (green boxes) used to calculate brain stiffness rostral and caudal of the OT, and hence the developing stiffness gradient. Red overlaid lines show calculation of the angle through which OT axons turn (turn angle). (b) Boxplots of the extrapolated appearance times of the stiffness gradients and the onset of OT axon turning, relative to the start time of timelapse-AFM measurements, with ladder plots for individual embryos overlaid. Extrapolations are based on linear fits to the re-scaled data for individual animals. Stiffness gradients appear significantly earlier than the onset of axon turning. (c) Stills from a representative time-lapse stiffness map. Fluorescently labelled OT axons (pseudo-coloured in blue) and processed AFM-based stiffness maps (colour maps) are overlaid on images of the brain. Colour maps encode the apparent*

*elastic modulus,  $K$ , a measure of tissue stiffness, assessed at an indentation force  $F = 10$  nN. The time in minutes on each frame is taken from the timestamp of the first measurement in each successive stiffness map; the corresponding overlaid fluorescence images were obtained simultaneously. (d) Visualisation of fold-changes in brain tissue stiffness from one time point to the next, based on the interpolated and smoothed data shown in (c). Colour scale encodes the fold-change in  $K$  at each location on the stiffness map, expressed relative to the values at the previous time point, with the exception of  $t = 0$  min, where all values were set to 1. Tissue stiffness changes throughout the time course, with large changes already occurring between  $\sim 40$ – $80$  min after the start of the experiment. This figure is adapted from (Thompson, Pillai et al., 2019).*

#### 1.5.5 Mechanosignalling via Piezo1 is crucial in *in vivo* axon pathfinding

RGC axons robustly respond to substrate stiffness *in vitro* through MSCs, and the local mechanical environment *in vivo* influences axon guidance. Blocking MSCs *in vivo*, using GsMTx4, also resulted in shorter axons and severe axon pathfinding defects, demonstrating that MSCs are required in accurate axon pathfinding. Depletion of the MSC Piezo1 in the *Xenopus* central nervous system (CNS) also resulted in severe axon pathfinding errors. These results demonstrated that RGC axon mechanosensing *in vivo* is reliant on MSCs in general, and the MSC Piezo1 in particular is critical for accurate axon pathfinding (Figure 1-12).

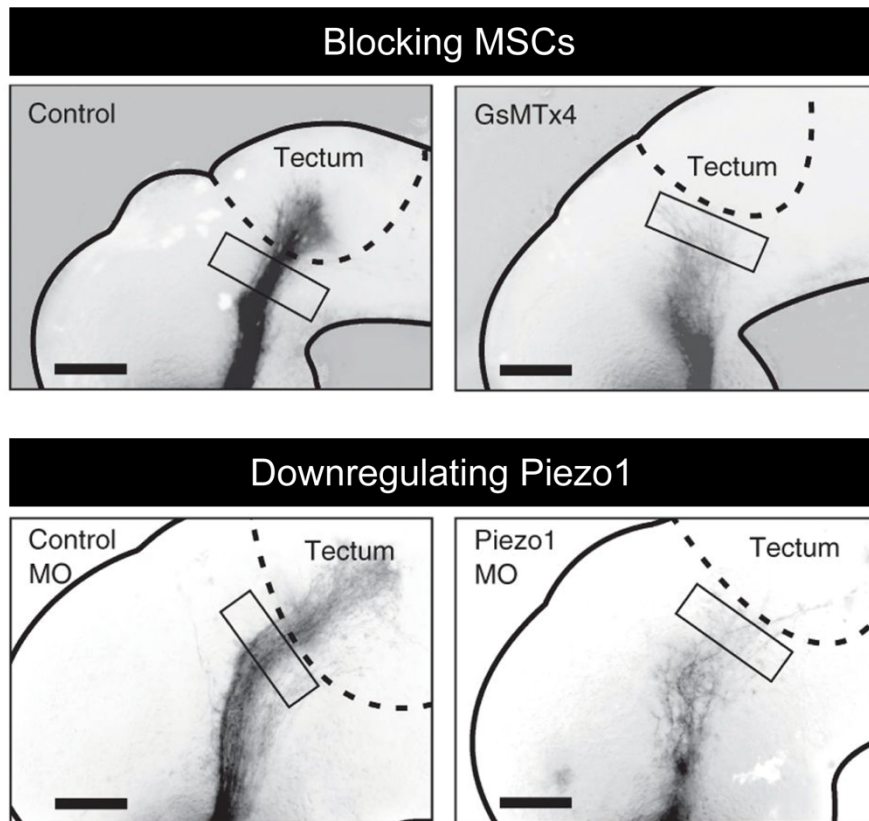


**Figure 1-12 Perturbing MSCs results in aberrant axon pathfinding.**

*Blocking MSCs by application of 25  $\mu$ M GsMTx4 disrupted axon pathfinding in vivo. Axons were shorter and spread more, resembling axons cultured on soft substrates in vitro. Similarly, downregulation of Piezo1 in the CNS using morpholinos, resulted in aberrant axonal growth. The rectangular regions highlight the OT region before the tectum, whereby in the controls, axons remain bundled whereas in the case of GsMTx4 and Piezo1 downregulation, axons appear defasciculated and shorter. This figure is adapted from (Koser et al., 2016).*

## 1.6 Aim of this study

The initial aim of this study was to better understand the role Piezo1 in axon guidance. It developed to also include some understanding of the interplay between chemical and mechanical signalling during development. I have used the *Xenopus laevis* retinotectal system as a model to address the following questions:

1. How does Piezo1 affect axon guidance? As Figure 1-12 shows, Piezo1 depletion results in axon pathfinding defects. Therefore, I first investigated if Piezo1 regulation of RGC axon guidance is cell-autonomous or non-cell-autonomous.
2. Does Piezo1 downregulation result in alterations to the chemical and mechanical environment that axons grow in?
3. As I found that both tissue stiffness and *sema3A* mRNA levels (two critical axon guidance cues *in vivo*) are affected by Piezo1 depletion, I wanted to explore the interplay between these two cues.



# 2 METHODS

Reagents are from Sigma unless otherwise specified

## 2.1 Manipulating the *Xenopus* embryo

### 2.1.1 *Xenopus* husbandry

All animal experiments described in this thesis are in compliance with the Ethical Review Committee of the University of Cambridge and adhere to the guidelines set by the UK Home Office. Single-cell stage, wild-type *Xenopus laevis* embryos of both sexes were fertilised *in vitro* with mechanically homogenised testes. Embryos were reared in  $0.1 \times$  Modified Barth's Saline (MBS – the composition of  $10 \times$  MBS: 88 mM NaCl, 1 mM KCl, 2.4 mM NaHCO<sub>3</sub>, 1 mM HEPES, 0.82 mM MgSO<sub>4</sub>, 0.33 mM Ca(NO<sub>3</sub>)<sub>2</sub>, 0.41 mM CaCl<sub>2</sub>, pH 7.6) at 14–18°C to reach the desired developmental stage, as described by in (Nieuwkoop and Faber, 1958). All embryos used in this study were below stage 45.

### 2.1.2 Exposed brain preparation of *Xenopus* embryos.

A modified exposed brain protocol previously described in (Irie et al., 2002) was used to expose the brain surface to various chemical treatments or to expose the brain surface to enable AFM measurements.

Briefly, wild-type *Xenopus* embryos were anaesthetised in *Xenopus* exposed brain medium (0.04% w/v tricaine methanesulfonate (MS222),  $1 \times$  Penicillin-Streptomycin-Amphotericin B (PSF, Lonza,  $1 \times$  PSF: 1% v/v of a 100x solution containing: penicillin (10,000 U/mL), streptomycin (10,000 µg/mL), amphotericin B (25 µg/mL)), in  $1.3 \times$  MBS, pH 7.6), transferred to a Sylgard 184-coated (Dow Corning) dissection dishes and immobilised by pinning down at the neck region with bent 0.2 mm minutien insect pins (Austerlitz). All embryo dissections and manipulations were carried out using 0.15 and 0.1 mm minutien insect pins (Austerlitz) in pin holders unless otherwise stated. Here, the eye, epidermis, and dura on the side facing up was removed, exposing the telencephalon,

diencephalon and tectal surfaces. Embryos were then transferred to the relevant treatment solution or to a measuring dish for AFM measurements (see 2.2.2).

High salt concentration solution,  $1.3 \times$  MBS, retards skin regrowth allowing the experiments to take place over several hours. This allows for a chemical treatment to act across several developmental stages or for AFM maps to be made without skin regrowth affecting the stiffness measurements. The viability of embryos throughout exposed brain experiments was assessed by the presence of a visible heartbeat (Gurdon et al., 1997).

### 2.1.3 *In vivo* chemical treatments

Stage 33/34 *Xenopus* embryos with exposed brains were transferred to 4-well dishes (Thermo Fisher Scientific) with either a control or treatment solution (reagent concentrations and rationale are described in Table 1. Five to six embryos were placed in each well and the samples were light protected. The embryos were incubated overnight at 20°C until they reached stage 39-40.

**Table 1** *In vivo* drug treatments used in exposed brain preparations.

Reagent	Rationale	Treatment concentration	Control
Chondroitin sulfate	Softening the brain tissue surface	15 mg/ml in <i>Xenopus</i> exposed brain medium	<i>Xenopus</i> exposed brain medium
BI2536 (MedChem Express)	Inhibits <i>in vivo</i> cell proliferation	50 $\mu$ M in <i>Xenopus</i> exposed brain medium	<i>Xenopus</i> exposed brain medium
GsMTx4 (Abcam, Tocris)	Mechanosensitive ion channel blocker	1.5-25 $\mu$ M in <i>Xenopus</i> exposed brain medium	<i>Xenopus</i> exposed brain medium

#### 2.1.4 *In vivo* eye primordia ablation

To obtain embryos with brains free of RGC axons, eye primordia were removed prior to axons crossing onto the contralateral brain hemisphere through the optic chiasm. Embryos at stage 31-32 were anaesthetised and prepared for dissection as described above in 2.1.2, but in a lower osmolarity solution of  $1.0 \times$  MBS + 0.04% (w/v) MS222 +  $1 \times$  PSF. This was the solution used to anaesthetise embryos in all experiments unless otherwise stated. Both eye primordia were removed while keeping the skin and dura over the brain as intact as possible. Embryos were left to recover at 18°C in  $0.5 \times$  MBS + 0.02% (w/v) MS222 for 1 hour, and then transferred to  $0.1 \times$  MBS without anaesthetic and left to develop to stage 40.

#### 2.1.5 *In vitro* eye primordia cultures

Explants were cultured from stage 35/36 embryos. Prior to dissection, embryos were anaesthetised in a 1:1 solution of the anaesthetic media (described in *in vivo* eye primordia ablation) and *Xenopus* culture medium (60% Leibovitz L15 medium with  $1 \times$  PSF, pH 7.6). Intact eye primordia were removed and placed immediately into *Xenopus* culture medium. Eye primordia were placed, lens-side up, on functionalized glass-bottom

microwell dishes (MatTek, MA, USA) or hydrogel substrates. Both glass and hydrogel substrates were functionalized at room temperature with 10 µg/mL poly-D-lysine (PDL, MW 70-150 kDa) diluted in phosphate buffered solution (PBS, Oxoid) for 30 minutes and followed by 5 µg/mL laminin in PBS for 30 minutes. Hydrogel substrates were functionalized with the same concentrations of PDL and laminin, the functionalisation is discussed below in section 2.2.1. Explants were moved to a 20°C incubator 2-3 hours after plating the eye primordia. Eye primordia were fixed using 2% paraformaldehyde (PFA), 7.5% sucrose after ~22-24 hours in culture.

### 2.1.6 *In vitro* neuroepithelia cultures

The forebrain region, which produces *Sema3A* and region of the brain caudal to it which does not usually produce *Sema3A*, were dissected from stage 35/36 embryos. 20 brain regions (per hydrogel) were collected in *Xenopus* culture medium. Brain regions were mechanically dissociated with 1% v/v DNase in Ca<sup>2+</sup>- and Mg<sup>2+</sup>-free Hank's Balanced Salt Solution (HBSS, Gibco), and incubated for 5 minutes at 37°C. Each tube was topped up with 4-fold the volume of *Xenopus* culture medium before being spun down for 6 minutes at 650 *G*. The supernatant was removed, and 1 mL of *Xenopus* culture medium was added to the pellet fraction to gently resuspend the cells. 500 µL of resuspended cells were added to each functionalised hydrogel substrate. After 2 hours, the dishes were gently topped up with a further 1.5 mL *Xenopus* culture medium and cultured for 22-24 hours in a 20°C incubator.

### 2.1.7 Translation blocking by morpholino blastomere injections

Translation-blocking morpholino oligonucleotides were designed and synthesised by GeneTools. Morpholinos directed against *Xenopus tropicalis piezol* (PzT MO), *Xenopus laevis piezol.L* (PzL MO), and a standard non-specific sequence control (i.e. scrambled) morpholino (Scr MO) were used. I also designed a morpholino against *Xenopus laevis piezol.S* (PzS MO) for use in future experiments.

Prior to the publication of the full *Xenopus laevis* genome (Session et al., 2016), *Piezo1* was downregulated using PzT MO (Koser et al., 2016) as the only available sequence was that of the closely related *Xenopus tropicalis*. As the *Xenopus laevis* genome was not fully annotated, I extracted the sequence of *piezol.L* and *piezol.S* with help from Dr Toshiaki Shigeoka (Holt Group, PDN, Cambridge). I found that PzT MO had two mismatches with

the *Xenopus laevis* *Piezo1.L* sequence. To improve the specificity of morpholino binding and minimise potential off-target effects, I designed Piezo1 morpholinos for *Xenopus laevis* (the morpholino information is given in Table 2). In this thesis, I used PzT MO to replicate previous experiments in the lab and PzL MO (as Piezo1.L rather than Piezo1.S translation is more likely to have been affected by the PzT MO).

**Table 2 Morpholino sequences to downregulate Piezo1.**

Morpholino	Sequence	3'end
Scr MO	5'- CCTCTTACCTCAGTTACAATTTAT A -3'	Carboxyfluorescein
PzT MO	5'- <u>C</u> <u>A</u> CAGAGGACTTGCAGTTCCATC CC -3'	Carboxyfluorescein/ Lissamine
Pz1L MO	5'- <u>C</u> <u>G</u> C <u>A</u> C <u>A</u> <u>G</u> GACTTGCAGTTCCATC <u>C</u> C -3'	Carboxyfluorescein/ Lissamine
PzS MO	5'- <u>C</u> <u>G</u> C <u>A</u> C <u>A</u> <u>A</u> GACTTGCAGTTCCATC <u>T</u> C -3'	Carboxyfluorescein

**Translation-blocking morpholino sequence information. Base differences between PzT MO and PzL/PzS MO are underlined in black, differences between PzL MO and PzS are highlighted in yellow.**

To microinject morpholinos, freshly fertilised embryos were chemically dejellied in 2% w/v Cysteine in 0.1 × MBS, pH 8.0, for 2-5 minutes. Embryos were visually inspected under a stereomicroscope and when the jelly coat was no longer visible, the embryos were thoroughly but carefully rinsed in several washes with 0.1 × MBS. The dejellied embryos were gently transferred to a mesh-bottomed dish containing 4% w/v Ficoll in 0.1 × MBS, pH 7.5.

Glass capillary tubes (1.0 mm OD by 0.5 mm ID, Harvard Apparatus) were pulled into needles and loaded with a solution of 3 ng/nL morpholino. Needles were then affixed to a micromanipulator (connected to a FemtoJet 4X microinjector (Eppendorf)) and manually

broken with forceps. The droplet size was calibrated in mineral oil, using a reticule in the microscope eyepiece, to dispense ~5 nL of morpholino.

A single pulse of morpholino (15 ng) was injected into one or both dorsal blastomeres of 4-cell stage embryos. The embryos were transferred to  $0.1 \times$  MBS after 1 hour and left to develop in 12-18°C rearing incubators.

Prior to any downstream use, embryos were screened using a fluorescence stereomicroscope. As the morpholinos were designed with a fluorescent 3' tag, this ensured that only embryos presenting a clear signal in the tissues of interest were selected.

## 2.1.8 Visualising the optic tract in intact brains

### 2.1.8.1 Lipophilic labelling using DiI.

*Xenopus* embryos at the development stage of interest were fixed using 4% PFA in  $1 \times$  PBS for 2 hours at room temperature or overnight at 4°C. Post-fixation, embryos were rinsed in  $1 \times$  PBS and laterally pinned onto Sylgard-184 coated dishes. DiI (1,1'-Dioctadecyl-3,3,3',3'-Tetramethylindocarbocyanine Perchlorate, Molecular Probes) crystals were dissolved in 100% ethanol and heated for a few minutes at 65°C. The DiI solution was then loaded into microinjection glass capillaries (1.0 mm OD by 0.78 mm ID, Harvard Apparatus) and mounted. DiI was injected into the eye, between the boundary of the lens and retina, until a full roseate ring formed as described in (Wizenmann et al., 2009). After 24-28 hours in  $1 \times$  PBS at room temperature, the brains were dissected and mounted in  $1 \times$  PBS in the lateral view. This method was used to visualise the optic tract (OT) of wild-type embryos at various development stages and of Piezo1 downregulated embryos at stage 40.

### 2.1.8.2 Horse radish peroxidase (HRP) labelling

To visualise the OT and cell nuclei for cell density measurements at stage 40, the lens primordia of embryos were removed and a plug of semidried HRP (30% HRP in 1% lysolecithin) was placed in the lens cavity. After 30 min, embryos were fixed in 4% PFA for 1 hour at room temperature. Post-fixation, brains were dissected out and reacted with diaminobenzidine (DAB; 1 DAB tablet dissolved into 15 ml 0.1 M Tris buffer and 12  $\mu$ l 30% H<sub>2</sub>O<sub>2</sub>). Brains were then mounted in Fluoromount-G (eBioscience, UK). This method was used to visualise the OT of wild-type embryos at stage 40.

Z-stack images of the OTs of both DiI and HRP labelled brains were obtained using a confocal microscope (SP8, Leica Microsystems, UK; 20× air, NA = 0.75; z-step size = 1 µm).

### 2.1.9 Cryosectioning *Xenopus* embryos

BI2536 inhibitor or mock-treated embryos were fixed at the requisite stages in 4% PFA overnight at 4°C, washed thrice in PBS for 10 min, and equilibrated in 30% sucrose for 1 hour at 4°C. The embryos were embedded in optimum cutting temperature compound (OCT, VWR). 12 µm-thick coronal sections were made and collected on Superfrost plus slides (ThermoScientific). Sections were dried and frozen at -20°C, immunostained (detailed in 2.4.3), and imaged.

### 2.1.10 Brain targeted electroporation

To more finely control the spatio-temporal knockdown of Semaphorin3A (Sema3A), a targeted electroporation method was used, as described in (Falk et al., 2007).

Vitelline membranes were manually removed from stage 28 embryos using fine tipped forceps. Embryos were anaesthetised in (0.04% w/v MS222, 1 × PSF, in 1.0 × MBS, pH 7.6). and an individual embryo was placed belly down in a custom fabricated, electroporation chamber (courtesy of the Holt lab). The same chamber was used in all experiments to ensure that electrode and embryo positioning were as reproducible as possible.

The electroporation chamber is a cross-shaped chamber, formed by two channels carved perpendicular to each other in a Sylgard-coated dish. An embryo was positioned in the longitudinal channel of the cross, while 0.5 mm wide platinum electrodes were positioned on either side of the embryo in the transverse channels. Glass capillaries (1.0 mm OD by 0.5 mm ID) were loaded with 1 mM fluorescein-labelled Sema3A MO or standard control (Scr MO) morpholino solution (Table 3) and placed in a micromanipulator connected to a picospritzer (Intracel).

**Table 3 Morpholino sequences for brain electroporations.**

Morpholino	Sequence	3'end
Scr MO	5'- CCTCTTACCTCAGTTACAATTTA TA -3'	Carboxyfluoresce in
Sema3A MO	5'- TGCAATCCAGGTCAGAGAGCCC ATG -3' from (Leung et al., 2013)	Carboxyfluoresce in

The capillary was inserted between the eye and brain, such that the target region was between the positive electrode and capillary. Eight pulses of morpholino were dispensed, followed by eight 18 V shocks, for a duration of 50 ms, spaced one second apart using a TSS20 Ovodyne electroporator (Intracel). The electrodes were then removed, and the embryo was gently transferred with a Pasteur pipette to a dish containing  $0.1 \times$  MBS and left to develop at 20°C to stage 40.

Embryonic brains were exposed (refer to 2.1.2) and screened for fluorescence at the telencephalon region of the brain. Embryos with signal at the region of the brain where Sema3A is normally expressed were selected for AFM measurements.

## 2.2 Altering and measuring the mechanical environment

### 2.2.1 Compliant tissue culture substrate (hydrogel) fabrication

Single-stiffness hydroxy-acrylamide substrates were prepared as in (Moshayedi et al., 2010). Briefly, glass-bottom Petri dishes were treated with 0.1M sodium hydroxide, silanized with (3-Aminopropyl)- trimethoxysilane (APTMS) for 2-3 minutes, washed thoroughly, and incubated in 5% glutaraldehyde for 30 minutes.

The compliant substrates were prepared using the indicated compositions (Table 4) of acrylamide, bis-acrylamide (Fisher Scientific), and hydroxy-acrylamide in PBS. The composition of acrylamide, bis-acrylamide, and hydroxy-acrylamide used to achieve these specific gel stiffnesses was previously determined by rheological and atomic force microscopy measurements.

**Table 4 Composition of acrylamide, bis-acrylamide, and hydroxy-acrylamide in 500 $\mu$ l of gel premix.**

Shear Modulus (kPa)	% acrylamide	% bis-acrylamide	% hydroxy-acrylamide
0.1	2.4	0.07	2.4
1	3.5	0.10	1.2

Gel premixes were degassed under vacuum, and gelation initialized by addition of freshly prepared 1% ammonium persulfate and 0.3% tetramethylethylenediamine (TEMED, Invitrogen). A small volume of premix was pipetted onto the treated surface of the glass bottom dishes, and covered with a “top” coverslip, made hydrophobic by treating with Rain-X (Shell Car Care International Ltd, UK) for at least 30 minutes. After the residual premix had solidified, gels were soaked in 1 $\times$  PBS and “top” coverslips were removed with forceps and gels were washed with twice with 1 $\times$  PBS and UV-treated for 30 minutes. One sample per gel stiffness was measured using atomic force microscopy to ensure that the substrates were indeed at the intended stiffness prior to culturing cells on them. Post UV-treatment, gels were functionalized with 10  $\mu$ g/ml Poly-D-lysine overnight, followed by 5  $\mu$ g/ml laminin for 2-3 hours.

## 2.2.2 Atomic Force Microscopy Measurements

### 2.2.2.1 Cantilever and microscope setup

The spring constants,  $k$ , of tipless cantilevers were determined using the thermal noise method (Hutter and Bechhoefer, 1993) to with the AFM Software (JPK instruments).

Only cantilevers with  $k$  between 0.01 to 0.05 N/m were used for stiffness measurements of *in vivo* embryo brains and compliant hydroxy-acrylamide substrates.

Spherical monodisperse polystyrene beads (microParticles GmbH) with a diameter of  $37.28 \pm 0.34$   $\mu$ m were affixed to the end of the tipless cantilevers using M-bond 610 heat-curing glue (MicroMeasurements).

The beaded cantilevers were mounted onto a CellHesion-200 AFM head (JPK Instruments), on a Zeiss Axio Observer.A1 inverted microscope with a motorized stage (JPK instruments). A modified AxioZoom V.16 system (Zeiss) on a custom-built support

arm above the AFM head, described in (Thompson, Pillai et al., 2019), was used to enable upright imaging of the *Xenopus* embryonic brain surface.

#### 2.2.2.2 Sample preparation and measuring conditions

*Xenopus* embryonic brains were exposed (2.1.2) to allow for tissue stiffness measurements *in vivo* in the intact embryo. Any excess dura that regrew following overnight exposure to *in vivo* treatments, was removed prior to making AFM measurements. Embryos were immobilised on Sylgard-184 coated dishes with bent 0.2 mm minuten pins in *Xenopus* exposed brain medium, with the exposed hemisphere facing up. Stiffness measurements were performed at room temperature, between 20-22°C.

#### 2.2.2.3 Tissue stiffness mapping

All brain stiffness mapping in this thesis was conducted on stage 40 embryos. To mechanically characterize the effects of downregulating Piezo, measurements were made in embryos with one or both dorsal blastomeres injected with a morpholino (resulting in tissue specific or whole CNS Piezo1 depletion respectively). Embryos treated chemically to perturb tissue stiffness, cell proliferation, or MSC activity (detailed in 2.1.3) were exposed to the treatments from stage 33/34 and left to develop to stage 40 at 20°C, when stiffness measurements were conducted.

Samples were placed on a motorized stage (JPK instruments), controlled by custom-written Python scripts. A user-defined rectangular grid of measurement points was set to include the forebrain and tectal areas of the embryonic brain. Images were taken of the whole embryo -to enable staging (before and after measurements) and at each point that was being mapped using a CCD camera (Image Source, UK). Measurements were made of the selected region at every 20 or 25  $\mu\text{m}$  in a raster scan, using a custom-written script. The cantilever was retracted by 100  $\mu\text{m}$  before the stage shifted to the next position. The setpoint force was 10 nN at an approach speed of 5  $\mu\text{m}/\text{s}$  with a sample rate of 1000 Hz. Custom scripts can be obtained at <https://github.com/FranzeLab/Instrument-Control>.

#### 2.2.2.4 Measuring hydroxy-acrylamide gels

Compliant substrate samples were placed on the motorized stage (JPK instruments) and multiple measurements were made at three to five random locations on the substrate. The AFM setup and measuring conditions were identical to the stiffness mapping experiments,

with the exception that the substrates were measured in  $1 \times$  PBS rather than in *Xenopus* exposed brain medium.

## 2.3 RNA visualization and quantification

### 2.3.1 Preparation of Digoxigenin-labelled RNA probes

A pCS2+*-XenopusSema3A* plasmid (kindly provided by the lab of Christine Holt (Leung et al., 2013)) was used as template for producing digoxigenin (DIG)-labelled antisense riboprobes. The plasmid DNA was extracted from a filter paper spot using Tris-EDTA buffer heated to 50-60°C. The plasmid was then transformed into Library Efficiency<sup>®</sup> DH5 $\alpha$ <sup>™</sup> cells (Thermo Fisher) by applying 45 seconds of heat shock at 45°C. Transformed cells were spread onto media plates (Luria Broth (LB, Invitrogen) + Bacto-Agar (BD)) with 100  $\mu$ g/mL of ampicillin and left to grow overnight at 37°C. Individual colonies were selected, and amplified via shaking incubation overnight at 37°C in 5 mL of LB with 100  $\mu$ g/mL ampicillin in a round bottom conical tube. Plasmid DNA was subsequently extracted using a Miniprep kit (Qiagen or New England Biolabs).

A specific region of the purified plasmid was polymerase chain reaction (PCR) amplified and a T3 RNA polymerase promoter sequence overhang was artificially added at the 3'-end to enable synthesis of the anti-sense strand. The plasmid contains the full-length coding sequence of *sema3A*, which at 2325 bases is above the optimum length for an *in situ* probe. I therefore made probes using the full length, and the first and last ~800 bases of *sema3A*. All probes produced identical patterning. Subsequently, in this thesis I used the probe generated from the last ~800 bases of *sema3A*. As the expression pattern of *sema3A* in stage 40 embryos has not been previously shown in whole embryos, Sox2 probes (a generous gift from the lab of Clare Baker) were made and tested alongside the Sema3A probes as a positive control (*sox2* patterning was consistent with published images, suggesting that the protocol we adapted worked for whole *Xenopus* embryos, positive control data is not shown). The PCR primer sequences used are detailed in Table 5. A Phusion-High Fidelity DNA Polymerase Kit (New England Biolabs) was used according to manufacturer instructions, to PCR amplify the whole construct or specific regions.

All PCR products (and the unlinearized plasmids) were run on a 1% agarose gel in Tris-Acetate-EDTA running buffer containing 0.005% RedSafe, to ensure that a single product

of the correct size was obtained. The product identities were verified by Sanger sequencing done by the Sanger Sequencing Facility at the Department of Biochemistry (University of Cambridge).

**Table 5 PCR primers used in amplifying specific regions of the plasmid and for artificially inserting a T3 RNA polymerase promoter site.**

Probe	Forward primer	Reverse primer	Product length
Sema3A (full length)	ATGGGCTCTCTGACCTGG ATTGCATTTC	TAAAATAGCAATTA ACCCTCACTAAAGG CAGACACTCCTTGG TGCCCTCTCAAATTC A	2352 bases
Sema3A (first 800 bases)	ATGGGCTCTCTGACCTGG ATTGCATTTC	TAAAATAGCAATTA ACCCTCACTAAAGG CACCCCATCTATGG CATTTTCACGGAAG	796 bases
Sema3A (last 800 bases)	TGGAAAAGCTTGTGCTGA GTGTTGCCTTG	TAAAATAGCAATTA ACCCTCACTAAAGG CAGACACTCCTTGG TGCCCTCTCAAATTC A	763 bases
Sox2	GGCCGAGAAAAGACCCTT CA	TAAAATAGCAATTA ACCCTCACTAAAGT GCCCTTTTTCACATG TGCG	705 bases

### 2.3.2 RNA synthesis of probe

To prepare DIG- labelled RNA from the PCR product, the following components were mixed in a 1.5 mL RNase-free Eppendorf tube on ice (5 µl PCR product, 2µl DIG labelling mix, 2 µl 10x transcription buffer, 1 µl RNase inhibitor, 2 µl T3 RNA polymerase and nuclease free water to 20 µl) and then incubated at 37°C for 2 hours. 1 µl of RNase-free DNase was added for 15 minutes at 37°C.

1 µl of the product was measured using a Nanodrop Spectrophotometer (Thermo Scientific) to measure the quality and quantity of RNA synthesized. Another 1 µl of the

product was run on a 1% agarose gel in Tris-Acetate-EDTA running buffer containing 0.005% RedSafe, to ensure that a single product of the correct size was obtained.

The remainder of the product was topped up to 90  $\mu$ l with nuclease free water and 10  $\mu$ l of 8M LiCl was added. Finally, 300  $\mu$ l of 100% ethanol was added, and the tube contents were mixed and incubated overnight at -20°C.

RNA was precipitated and purified by centrifuging the product at 15 000 G for 25 minutes at room temperature, carefully removing the supernatant, and adding 300  $\mu$ l of 70% ethanol. This was then centrifuged at 15 000 G for 5 minutes at room temperature. All ethanol was carefully removed, and the remaining pellet was air-dried for 5-10 minutes on the bench, by inverting the tubes over clean tissue. The pellet was then carefully resuspended in 22  $\mu$ l of nuclease free water, by gently flicking the tube (vortexing is too harsh and pipetting the solution up and down results in a loss of material to the pipette tip). The probe RNA concentration and quality were measured using a Nanodrop Spectrophotometer and the end concentration was adjusted to 250 ng/ $\mu$ l with hybridization buffer. Probes were stored at -20°C.

### 2.3.3 Whole embryo *in situ* hybridization

Whole-embryo *in situ* hybridization was adapted from (O'Neill et al., 2007). *Xenopus* embryos were fixed using a modified Carnoy's fixative (6 parts 100% ethanol, 3 parts 37% formaldehyde, 1 part glacial acetic acid) for 4 hours at room temperature, overnight at 4°C. Embryos were then rinsed in 70% ethanol in PTw (0.1% Tween-20 in nuclease-free PBS) and dehydrated in three thirty minute 100% ethanol washes. The embryos were then stored at -20°C until the *in situ* hybridization could be carried out.

Embryos were rehydrated through an ethanol gradient into nuclease-free PBS (100%, 75%, 50%, 25% ethanol in PBS), washed thrice in PTw for 15 minutes per wash and bleached in bleaching solution (5% formamide, 25% 2  $\times$  SSC (0.3M NaCl, 0.03M sodium citrate), 28% H<sub>2</sub>O<sub>2</sub> in nuclease -free water) under a strong light source for 25-45 minutes, until the eye primordia of embryos turned from black to white. Embryos were washed thrice in PTw for 10 minutes and then treated with 20 $\mu$ g of proteinase K (Roche) for 10-15 minutes at room temperature, without shaking. Embryos were washed thrice in PTw for 10 minutes and post-fixed in 4% PFA and 1% glutaraldehyde in nuclease -free PBS for 2 hours at room temperature, then washed in PTw thrice for 15 minutes, followed by a prewash solution containing 1:1 solution of PTw and washing solution (50% formamide, 5% 20x

SSC (3M NaCl, 0.3M sodium citrate), 0.1% Tween20 in nuclease -free water) for 10 minutes at room temperature, and finally in washing solution for 10 minutes at room temperature. Specimens were prehybridised in hybridisation solution (1x salt solution [0.2M NaCl, 10mM Tris pH7.5, 5mM NaH<sub>2</sub>PO<sub>4</sub>.H<sub>2</sub>O, 5mM Na<sub>2</sub>HPO<sub>4</sub>, 5mM EDTA], 50% formamide, 10% dextran sulphate, 1mg/ml yeast tRNA, 1 × Denhardt's Solution) for 3 hours at 68-70°C. Hybridisation was performed overnight at 68-70°C with a 3:500 dilution of probe to pre-warmed hybridization solution.

Probe hybridized embryos were washed 4-6 times for 30 minutes each at 68-70°C in pre-warmed wash solution (50% formamide, 1xSSC, 0.1% Tween-20), once in a 1:1 solution of washing solution and MABT (0.1M maleic acid, 150mM NaCl, 0.1% Tween-20, pH 7.5) at 68-70°C then thrice for 10 minutes at room temperature in MABT. Embryos were incubated in a blocking solution (20% sheep serum (Sigma), 2% Boehringer blocking reagent in MABT) for 2-3 hours at room temperature and then incubated overnight at 4°C with a 1:2000 dilution of anti-digoxigenin (Roche) antibody in blocking buffer.

Embryos were then washed in MABT (two quick rinses then eight 30-minute washes) and equilibrated in NTMT (100mM NaCl, 100mM Tris pH 9.5, 50mM MgCl<sub>2</sub>, 0.1% Tween-20) with three 20-minute room temperature washes. The colour reaction was initiated by removing the NTMT and adding BM Purple (Roche) to the embryos and stopped by transferring into PTw. Embryos were rinsed several times in PTw and post-fixed in 4% PFA for 2 hours at room temperature or overnight at 4°C. Embryos were then rinsed several times in PTw and transferred to an agar-coated petri dish with PBS and imaged using a Leica MZFLIII stereomicroscope with QImaging microPublished Color RTV camera, and the QCapture Pro 7 software.

#### 2.3.4 Whole brain *in situ* hybridization

Whole-mount *in situ* hybridization was adapted from (Shimamura et al., 1994). Embryos were collected in cold PBS, fixed with 4% paraformaldehyde/PBS for 2 hours at room temperature. Whole brains were carefully dissected out, in nuclease-free PBS, and washed thrice with cold PTw (0.1% Tween-20 in RNase-free PBS). Samples were transferred to a 12-well plate with mesh adapters and treated with 20 µg/ml of proteinase K for 5 minutes at room temperature, then washed twice for five minutes in freshly prepared 2 mg/ml glycine in PTw. Brains were post-fixed in 0.2%glutaldehyde in PBS, for 20 minutes at room temperature. Embryos were washed thrice for five minutes in PTw. After treatment

## Chapter 2: Methods

with freshly prepared 0.1% sodium borohydride in PTw for 20 minutes, brains were washed a further three times in PTw, and twice in hybridization buffer (50% formamide, 750 mM NaCl, 1 × PE (10mM PIPES pH6.8; 1mM EDTA), 100 µg/ml yeast t-RNA, 0.05% heparin and 1% SDS in nuclease-free water) for five minutes at room temperature. Samples were pre-hybridized for at least 1 hour at 63°C in a hybridization oven, in a humidity chamber, and samples were hybridized with 2 µg/ml of probe in hybridization solution overnight at 63°C.

Samples were then washed in hybridization buffer at 63°C for 30 minutes, and twice for 30 mins with 300 mM NaCl, 1 × PE, and 1% SDS at 63°C. Followed by two 30-minute washes in 50 mM NaCl, 1 × PE, and 0.1% SDS at 50°C, and a brief rinse in NTE buffer (500 mM NaCl, 10 mM Tris-HCl pH 8.0; 1mM EDTA). The samples were then treated with 100 µg/ml RNaseA and 100U/mL of RNaseT1 in NTE for 60 minutes at 37°C and rinsed briefly in NTE. The samples were then washed in (50% formamide, 300 mM NaCl, 1 × PE, 1%SDS) at 50°C for 30 minutes, followed by (50% formamide, 150 mM NaCl, 1 × PE, 0.1% Tween-20) at 50°C for 30 minutes. Finally, the samples were washed twice at room temperature, and once for 20 minutes with (500 mM NaCl, 1 × PE, 0.1% Tween-20) at 70°C to inactivate endogenous alkaline phosphatases. Samples were blocked in 1 × MABT (0.1M maleic acid, 150mM NaCl, 0.1% Tween-20, pH 7.5), with 2mM levamisole, 2% Boehringer blocking reagent, and subsequently incubated overnight at 4°C with a 1:5000 dilution of anti-digoxigenin antibody in blocking reagent. After thorough washings, thrice quickly and 5-6 times for an hour each with freshly made 2mM levamisole in 1 × MABT, samples were washed twice for 20 minutes with 2mM levamisole in NTMT. The colour reaction was initiated by removing the NTMT and adding BM Purple (Roche) to the embryos and stopped with the changes of PTw containing 1mM EDTA and stored at 4°C. Samples were observed and imaged as done for the whole-mount embryo samples.

### 2.3.5 Quantitative polymerase chain reaction (qPCR)

#### 2.3.5.1 RNA extraction and cDNA conversion

RNA was extracted from specific regions of the brain that were dissected out, from acutely dissociated neuroepithelia, and from dissociated neuroepithelia that were cultured on gels for 24 hours using the Qiagen RNA extraction kits in Table 6.

Piezo1 downregulated and wild-type chondroitin sulphate embryos and their respective controls were fixed in a modified Carnoy's (described in section 2.3.3) or MEMFA (0.1 M MOPS, pH 7.4, 2 mM EGTA, 1 mM MgSO<sub>4</sub>, 3.7% formaldehyde for 2 hours at room temperature) fixative. Fixed embryos were stored in ethanol and methanol respectively and stored at -20°C until *in situ* hybridizations (described in 2.3.3) or RNA extractions for qPCR were done.

Brain tissue regions were dissected out of fixed embryos and placed in Buffer PKD (supplied in miRNeasy FFPE kit). The tissue was mechanically homogenized by pipetting in the buffer. The extraction was done according to manufacturer instructions. To comply with recommended tissue volumes for optimal RNA extraction, two brain regions were used per condition.

For *in vitro* neuroepithelia cells cultured on hydrogels, Xenopus culture medium was removed and replaced with 350 µl RLT Plus buffer from the RNeasy Plus Micro kit, with 1% v/v β-mercaptoethanol. The entire gel was scraped from the glass dish using a scalpel and transferred to a sterile 1.5 ml Eppendorf tube. The gel-cell mix was homogenized by pipetting and vortexing. The extraction was done following manufacturer instructions.

RNA was also extracted from acutely dissociated cells from the neuroepithelia.

RNA extracted was measured for yield and purity using a NanoDrop Spectrophotometer.

**Table 6 Kits used for RNA extractions.**

Qiagen Kit	Catalogue number	Samples
RNeasy Plus Micro Kit	74034	<i>In vitro</i> cultures of dissociated wild-type brain cells on compliant substrates.

miRNeasy FFPE Kit	217504	RNA extraction from brain regions of MEMFA- or Modified Carnoy's- fixed embryos (Piezo1 downregulated and chondroitin sulphate treated brains)
----------------------	--------	--

For a given experiment, RNA concentrations of all samples were adjusted to that of the lowest concentration sample prior to cDNA synthesis.

RNA was then reverse transcribed into cDNA using a SuperScript III First Strand Synthesis System (Invitrogen) or the Sensiscript RT Kit (Qiagen), according to the manufacturer's instructions.

### 2.3.5.2 cDNA preamplification

As the micro dissections and dissociated cells on compliant substrates typically result in low RNA yields. cDNA was pre-amplified using the TaqMan PreAmp Master Mix kit (Thermo Fisher Scientific). The kits allow for pre-amplification of small amounts of cDNA without the introduction of amplification biases.

### 2.3.5.3 qPCR

Custom designed TaqMan Gene Expression Assays (20 ×) designed for FAM-labelled *Xenopus laevis sema3A.L*, and VIC-labelled reference genes, in this work, *Xenopus laevis mcts1.L*, *mtch2.L*, *slc35b1.L*, *sub1.L*. These reference genes (and primer design) were selected based on (Mughal et al., 2018). Mughal et al. evaluated the stability of various candidate genes using RT-qPCR for various stages of early *Xenopus laevis* embryonic and brain development. (*mcts1*: malignant T-cell amplified sequence 1; *mtch2*: mitochondrial carrier 2; *slc35b1*: solute carrier family 35 member B1; *sub1*: SUB1 homolog, transcriptional regulator. *Xenopus laevis* are allotetraploids that often have two copies of a certain gene. 'L' and 'S' indicate the large and small chromosomes respectively).

qPCR was performed using the Light Cycler 480 II (Roche) on 96-well Standard (0.2 mL) Plates. Each well contained 2.5 µl cDNA at a ratio of 1:5 with 1 x TE Buffer, 0.5 µl each of FAM-*sema3AL* and a VIC-labelled reference TaqMan Gene Expression Assay (20 ×), 5 µl TaqMan Fast Advance Master Mix (ThermoFisher) and RNase-free water to a total reaction volume of 10 µl per well. The plates were vortexed and centrifuged at 3000 RPM for 2 minutes.

The qPCR reaction for each sample and reference gene combinations consisted of three technical replicates and used RNase-free water as negative controls. The data was analysed

using the LightCycler 480 SW 1.5.1 (Roche) software. Threshold cycle ( $C_t$ ) values are obtained from this software and used to calculate the delta-delta- $C_t$  (Livak and Schmittgen, 2001), to quantify relative differences between Sema3A and individual reference genes against the control condition for whole brain regions, and against acutely dissociated cells for the *in vitro* experiments.

## 2.4 Protein quantification and visualization

### 2.4.1 Western blots

Heads of stage 39–41 *Xenopus* embryos were dissected and mechanically homogenized in lysis buffer (150mM NaCl, 1% Triton-X, 0.5% sodium deoxycholate, 0.1% sodium dodecyl sulfate, 50mM Tris buffer; pH8, 1× Halt Protease and Phosphatase Inhibitor Cocktail from Thermo Scientific). Extracts were lysed by rotating in a 4°C cold room for 30 minutes and then centrifuged at 20,000 G at 4°C. The supernatant was collected, and protein concentrations of the lysates were calculated with the Bradford calorimetric assay. For Western Blots 1mg/ml samples were prepared in SDS sample buffer (60mM Tris-HCl, 2% w/v SDS, 5% v/v beta-mercaptoethanol, 10% v/v glycerol, 0.01% v/v bromophenol blue). Samples were run on 4–12% Bis-Tris gradient gels (Invitrogen) at 20mA per gel in MOPS SDS buffer (NuPage). The proteins were transferred to a nitrocellulose membrane for 16 hours at 30V at 4°C using a wet Biorad Transfer System.

The most abundant protein bands were visualized with PonceauS. Membranes were blocked for 1 hour in blocking solution (5% skim milk powder diluted in TBST (20mM Tris buffer, 0.137M NaCl, 0.05% Tween-20; pH7.6)) and then incubated 2 hours at RT in fresh blocking buffer supplemented with polyclonal rabbit anti-Piezo1 primary antibody (Abcam ab 82336, 1: 500 or Novus Biologicals NBP1-78446; 1:500 dilution), and monoclonal mouse anti- $\alpha$ -tubulin (Abcam, ab7291; 1:10,000 dilution) as a loading control. The nitrocellulose membranes were washed in TBST and incubated in fresh blocking buffer supplemented with polyclonal goat anti-rabbit antibody conjugated to horseradish peroxidase (HRP) (Abcam, ab97080; 1:10,000 dilution) for Piezo1, or a polyclonal goat anti-mouse antibody conjugated to HRP (Abcam, ab6789; 1:10,000 dilution) for  $\alpha$ -tubulin for 1 hour at RT. Western blots were developed using the Novex ECL HRP Chemiluminescent Substrate Reagent kit (Invitrogen) and either an X-ray developer or a LiCor FC imager. For Sema3A detection an anti-rabbit IRDye 800CW antibody (LiCor)

was used and the fluorescent signal intensity was measured in the C800 channel of the LiCor FC. The signal intensity was normalized against signal intensity of anti-mouse IRDye 680 antibody (LiCor) detecting  $\alpha$ -Tubulin.

X-ray films were scanned, and densitometry was performed on 8-bit greyscale images imported into Fiji. The Fiji Gel analysis tool was used to correct for background and to measure relative band intensities. LiCor images were analyzed using ImageStudioLite software supplied with the machine. The ratio of relative intensities of Piezo1 to  $\alpha$ -tubulin was used to compare different groups.

### 2.4.2 Wholemout brain immunohistochemistry

Fixed whole brains from stage 40 embryos were permeabilized at room temperature for 30 minutes with PBS + 0.2% Bovine serum albumin + 0.1% Triton-X (PBT). Tissue was blocked for 45-60 minutes with 10% Donkey serum in PBT, followed by an overnight  $\alpha$ -Piezo 1 primary antibody incubation (Abcam ab82336, 1:200 dilution) at 4°C. Tissues were washed thrice in PBS and then incubated with Dnk  $\alpha$ -Rb 568 secondary antibodies (Abcam, ab175470, 1:500 dilution) at room temperature. Brains were laterally mounted in Fluoromount-G (eBioscience) for imaging.

Visualizing cell nuclei, Cell nuclei were labelled using 1  $\mu$ g/ml 4,6-diamidino-2-phenylindole (DAPI). HRP-labelled optic tracts were mounted in Fluoromount-G, while DiI-labelled optic tracts were mounted in 1  $\times$  PBS. Z-stack images of the of brains were obtained using a confocal microscope (SP8, Leica Microsystems, UK; 20 $\times$  air, NA = 0.75; z-step size = 1  $\mu$ m).

### 2.4.3 Immunohistochemistry tissue cross-sections

Sectioned embryonic head tissue on slides (from 2.1.9) were washed thrice in PBS, followed by three 10 min washes in PBS with 0.1% TritonX (PBT). The sections were blocked in 5% goat serum in PBT for 30–45 min and incubated with rabbit polyclonal anti-phospho-Histone H3 (Ser10) (EMD Millipore, 06–570, 1:1000 dilution) overnight at 4°C or for 2 hr at room temperature. This was followed by three 10 min washes in PBS and secondary antibody incubation with goat anti-rabbit Alexa Fluor 594 (Abcam, ab150084, 1:500 dilution) for 45–60 min. The slides were washed twice for 10 min with PBS and nuclei were labelled using 1  $\mu$ g/ml DAPI. Sections were mounted with Fluoromount-G and imaged with a confocal microscope (SP8, Leica Microsystems, UK; 20 $\times$ /0.75 air and

63×/1.4 oil, z-step size = 1 μm). Only slices with eye tissue present were selected, to reliably ensure that the brain sections imaged and analysed were indeed exposed to the treatment solutions. This enabled the easy identification of intact- versus exposed- brain side hemispheres in each section.

#### 2.4.4 Immunocytochemistry of RGC axons *in vitro*

To visualize Piezo1 distribution and cytoskeletal elements found in RGC axons cultured on glass or hydrogels, eye primordia were fixed after 24 hours in culture in 2% PFA + 7.5% sucrose and permeabilized for 5 minutes in 0.1% Triton-X. Axons were quickly washed 2-3 times. All intermediary washes were done in 1 × PBS with 0.001% Triton-X. Cultures were blocked in 5% donkey serum for 45-60 minutes and were incubated with primary antibodies overnight at 4°C. Cultures were briefly washed thrice, and incubated with secondary antibodies for 45 minutes at room temperature. Cultures were washed thrice for 20-30 minutes with PBS. If phalloidin was used to visualize actin, the second wash step post-secondary antibody incubation was substituted with a phalloidin incubation (phalloidin-Alexa Fluor 488, Life Technologies) for 20-45 minutes. Images of axons and growth cones were taken using a Nikon Eclipse TE2000-U inverted fluorescence microscope (60× oil immersion, NA = 1.4).

**Table 7 Summary of primary and secondary antibodies used.**

Primary antibody	Manufacturer	Catalogue number	Dilution	Secondary antibody	Dilution
Gt $\alpha$ -Piezo 1	Santa Cruz	sc-164319  (used with peptide sc-164319 P)	0.18055556	Dnk $\alpha$ -Gt 488 (Sigma-Aldrich, sab4600032) or 568 (Abcam, ab175704)	0.73611111
Rb $\alpha$ -Piezo 1	Abcam	ab82336	0.18055556	Dnk $\alpha$ -Rb 488 (Abcam, ab150073) or 568 (Abcam, ab175470)	0.73611111
Rb $\alpha$ -beta tubulin	Abcam	ab6046	0.73611111	Dnk $\alpha$ -Rb 488 (Abcam, ab150073) or 633 (Sigma-Aldrich, sab4600127)	0.73611111
Ms $\alpha$ -alpha tubulin	Abcam	ab7291	0.73611111	Dnk $\alpha$ -Ms 488 (Life Technologies, A-21202) or 647 (Abcam, ab150107)	0.73611111
Rb $\alpha$ -phospho-Histone H3 (Ser10)	EMD Millipore	06-570	0.73611111	Gt $\alpha$ -Rb 594 (Abcam, ab150084)	0.38888889

***Dnk: donkey, Gt: goat, Ms: mouse, Rb: rabbit.***

## 2.5 Analysis

### 2.5.1 OT phenotype analysis

Only samples that were mounted with the brain positioned properly and with visible tracts were used in the phenotype and elongation analysis (below). DiI-labelled images were randomized and OTs with normal projections (axons reach the tectum, without mid-OT bend defects or visibly straying axons), or that displayed defects such as mid-OT bend stalling, or axon misprojections were counted. Misprojections frequently occurred near the mid-OT bend but also included axons straying in other parts of the tract. Some of the misprojections include deviating at the mid-OT bend, bypassing the bend, avoiding the tectum or projecting into the telencephalon). Percentages of each phenotype were compared for the various experimental conditions.

### 2.5.2 OT elongation analysis

Maximum projections were made across 10-15  $\mu\text{m}$  confocal image stacks of wholemount brains with DiI-labelled OTs.

The OTs were manually outlined in Adobe Illustrator. Elongation of the OT was calculated by the major-to-minor axis ratio using a previously described (Koser et al., 2016) automated Matlab algorithm (<https://github.com/FranzeLab/Image-processing-and-analysis/tree/master/OT%20elongation>).

Briefly, the major and minor axes were determined by fitting ellipses, with the same normalized second central moment as the OT area, around the OTs.

### 2.5.3 AFM data analysis

Force-distance curves obtained from stiffness measurements were analysed with a custom-written MATLAB script (Christ et al., 2010; Koser et al., 2016; Thompson, Pillai et al., 2019) to obtain the reduced apparent elastic modulus  $\mathbf{K}$ . Raw AFM data were fitted to the Hertz model,

$$F = \frac{4}{3} \mathbf{K} \delta^{3/2} \sqrt{\mathbf{R}}$$

where  $F$  is the applied force,  $\mathbf{K}$  is the reduced apparent elastic modulus ( $\frac{E}{(1-\nu^2)}$ ; where  $E$  is the elastic modulus and  $\nu$  is the Poisson ratio),  $\mathbf{R}$  the radius of the indenter, and  $\delta$  is sample indentation (Crick and Yin, 2007; Hertz, 1882)

Force-distance curves were analysed at the maximum applied force  $F = 10$  nN. Points where the AFM data were not analysable were excluded. Criteria for excluding individual force-distance curves were (1) inability to apply linear fits through the baseline region, e.g. due to noise, and (2) inability to apply good-quality Hertzian fits to the indentation region, i.e. when the fit aligned poorly with the raw data. Values of  $K$  were converted to an 8-bit scale, colour-coded maps were generated using the desired MATLAB colourmap pre-set (the ‘hot’ pre-set was used in this thesis). Data were plotted as violin plots with individual measurements scattered over.

When brain stiffness was calculated by region, a MATLAB script (Koser et al., 2016) was used to manually select regions of interest using anatomical boundaries and fluorescence-labelling of structures as an approximate guide. Region of interest areas were selected 4 times and pixels defined as part of the region of interest if selected at least 3 out of the 4 times. Scripts can be obtained at <https://github.com/FranzeLab/AFM-data-analysis-and-processing>.

### 2.5.4 In situ hybridization

#### 2.5.4.1 Sema3A expression in the brain

Coloured *in situ* hybridization images were imported into Fiji and converted to greyscale. Two circular regions of interest (100  $\mu\text{m}$  radius) were selected, at the *sema3A* producing region (ROI) and the region of the brain adjacent to it (Ctrl). The mean signal intensities of these regions were measured. The normalized mean intensity used to compare different groups is the ratio of ROI to Ctrl region ( $\text{ROI}_{\text{mean intensity}} / \text{Ctrl}_{\text{mean intensity}}$ ).

#### 2.5.4.2 Sema3A expression in the whole embryo

Images were imported into Fiji. Piezo1 downregulated embryos are slightly smaller and lordotic, therefore a fairly featureless rectangular ROI (750  $\mu\text{m} \times 500 \mu\text{m}$ ) was selected (with the expression of the *sema3A* expressing band) to blind the experimenter to the embryo condition when scoring the embryos from high to low signal intensity. However, I ended up analysing these ROIs using methods less prone to experimenter subjectivity. Sequential perpendicular line profiles were made across the cropped ROI image. The median value and top percentile of each line profile was taken as the background and maximum intensity respectively. Fold changes of *sema3A* expression for each embryo was taken as the mean ( $\bar{X}$ ) ratio of the maximum intensity to background.

$$\text{Fold change} = \bar{X} \frac{\text{max intensity}}{\text{background}}$$

### 2.5.5 Analysis of the brain cross-section

Confocal images were taken with the 20 × air objective and imported into FIJI. Maximum projections were made of the stacks (z-stack height = 8 μm).

#### 2.5.5.1 Quantification of area

From the maximum projection images, the brain was identified in each section and both intact and exposed hemispheres were manually outlined. The area occupied by nuclei in each brain hemisphere was measured using the ‘Analyse > Measure’ tool. Normalised brain areas were obtained by calculating the ratio of exposed brain area to intact brain area.

#### 2.5.5.2 Quantification of phospho-histone H3 immunolabeling

Phosphorylated-histone3 positive (pH3+) cells were counted from the maximum projection image and normalized to the total measured brain area in each section. The data is presented as the number of pH3+ cells per 10,000 μm<sup>2</sup> of brain tissue.

$$\frac{\text{number of pH3 + cells}}{\text{brain area } (\mu\text{m}^2)} * 10,000$$

### 2.5.6 Cell body density analysis

Confocal image stacks of brains with fluorescently labelled OT and nuclei were imported into Fiji. For each brain, the image in which the mid-OT bend was in focus was selected. A maximum intensity projection was generated of this image and one image above and below it in the stack. Two 50 μm × 50 μm regions of interest were selected, rostral and caudal to the OT bend. Noise was removed with a Gaussian blur filter (sigma = 2.0). The resulting image was manually thresholded to capture all nuclei as accurately as possible. The image was binarised and the FIJI built-in function ‘Analyse Particle’ (size: 1–∞; circularity: 0.2–1.00) was used to determine the area in each region covered by nuclei. Relative cell body density was taken as the ratio of the area occupied by nuclei to the total region area.

## 2.6 Statistics

Data were collected from at least three independent experiments (data obtained from fewer than three biological replicates are disclosed in the figure legends).

Data were assessed for normality with a one-sample Kolmogorov-Smirnov test. If distribution did not deviate significantly from normal, a one or two sample t-test was used, when more than two samples were compared, data were analysed with an ANOVA followed by a Bonferroni post-hoc test. If data distributions significantly deviated from normal: (i) when two samples were compared, a Wilcoxon rank sum test was used, or if the data was paired (e.g. different regions within the same brain compared), a Wilcoxon signed-rank test was used, (ii) if more than two samples were compared, data were analysed with a Kruskal-Wallis test followed by a Tukey post-hoc test.



# 3 PIEZO1 IN THE *XENOPUS* EMBRYONIC BRAIN

*Xenopus* RGC axons sense and respond to mechanical cues from the environment, both *in vivo* and *in vitro* (Koser et al., 2016). A key player in acutely sensing and transducing mechanical cues into biochemical signalling in the cell, is mechanosensitive ion channels (MSCs). In this chapter, I downregulated the expression of the MSC Piezo1 in *Xenopus* RGCs and neuroepithelia and examined the MSC's distribution and functional results.

## 3.1 Piezo1 is found in neuroepithelia

I first investigated the distribution of Piezo1 at the brain surface via immunohistochemistry. Briefly, I applied commercially available antibodies against Piezo1 to stage 40 whole-mount brains, and visualized its distribution using confocal microscopy. I found that Piezo1 is homogenously distributed across the brain surface.

The observed distribution was relatively uniform across the brain, including the region occupied by the optic tract (made up of RGC axons originating from the eye on the contralateral side). Therefore, to confirm if the signal in that region originated from the neuroepithelia, the optic tract, or both, I ablated the eye primordia of early embryos, ensuring no RGC axons grew across the neuroepithelia. Ablated embryos were fixed and immunostained at stage 40. There was no discernible difference in signal between ablated and control brains at the region of the optic tract, suggesting that Piezo1 is evenly distributed across the neuroepithelia ( Figure 3-1 a).

## 3.2 Piezo1 is found in RGC axons

*Xenopus* RGC axons respond to mechanical cues from the environment, and as Piezo1 is present at the neuroepithelia, I was interested to see if this MSC was also present in RGC axons themselves. Thus, I cultured *Xenopus* eye primordia on glass-bottom microwell dishes. These explants produce axons exclusively from RGCs. Piezo1 was distributed in puncta mainly along the axon shaft (Figure 3-1 b).

To verify that the signal was not an *in vitro* artefact of growing axons on unnaturally stiff glass substrates, I then immunostained eye primordia explants, cultured on soft (0.1 kPa) and stiff (1.0 kPa) substrates. These substrate stiffnesses represent the lower and upper limits of brain tissue stiffness RGC axons would encounter *in vivo*. On both soft and stiff substrates, Piezo1 fluorescence was present as homogeneously distributed puncta along the axon shafts ( Figure 3-1 c). Hence, I found that the MSC Piezo1 is present in both RGC axons and neuroepithelia.

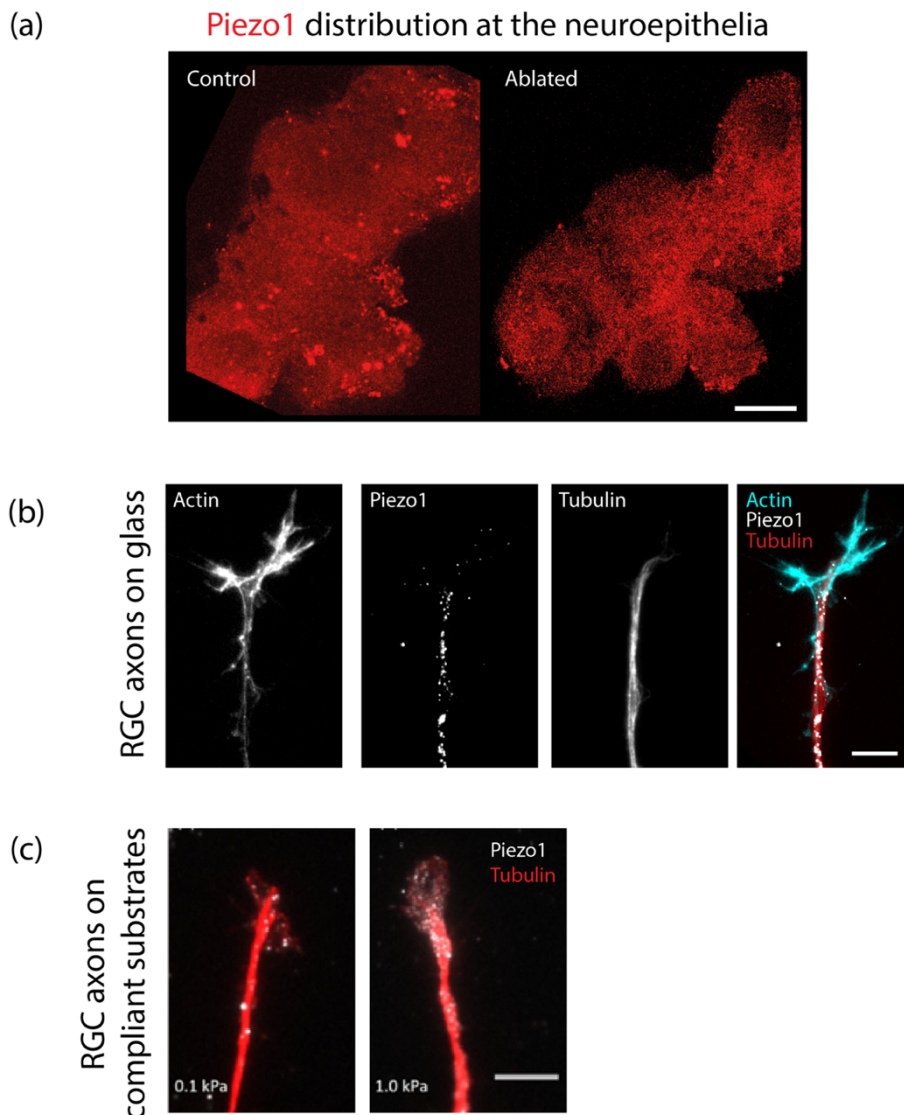


**Figure 3-1 Piezo1 is present in the neuroepithelia and in the axons of the optic tract.**

*(a) Lateral view of whole mount stage 40 embryonic brains in a control and optic tract ablated brain. Piezo1 distribution is relatively homogeneous in both conditions, suggesting that the neuroepithelia, independent of the presence of RGC axons have a*

***uniform Piezo1 distribution. Scale bar is 100  $\mu\text{m}$ . (b,c) Piezo1 is present in in vitro cultures of RGC axons (b) Immunocytochemistry of F-actin, piezo1, and  $\beta$ -tubulin on glass. Scale bar is 10  $\mu\text{m}$ . This data was produced by me and published in (Koser et al., 2016) (c) Immunocytochemistry of Piezo1 (white) and  $\beta$ -tubulin (red) on soft (0.1 kPa) and stiff (1.0 kPa) substrates. Scale bar is 10  $\mu\text{m}$ .***

The presence of Piezo1 in the optic tract and at the neuroepithelia suggested that this MSC is required for mechanosensing in growing axons as well as in the surrounding environment.

To address concerns relating to antibody specificity (while the antibodies had over 70% sequence similarity to *Xenopus* Piezo1, they were not verified for immunohistochemistry in *Xenopus*), I conducted all experiments with negative controls (i.e. no primary antibody), to ensure that detected signals were not the result of random secondary antibody binding, or from the specimen itself. Negative controls had no signal, suggesting that signals detected in the samples were from primary antibody binding. Furthermore, I incubated specimens with pre-absorbed antibodies, with a suitable peptide to the antibody present (Piezo1 (N-15) peptide, sc-164319 P against Piezo1 (N-15) antibody, sc-164319). These samples yielded no signal, suggesting that the Piezo1 antibody was indeed binding to the antigen of interest.

I then used two Piezo1 antibodies raised in different hosts (polyclonal rabbit anti-piezo1, ab82336 and polyclonal goat anti-piezo1, sc-164319) for co-localisation studies. I incubated cultures of RGC axons with both antibodies and used signal colocalization to approximate the specificity of the antibodies. The colocalization analysis was done *in vitro*, as the signal is clearer compared to observations from whole brain imaging. Overall, merged images showed a relatively high degree of colocalization (Figure 3-2). Analysis using the Fiji Coloc2 plugin showed complete correlation between the goat anti-Piezo1 and rabbit anti-Piezo1 (Manders Overlap Coefficient = 1.0) and positive correlation between the rabbit anti-piezo1 and the goat anti-piezo1 (Manders Overlap Coefficient = 0.791). The high overlap coefficients suggested that the two antibodies are binding to very similar or identical regions in the cells. The lack of complete colocalization could be attributed to the antibodies binding to different regions of the protein or competition during binding.

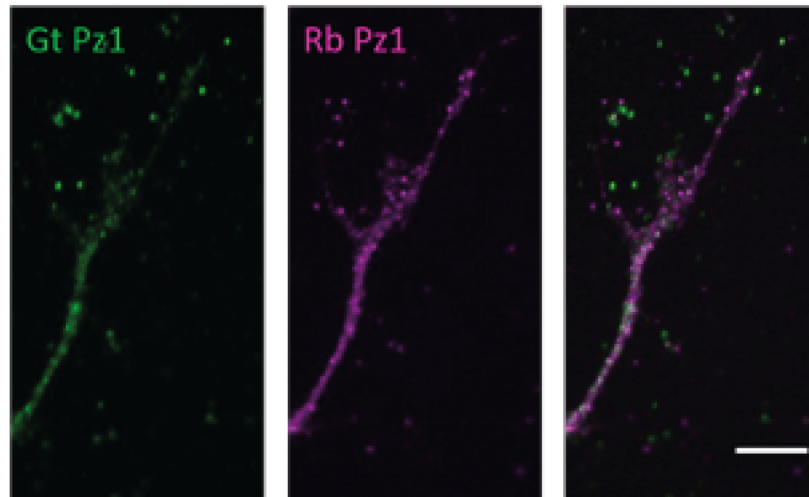


**Figure 3-2 Colocalization of Gt and Rb anti-Piezo1.**

*Merged images show a relatively high degree of colocalization. Analysis using the Fiji Coloc 2 plugin found complete correlation with Gt  $\alpha$ -Piezo1 to Rb  $\alpha$ -Piezo1 (Manders Overlap Coefficient = 1.0) and positive correlation with Rb  $\alpha$ -Piezo1 to Gt  $\alpha$ -Piezo1 (Manders Overlap Coefficient = 0.791). Scale bar is 10  $\mu$ m. Gt: goat, Rb: rabbit.*

Finally, to directly test antibody specificity, I downregulated Piezo1 expression using translation blocking morpholinos designed against *X. tropicalis* piezo1 (Pz1 MO) (since overexpression of Piezo1 was not a simple option because of its size of >2500 amino acid length).

### 3.3 Translation blocking morpholinos downregulate Piezo1 protein expression

Because eye primordia exposed to Pz1 MO did not adhere well to cell culture substrates, I could not validate Piezo1 antibodies using immunostaining because too few axons grew and most primordia detached at the latest during the washing steps of the immunostaining process. Instead, Western blot analysis on Piezo1 downregulated samples delivered useful results (Figure 3-3).

When I analysed protein lysates extracted from stage 40 heads of wild-type, control injected, and Pz1 MO injected embryos, I found (using polyclonal rabbit anti-piezo1, ab82336) that Pz1 MO downregulated Piezo1 protein levels by  $42\% \pm 9\%$  compared to controls (this data was part of my contribution to (Koser et al., 2016)).

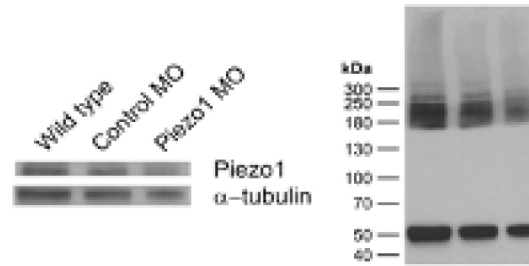


**Figure 3-3 Piezo1 morpholinos down regulate protein expression.**

*Western blot analysis of translation blocking by a Piezo1 morpholino showed a significant decrease in the expression of the protein ( $42\% \pm 9\%$ ) compared to control injected samples.  $n=4$  Western blots with duplicates of lysates. Left: cropped lanes of Piezo1 and  $\alpha$ -tubulin (loading control). Right: Full blot with molecular weight standard. This data was produced by me and published in (Koser et al., 2016)*

The antibody used in these Western blots was discontinued by Abcam and we have since found a suitable replacement antibody. Katrin Mooslehner, a colleague in the Franze group, tested several new commercially available Piezo1 antibodies in *Xenopus* and mouse tissue. She tested a range of tissue types with varying Piezo1 levels (e.g. adult *Xenopus* lung/kidney/spleen tissue and whole embryo extracts, and various mouse tissues) and verified that differences in Piezo1 levels in various tissues could be detected using polyclonal anti-rabbit piezo1, NBP1-78446. Subsequently, she independently validated Pz1 MO downregulation in *Xenopus* with this antibody (results shown in Figure 6-1). Thus, the translation blocking morpholinos used in this study indeed downregulated Piezo1 protein expression.

### 3.4 Cell autonomous and non-cell autonomous regulation of axon guidance through Piezo1 signalling

We previously found that downregulating Piezo1 in the CNS (simultaneously in the OT and surrounding neuroepithelia) resulted in aberrant axon growth and severe pathfinding errors (Koser et al., 2016). Downregulation in the entire CNS was achieved by injecting both dorsal blastomeres at the four-cell stage of the embryo.

I was interested if the role of Piezo1 in axon guidance was cell-autonomous and/or non-cell autonomous. In essence, would Piezo1 depletion in just RGC axons result in the same

axon guidance defects, or is Piezo1 also required in the surrounding environment for accurate axon pathfinding?

To downregulate Piezo1 in only the axons of the optic tract or in the neuroepithelia, I injected morpholinos in one of the two dorsal blastomeres at the four-cell stage (Figure 3-4(a)). This resulted in Piezo1 downregulation in only one half of the nervous system. As RGC axons cross over completely to the contralateral brain surface in the optic chiasm, Piezo1 is downregulated in optic tracts growing across normal neuroepithelia and, conversely, normal optic tracts grow across Piezo1 downregulated neuroepithelia on the contra-lateral side (Figure 3-4(b)). Control embryos in these experiments were injected in both dorsal blastomeres with a standard scrambled control-morpholino.

When Piezo1 was depleted in only the OT, I found that most axons still grew to the optic tectum, and pathfinding defects were less dramatic compared to when Piezo1 was downregulated in the entire central nervous system (Figure 3-4 c, d). The optic tract elongation (ratio of the major to minor axis of an ellipse fitted over the tract) was not significantly different from that of control injected embryos ( $p = 0.83$ ) (Figure 3-4(f)). However, close to 30% of the brains analysed had axons that stalled at the caudal turn, in contrast with 6.25% in controls. Furthermore, over 35% of brains had axon misprojections, e.g. deviations at the caudal turn, straying axons from the main optic tract bundle, or dorsal-anterior projections of the tract, whereas only 6.25% of controls had misprojection defects (Figure 3-4 e). These findings suggest that Piezo1 is important in the axons themselves for accurate pathfinding.

Considering that RGC axons actively grow, navigate, and respond to mechanical cues from the neuroepithelia, it was expected that downregulation of an MSC like Piezo1 in the axons resulted in pathfinding defects.

Surprisingly, however, Piezo1 downregulation in only the neuroepithelia resulted in far more dramatic axon guidance defects. Optic tract elongation was significantly lower compared with controls ( $p = 3.0E-4$ ) or when Piezo1 was downregulated solely in RGC axons ( $p = 0.01$ ) (Figure 3-4 f). Additionally, over 50% of the brains analysed had axons that stalled at the caudal turn and more than 45% of optic tracts had axonal misprojections (Figure 3-4 e). This result was highly intriguing since, despite the RGC axons having normal Piezo1 levels and being able to sense their mechanical environment, the optic tract

### Chapter 3: Piezo1 in the *Xenopus* embryonic brain

grew aberrantly, suggesting that Piezo1's presence at the neuroepithelia is essential in axon pathfinding.

Downregulating Piezo1 in both the axons and the neuroepithelia resulted in more devastating axon pathfinding defects. In line with our previous findings (Koser et al., 2016), optic tract elongation was significantly lower compared with controls ( $p = 3.3E-3$ ) (Figure 3-4 f), and also compared with Piezo1 downregulation in just the RGC axons ( $p = 0.04$ ). Only 10% of brains had a normal optic tract, while axons stalled in 50% of brains, and 60% of brains had axon misprojection defects (Figure 3-4 e).

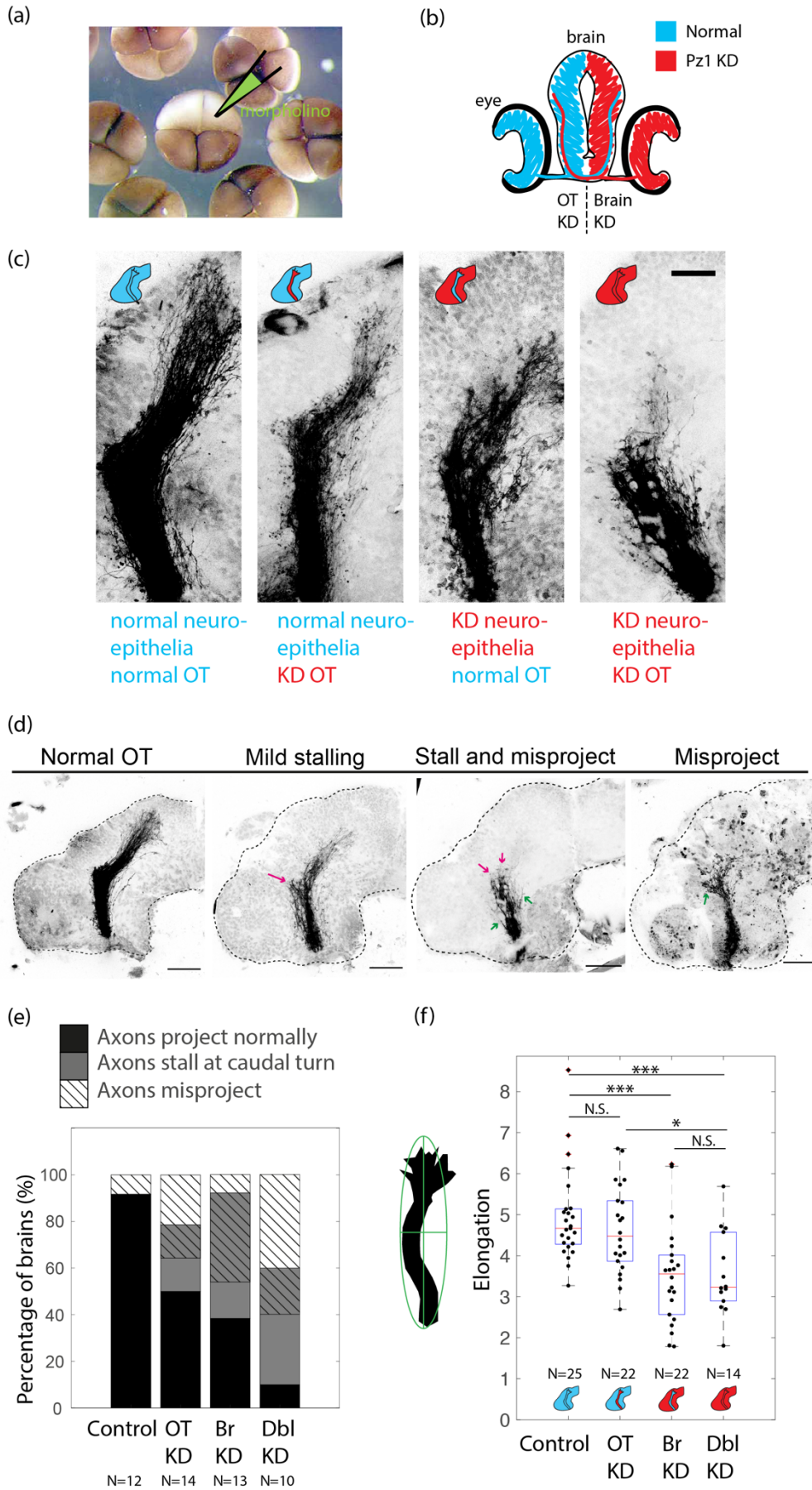


**Figure 3-4 Piezo1 is required in both the axons and the surrounding neuroepithelia for accurate axon pathfinding. (a) Morpholinos injected into one or both of the dorsal (lighter) blastomeres in the four-cell stage embryo. (b) Schematic of cross-section of *Xenopus* brain and RGC axons when morpholino is injected into one dorsal blastomeres; Piezo1 knockdown axons grow onto healthy brain tissue and vice-versa. (c) Images of OT growth in vivo. Piezo1 downregulation in either the optic tract or the neuroepithelia, but particularly the latter lead to axon guidance defects. Scale bar is 50  $\mu\text{m}$ . (d) Examples of normal and misprojection defects of OT. The dark grey dashed line indicates brain outlines, extracted from brightfield images. Axon misprojections (green arrows) and stalling defects (magenta arrows) are indicated on the images. Scale bar is 100  $\mu\text{m}$ . (e) OT phenotypes. Scoring of percentage of brains with normal OTs (black), stalling axons (grey) or misprojecting axons (diagonal hash). (f) Quantification of optic tract elongation at stage 40. Left: example ellipse fitting to the outline of an optic tract; the ratio of long and short axes determines the elongation. Right: Boxplot shows median, first, and third quartiles; whiskers show the spread of data; '+' indicates outliers. N denotes the number of animals. Data was assessed with a Kruskal-Wallis test ( $3.5\text{E-}5$ ), and with a Tukey post-hoc test. Optic tract elongation was not significantly different between control and piezo1 OT KD samples ( $p = 0.83$ ) but was significantly different between control and Br KD or Dbl KD samples ( $p = 3.0\text{E-}4$  and  $3.3\text{E-}3$ , respectively). Optic tract elongation was significantly different between OTKD and Dbl KD samples ( $p = 0.04$ ) but not between Br KD and Dbl KD samples ( $p = 0.99$ ). \* $p \leq 0.05$ , \*\* $p \leq 0.01$ , \*\*\* $p \leq 0.001$ . N denotes number of animals (data are for two biological replicates in 1(e)). Br KD: brain (neuroepithelia) knockdown, Dbl KD: double knockdown (in both the optic tract and neuroepithelia), OT KD: optic tract knockdown.**

## 3.5 Discussion

### 3.5.1 Verifying Piezo1 presence and depletion

I found that Piezo1 is present in both neuroepithelial cells and RGC axons. I was also able to downregulate Piezo1 using morpholinos and verified this through Western blots.

However, the circular assumption made for the validity of both the morpholino and the antibody in this instance must be acknowledged. Antibodies can be verified by observing

differences in signal in control versus morpholino-downregulated samples and observing differences in signal. Similarly, morpholino verification relies on checking if the protein levels are downregulated, usually via verified antibodies. As Piezo1 is a fairly recently discovered protein, few fully validated, commercially available, antibodies and reagents exist. Furthermore, while the *Xenopus* retinotectal system is well-established for studying axon guidance and very well suited for the *in vivo* mechanical characterizations done in this PhD project, not as many reagents and molecular tools are designed for this model organism compared with more conventional laboratory models such as mice and rats. Nonetheless, since we later verified Piezo1 morpholino downregulation with a different antibody against several tissue types and in different organisms (see page 67), I am suitably convinced that the morpholinos used in this study downregulate Piezo1 protein expression.

Morpholinos provide a powerful approach for inhibiting the action of a specific gene, enabling us to learn about its normal biological function. However, they are not an infallible tool. It is difficult to estimate the efficacy of morpholinos without a good antibody, as discussed above. Furthermore, it is hard to rule out the possibility that the function of genes besides the intended target are also affected. To better control for these off-target effects, it is important to ensure that the appropriate controls are applied (Eisen and Smith, 2008).

While I have ensured that all experiments are done side-by-side with a standard control morpholino experiment, it could also be useful to use a mismatched control construct, whereby 5 or more nucleotides of the designed Piezo1 morpholino are altered to affect binding (Eisen and Smith, 2008). If the mismatch and Piezo1 morpholinos both result in similar phenotypes, this would suggest that the Piezo1 morpholino could be affecting other genes as well. Furthermore, the use of a second non-overlapping morpholino that inhibited effective splicing, would complement the results of the translation blocking morpholino. Finally, the control that would provide the highest level of confidence in the specificity of the morpholino and the validity of the result would be a rescue experiment. This would be conducted for example, by introducing an RNA construct containing a version of the Piezo1 sequence which is immune to the morpholino and rescuing the phenotype observed when the morpholino is co-injected. I have designed this construct and am attempting to

generate the RNA. It has proven to be a rather challenging endeavour considering the size of Piezo1.

### 3.5.2 Piezo1 depletion in axon pathfinding defects

Piezo1 downregulation in the entire CNS resulted in severe pathfinding defects, while independently depleting Piezo1 in either RGC axons or in the neuroepithelia also resulted in optic tract defects during development. Thus, Piezo1 has both cell autonomous and non-cell autonomous roles in RGC axon pathfinding in the *Xenopus* retino-tectal system.

When Piezo1 was downregulated in only the optic tract, presumably reducing the ability of the axons to sense environmental stiffness, optic tract elongation did not change significantly. However, there were more stalling and mis-projection defects, suggesting that diminishing the ability of the axons to mechano-sense and -transduce results in pathfinding errors.

These mild *in vivo* pathfinding errors can be contrasted to the growth effects of Piezo1 KD *in vitro*. Piezo1-downregulated RGC axons (using Pz1L MO – a newly developed and improved morpholino discussed in Chapter 6), cultured *in vitro* on glass, grew significantly longer compared with controls (Foster, 2020). *In vivo* this effect may not have been observed as Piezo1 downregulation in the optic tract was not fully independent of other variables. Furthermore, we have previously shown that in wild-type embryos, softening brain tissues results in reduced optic tract elongation. Therefore, axonal morphology could also be consistent with axons sensing a potentially softened environment and responding as such (but in an attenuated fashion due to the Piezo1 depletion).

To better isolate the effects of downregulating Piezo1 in only the RGC axons, Piezo1 downregulated eye primordia could be grafted into wild-type embryos to observe OT elongation and pathfinding. For the most part, Piezo1-downregulated axons were still able to make their way to the tectum, suggesting some redundancies in chemical and mechanical signalling. Moreover, it is possible that other MSCs that are important in *Xenopus* axon guidance during development, such as TRPC1 (Kerstein et al., 2013; Shim et al., 2005; Wang and Poo, 2005), may be present and compensating for the Piezo1 depletion in the neurons. For example, when TRPC1 was depleted in *Xenopus* spinal neurons, this did not result in significant alterations of neurite outgrowths compared with

controls, and the authors proposed that other MSCs may have compensate for this (Kerstein et al., 2013).

### 3.5.2.1 Piezo1 downregulation in the neuroepithelia

The neuroepithelium is responsible for producing and organising the chemical and mechanical signals that direct axons to their target. RGC axons navigate to the optic tectum in a highly stereotyped and directed manner; the axons encounter and respond to long- and short-range chemical and mechanical guidance cues that direct them to their end target (Chedotal and Richards, 2010; Koser et al., 2016; Tessier-Lavigne and Goodman, 1996; van Horck et al., 2004). Piezo1 downregulation in the neuroepithelia had more severe pathfinding defects, suggesting that non-cell autonomous processes in axon guidance were also mechanosensitive.

In light of the observations that Piezo1 downregulation in the neuroepithelia resulted in more severe pathfinding defects, I chose to focus on this rich environment that leads the axons to their final destination in the rest of my thesis.

Piezo1 is thought to respond purely to mechanical cues. Hence, both RGC axons and neuroepithelial cells that instruct RGC axon growth likely respond to mechanical signals. As Piezo1 downregulation may result in changes in either cellular mechanosensing, mechanical cues themselves (e.g., tissue stiffness), or both, I first characterised the dependence of mechanical brain tissue properties on Piezo1 expression *in vivo*, as described in the following chapter.

## Acknowledgments

Eye primordia in Figure 3-1 (c) were cultured by Sarah Foster.

# 4 CHARACTERIZATION OF PIEZO1-DOWNREGULATED BRAIN TISSUE

In the previous chapter, I found that Piezo1 downregulation in either RGC axons or the surrounding neuroepithelial cells resulted in axon guidance defects. This demonstrates that axons require Piezo1 to sense mechanical cues from the environment but also that Piezo1 is required in the environment for axons to pathfind accurately.

As discussed in the introduction to *Xenopus* axon pathfinding (in section 1.5), the neuroepithelia across which RGC axons grow is a rich and diverse landscape of chemical guidance molecules and mechanical cues. Since healthy RGC axons that grew across Piezo1 downregulated neuroepithelia had navigational issues, this suggested that Piezo1 perturbation of the neuroepithelia could be affecting mechanical or chemical signals (for example guidance cues) found in the environment. In this section, I explored if Piezo1 downregulation affects tissue mechanics or the expression of Sema3A (a key chemical guidance cue involved in mid-OT turning).

## 4.1 Brain tissue stiffness decreases with Piezo1 downregulation

To investigate the *in vivo* mechanical landscape of the developing *Xenopus* brain, I used an AFM-based approach developed and optimized by previous members of the Franze group for *Xenopus* embryonic brain measurements (Koser et al., 2016; Thompson, Pillai et al., 2019) to generate tissue stiffness maps of stage 40 embryonic brains.

Briefly, an AFM cantilever with a spherical bead attached, was used to indent the brain tissue with a set force and the cantilever deflection measured. The recorded cantilever deflection can be used to measure the force exerted by it upon contact, and a force-distance curve can be generated for each indentation of the sample, from which the apparent elastic modulus  $K$  can be calculated, which is a measure of the tissue's local stiffness. Indentation measurements were performed in a rectangular grid on the exposed brain surface, with a

spatial resolution of 20-25  $\mu\text{m}$  (a scale relevant to individual RGC growth cones (Holt, 1989)). Stiffness values obtained were visualized as colourmaps, with individual 'pixels' of the map corresponding to single AFM indentation measurements (Figure 4-1 a-c).

I conducted stiffness measurements on stage-matched sibling embryos injected with a standard control morpholino (Scr MO) and in embryos where Piezo1 was downregulated solely in the optic tract (OT KD), in only the neuroepithelia (Br KD), or in both the OT and neuroepithelia (Dbl KD) (Figure 4-1 d,e).

Piezo1 downregulation in only the OT did not result in a significant difference in brain tissue stiffness compared with control injected embryos ( $p = 0.15$ ) (Figure 4-1 e). This suggested that OT defects discussed in the previous section were likely due to the axons' reduced ability to sense proper mechanical cues from the environment, illustrating once more the importance axon mechanosensing in pathfinding.

Piezo1 downregulation in the neuroepithelia, however, resulted in significantly softer brains, compared with control injected embryos ( $p = 3.8\text{E-}9$ ) (Figure 4-1 e). The OT defects (e.g. reduced elongation and axonal misprojections) observed in the previous section (Figure 3-4) could thus be attributed to the response of healthy axons to a too soft environment. This hypothesis is supported by previous *in vitro* work, whereby wild-type RGC axons cultured on stiff substrates grew straighter and longer, while those on soft substrates were shorter and had a higher tendency to splay apart rather than to bundle (Koser et al., 2016). Moreover, in the same publication, *in vivo* experiments in which chondroitin sulfate proteoglycans were applied to soften brain tissue showed similarly decreased OT elongation and more pathfinding defects.

Also Piezo1 downregulation in the whole CNS resulted in brains whose stiffness was significantly lower than that of controls ( $p = 3.8\text{E-}9$ ) and of brains with Piezo1 downregulation in only the neuroepithelia ( $p = 4.9\text{E-}5$ ) (Figure 4-1 e). The mean stiffness of Piezo1-downregulated brains was approximately half that of controls.

In conclusion, Piezo1 downregulation, particularly in the neuroepithelia, resulted in significantly decreased tissue stiffness, suggesting that mechanical signals are changed with Piezo1 depletion. This alteration of the mechanical environment could be a key reason for the OT guidance defects observed (Figure 3-4).

## Chapter 4: Characterization of Piezo1-downregulated brain tissue

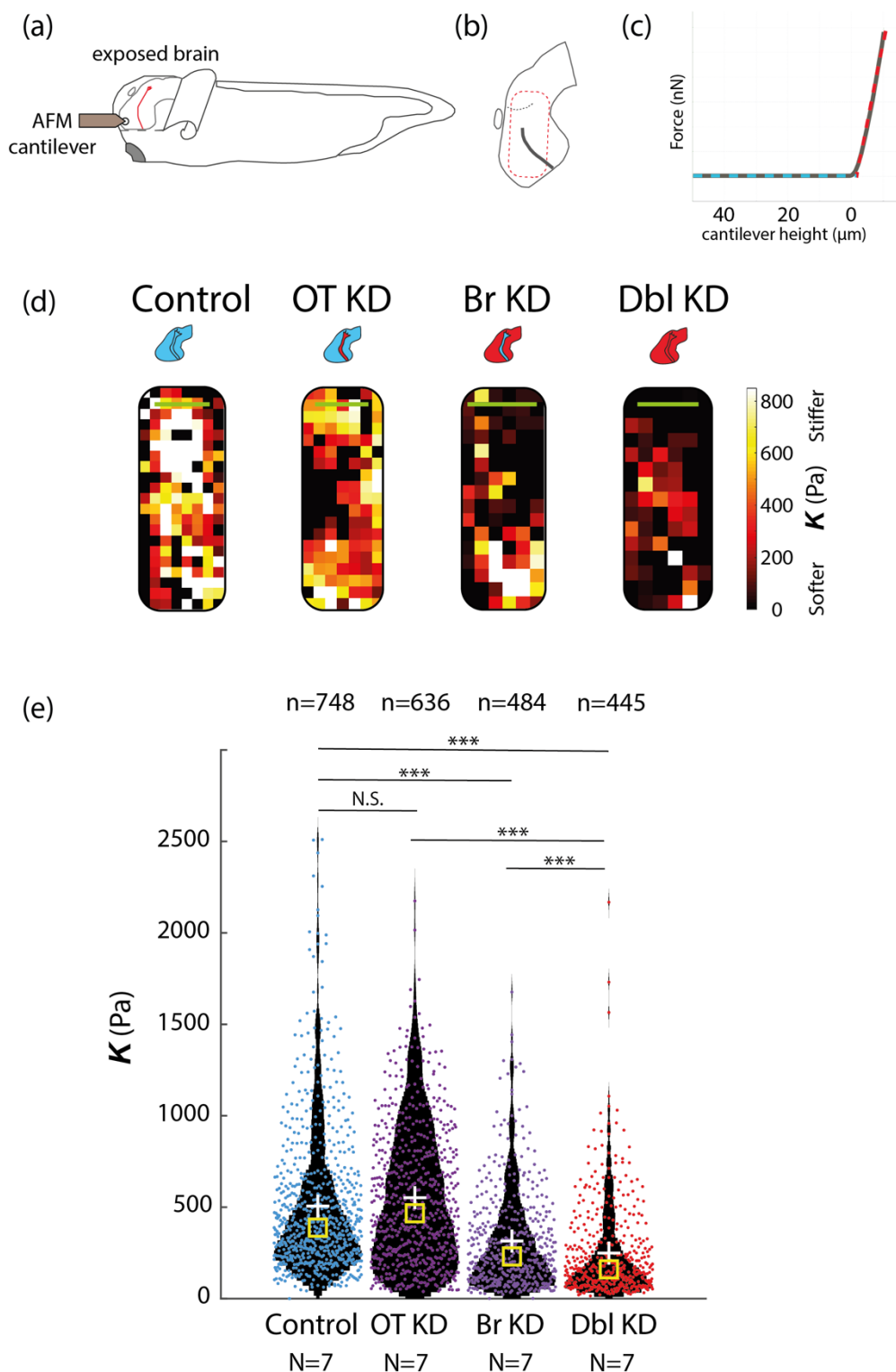


**Figure 4-1 Piezo1 downregulation results in decreased tissue stiffness.**

*(a) Schematic of the experimental setup. (b) Schematic of Xenopus brain and stiffness map orientation, the dashed red box indicates the mapped area. (c) Example of a single AFM force displacement measurement. A force-displacement curve (grey) is obtained.*

*An automated Matlab script is used to identify the contact point of the cantilever with the sample, defined at 0  $\mu\text{m}$  cantilever height, and produces a baseline (cyan dashed) and force-indentation fit (red dashed). The fit is done to a set cantilever depth into the sample. The slope of the fit is taken as the measure of sample stiffness. (d) Sample AFM stiffness maps for various *piezo1* tissue downregulation at stage 40. Colour encodes the apparent elastic modulus,  $K$ , assessed at an indentation force of 10nN. Darker colour on the map indicate softer tissue while brighter colours indicate stiffer tissue. Scale bars are 100  $\mu\text{m}$ . (e) Violin plot with scatter of individual stiffness measurements for each condition. The means and medians are indicated as white crosses and yellow squares respectively.  $N$  denotes the number of brains, while  $n$  denotes the number of measurements. Data was assessed with a Kruskal-Wallis test ( $3.8E-81$ ) and with a Tukey post-hoc test. Control brains stiffness values were not significantly different from OT KD ( $p = 0.15$ ) but BrKD and DblKD samples were significantly softer than controls ( $p = 3.8E-9$  and  $p = 3.8E-9$ , respectively). Brain tissue stiffness was also significantly different between OT KD and Br KD with Dbl KD samples ( $p = 3.8E-9$ ,  $p = 4.9E-5$ , respectively). \* $p \leq 0.05$ , \*\* $p \leq 0.01$ , \*\*\* $p \leq 0.001$ . N.S.: not significant. Br KD: brain (neuroepithelia) knockdown, Dbl KD: double knockdown (in both the optic tract and neuroepithelia), OT KD: optic tract knockdown, *Pz1* KD: *Piezo1* knockdown (or downregulation).*

## 4.2 Semaphorin3A mRNA expression decreases with Piezo1 downregulation in the CNS

Because downregulation of the MSC Piezo1 in neuroepithelia led to severe pathfinding defects of healthy RGC axons (Figure 3-4), I was not only interested in Piezo1-related changes in tissue mechanics but also in potential changes in chemical guidance cues, and especially the signalling molecules regulating the caudal turn of the OT in the mid-diencephalon (Campbell et al., 2001). Therefore, I studied the expression of Sema3A in Piezo1-downregulated brain tissue. *In situ* hybridization of stage 40 whole brains with a DIG-labelled *Xenopus sema3A* antisense RNA probe allowed for the visualization of *in vivo* *sema3A* mRNA expression. In control injected embryos, *sema3A* patterning was identical to what was published in the literature for wild-type embryos (Atkinson-Leadbeater et al., 2010; Campbell et al., 2001); *sema3A* mRNA is highly expressed in the telencephalic region. In contrast, in Piezo1-downregulated embryos, Sema3A RNA expression in the telencephalon was significantly attenuated (Figure 4-2 a).

In both control injected (Scr MO) and Piezo1 knockdown (Pz1 MO) embryos, the mean signal intensity in the telencephalon (ROI) was significantly higher than in the hypothalamus ( $p_{\text{Scr}} = 1.2\text{E-}4$ ;  $p_{\text{Pz1}} = 0.004$ ) (Figure 4-2 b). The hypothalamus served as control region of the brain as it abuts the telencephalon and does not normally express *sema3A* RNA. While the trend was of higher signal in the control over the Piezo1 downregulated brains, the ratio of signal intensity (2.5.4.1) in the telencephalon did not reach the threshold of significance (Figure 4-2 c) in spite of the visible difference in the two conditions by eye. This may be partly due to *in situ* hybridizations being not a truly quantitative method and saturation of the signal in the Scr MO condition.

I then verified these results using qPCR by comparing *Sema3A* mRNA expression in the telencephalon with the expression of four different reference genes. While not all reference genes showed a significant difference, there was a trend towards decreased *sema3A* RNA expression in Piezo1 downregulated brains compared with control in all reference genes (Figure 4-2 d).

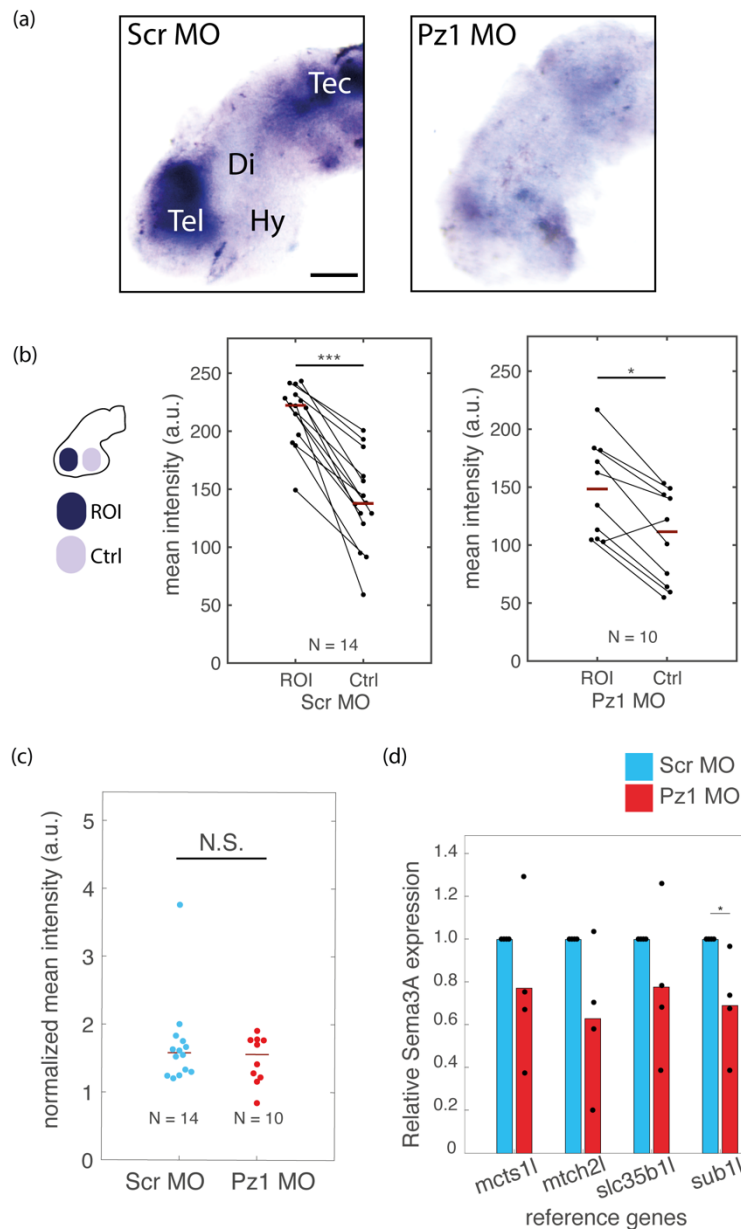


**Figure 4-2** *Sema3A* mRNA expression in the brain is altered when Piezo1 is downregulated in the CNS.

*(a)* In situ hybridization showing *Sema3A* RNA expression in control and Piezo1 knockdown brains. Scale bar is 100  $\mu$ m. *(b)* The telencephalon, region of interest (ROI) has significantly higher mean signal intensity than a control non-*Sema3A* producing region of the brain (Ctrl) adjacent to it, both in the control morpholino (Scr MO,  $p = 1.2E-4$ ) and Piezo1 morpholino (Pz1 MO,  $p = 0.004$ ) injected embryos. Data was assessed with a Wilcoxon signed-rank test. Ladder plots show the paired values for individual brains, means are indicated by red lines. *(c)* Plot of normalized mean intensity

*of sema3A signal in Scr MO vs Pz1 MO brains, data was assessed with a Wilcoxon rank-sum test. Each normalized mean intensity value plotted is the background corrected mean intensity for each brain,  $ROI \text{ mean intensity}/Ctrl \text{ mean intensity}$ . Population means are indicated by the red line.  $N$  denotes the number of brains assessed. (d) qPCR analysis of relative *sema3A* mRNA expression levels of the ROI in Scr MO and Pz1 MO compared with various reference genes. The bars indicate the mean of four biological replicates, the data for individual replicates are scattered over the bar. For each reference gene, the Pz1 MO injected embryos *sema3A* expression levels were normalized to Scr MO injected embryos *sema3A* levels.  $p_{mctsl1} = 0.31$ ,  $p_{mtch2l} = 0.31$ ,  $p_{slc35b1l} = 0.31$ ,  $p_{sub1l} = 0.028$ ).  $*p \leq 0.05$ ,  $**p \leq 0.01$ ,  $***p \leq 0.001$ ; a.u.: arbitrary units, Ctrl: control brain region, Di: diencephalon, Hy: hypothalamus, Pz1 MO: piezo1 morpholino knockdown, ROI: region of interest in the brain, Scr MO: scrambled control morpholino, Tec: optic tectum, Tel: telencephalon.*

Besides the telencephalon region, *sema3A* signal intensity in the posterior tectum was also attenuated in Piezo1 knockdown embryos. To determine if *sema3A* attenuation occurred only in the brain or in the rest of the CNS as well, *in situ* hybridizations were repeated on whole stage 40 embryos (Figure 4-3 a). Piezo1 downregulation in the CNS resulted in a global decrease of *sema3A* mRNA expression in knockdown tissue, as the signal intensity across the spinal cord was significantly attenuated in Piezo1 downregulated embryos if compared to controls ( $p = 3.4E-4$ ) (Figure 4-3 b-d).

There were clear morphological differences between control and Piezo1 knockdown embryos, unlike in whole brains where the two conditions were not easily distinguishable based on morphology alone. For instance, Piezo1 knockdown embryos tended to be smaller and lordotic. Therefore, to blind the experimenter to the embryo condition during analysis and to comparably analyse the signal observed, A semi-automated approach was developed to analyse the data (2.5.4.2). This analysis also showed that *sema3A* mRNA expression was attenuated in Piezo1 downregulated tissue across the embryos CNS.

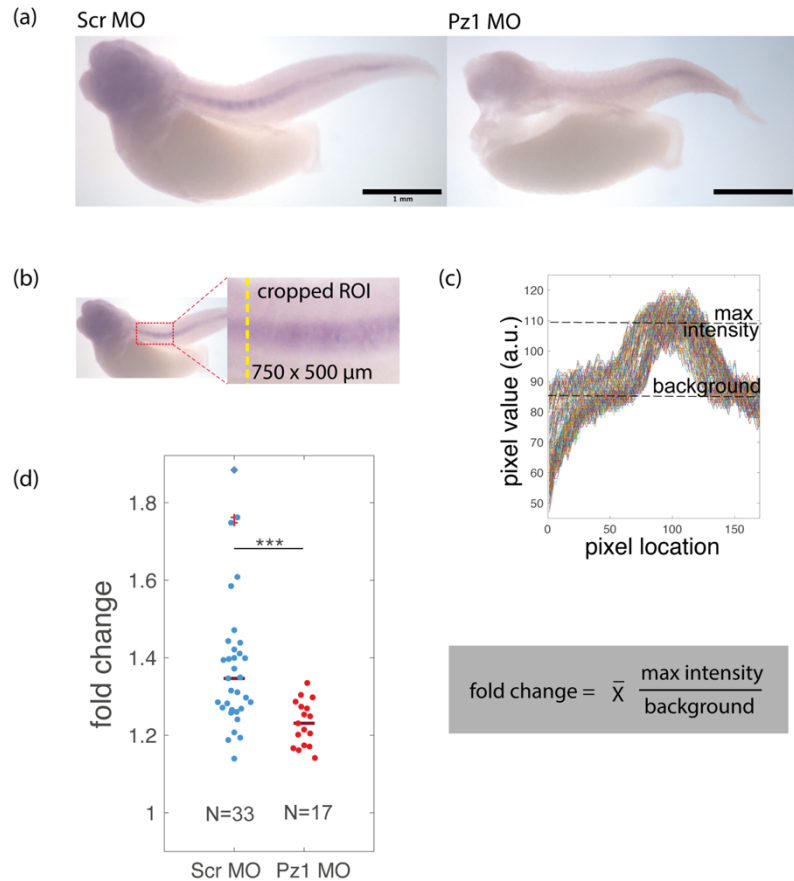


**Figure 4-3 Sema3A mRNA expression in the whole embryo at stage 40.**

*(a) In situ hybridization showing sema3A RNA expression in control injected (Scr MO) and Piezo1 downregulated (Pz1 MO) embryos. Scale bar is 1mm. (b) An example of region of interest (ROI) selection along the spinal cord. The yellow dashed line indicates a sample perpendicular line. Perpendicular line profiles were made sequentially across the ROI. (c) An example plot of all the line profiles, each coloured trace indicates an individual line profile. The mean value of the top percentile and the median of all the line profiles were taken as the maximum intensity and the background respectively. (d) Plot of fold change of Scr MO and Pz1 MO shows a significant difference between the two ( $p = 3.4E-4$ ), data was assessed with a Wilcoxon rank-sum test.  $N$  denotes the number of embryos assessed. Means are indicated by red lines, '+' indicates outliers. \* $p \leq 0.05$ , \*\* $p \leq 0.01$ , \*\*\* $p \leq 0.001$ . N.S.: not significant; Pz1 MO: piezo1 morpholino knockdown, ROI: region of interest, Scr MO: scrambled control morpholino,  $\bar{X}$ : mean. Data are from one biological replicate.*

## 4.3 Discussion

### 4.3.1 Piezo1 downregulation and alterations in tissue mechanics

Tissue stiffness in this thesis is measured using AFM. AFM is excellent at measuring topographical features and information from the surface but not deeper in the tissue. Furthermore, AFM measurements are obtained in one direction ( $z$ ), while forces act in all 3-directions ( $x,y,z$ ). Ideally, tissue is measured in multiple planes to account for this. However, it is technically challenging to make these measurements in an intact live embryo. Since the *Xenopus* brain, when laterally mounted, is almost a flat surface and the axons grow very close to the top surface of this plane, the AFM maps gives us a reasonable estimation of the stiffness landscape that the RGC axons are encountering as they grow. Another limitation is that AFM mapping does not provide information about other mechanical properties of materials e.g. how tissue is stretched/ if it is under torsion etc, or about other mechanical properties of the material, especially since the measurements are made in a single plane. However, as apparent tissue stiffness is the main mechanical characteristic of interest in this project, AFM was chosen as the most useful tool for this investigation.

Piezo1 downregulation generally resulted in a decrease in tissue stiffness overall. In the case of Piezo1 downregulation in only the OT (but not in the brain tissue), it is possible that, while I found no significant difference in brain stiffness maps, the axons themselves may have altered mechanical properties. However, it is not possible to resolve axonal mechanics from *in vivo* measurements, since both the OT and the underlying and neighbouring neuroepithelial cells contribute to the mechanical measurements. *In vitro* AFM measurements of the RGC axons from explanted eye primordia are possible, but as discussed in section 3.3, Piezo1-downregulated eye primordia often do not adhere or grow well in cultures. Even if culturing Piezo1 downregulated eye primordia were possible, substrate effects may confound stiffness measurements *in vitro* since the axons are less bundled to each other compared to *in vivo* where they grow as a -mostly- coherent tract. As RGC axons are very thin (~a few hundred nanometers), AFM indentation measurements would mostly reflect the stiffness of the underlying glass rather than of the axons. Axons cultured on compliant substrates of physiological stiffness, fabricated with a sufficient thickness to preclude substrate effects, may still not produce good estimations of differences in stiffness, as force applied by AFM indentation would deform not only

the axons but also the underlying substrate, resulting in under-estimations of the stiffness values (Rheinlaender et al., 2019).

It was intriguing to find that stiffness maps of whole CNS downregulated brains were significantly softer than when Piezo1 was downregulated in only the neuroepithelial tissue. One possible reason is that the AFM indentation also detects the softer tissue on the opposite side of the brain, in the Dbl KD condition. The lower brain tissue stiffness combined with the axons' decreased ability to sense the mechanical environment quite likely explains the more devastating pathfinding defects seen when Piezo1 is downregulated in the entire CNS.

Overall, my results are congruous with findings in *in vivo* AFM measurements of *Drosophila* brains, whereby gliomas with elevated dPiezo levels had higher tissue stiffness compared to normal brains -in which healthy glia do not express dPiezo (Chen et al., 2018). Similar to my results, Chen et al. found that genetic deletion of dPiezo in the glioma models resulted in decreased tissue stiffness.

#### 4.3.2 Piezo1 downregulations affects *sema3A* mRNA expression

Besides Piezo1 downregulation resulting in decreased tissue stiffness, there was also reduced *sema3A* mRNA expression. *In situ* hybridizations are an excellent method for visualizing location of RNA, however, it is not a quantitative method. Thus, while I found less *sema3A* signal in the brain, a method that can quantify this change more robustly would strengthen this finding. Hybridization chain reaction is a more quantitative method, which can show the signal *in situ*, and will be explored in future experiments. Nonetheless, these results suggest an interplay between mechanical and chemical signalling in axon guidance. It would be exciting to investigate if other chemical guidance cues are affected by Piezo1 downregulation as well, or if this is a Sema3A-specific phenomenon. It would be valuable to investigate, Slit1, in light of its important role in mid-OT turning (Atkinson-Leadbeater et al., 2010) in brains with downregulated Piezo1 expression or altered stiffness, and Eph-ephrin signalling which play a critical role in retino-tectal mapping (Hornberger et al., 1999; Mann et al., 2002). From visual inspection, I would postulate that Netrin-1 guidance at the optic nerve head, and inhibitory Slit and sonic hedgehog signalling at the optic chiasm are unaffected, since RGC axons in Piezo1 knockdown brains only show major guidance defects post-crossing, after they have reached the contralateral brain hemisphere. However, earlier stages of development, and early RGC

axon sprouting in the retina of Piezo1 downregulated embryos should be investigated before this conclusion is drawn.

In the next chapter I take a step back and examine cell body density, an important component of tissue mechanics, to investigate if it scales with brain tissue stiffness *in vivo*, and if this in turn could account for the change in Piezo1 downregulated brain mechanics.

## Acknowledgments

AFM mapping and data analysis in Figure 4-1 were done in collaboration with Amelia J. Thompson.

RNA extraction and qPCR in Figure 4-2 (d) were done with assistance from Katrin Mooslehner and Ross McGinn.

In situ hybridizations of whole *Xenopus* embryos in Figure 4-3 were done by David Mafullul, for a summer studentship under my supervision.

MATLAB script for analysis automation in Figure 4-3 was provided by Maximilian Jakobs.



# 5 CELL BODY DENSITY CONTRIBUTES TO TISSUE MECHANICS

During development, multiple embryonic tissues, including the brain, increase in stiffness over short time scales (i.e., over a few developmental stages). For example, during quail embryonic heart development, *ex vivo* AFM measurements of the myocardium showed an increase in stiffness from 4 to 10 days of development (Engler et al., 2008). Similarly, micropipette aspiration measurements of chick embryo hearts showed that the tissue stiffened at a rate of  $\sim 0.3$  kPa/day (Majkut et al., 2013).

Although the brain is one of the softest tissues in the body overall, it actually stiffens during certain periods of early development. For instance, *ex vivo* AFM measurements of the mouse embryonic cerebral cortex showed that tissue stiffness gradually increased between stages E12.5 to E16.5 (Iwashita et al., 2014). In *Xenopus* embryos, using *in vivo* AFM, we also found that brain tissue stiffens over time (Koser et al., 2016). Specifically, we found that a gradient in brain tissue stiffness developed during the outgrowth of the RGC axons that eventually form the optic tract. This gradient lay perpendicular to the growth direction of the RGCs and their axons followed reliably en route to their target, the optic tectum. We also found that brain tissue stiffness scaled with cell body density.

We then developed a method combining time-lapse *in vivo* AFM with upright fluorescence imaging to more closely study the establishment of this stiffness gradient, while visualizing the RGC axons as they grew across the surface of the brain (Thompson, Pillai et al., 2019). In this study, we found that the local increase in tissue stiffness preceded axon turning, and also confirmed that local tissue stiffening correlated with cell proliferation.

In this chapter I discuss in more detail some of my contributions to the two publications from our group discussed above, namely the study of the role of cell body density in regulating tissue stiffness.

## 5.1 Brain tissue stiffness correlates with cell density

AFM measurements of *Xenopus* brain tissue at stage 40 (done by David Koser and Amelia J. Thompson) showed a stiffness gradient perpendicular to the optic tract. Brain tissue on the rostral side of the tract was stiffer than on the caudal side of the tract (Figure 5-1a). Optic tract ablation did not result in a change of the measured stiffness, suggesting that the patterning was an inherent property of the brain tissue, rather than induced by the presence of the growing axons (Koser et al., 2016).

In the mouse spinal cord, a different CNS tissue, stiffness scales with cell body density (Koser et al., 2015). To determine if this was also the case in the developing *Xenopus* embryonic brain, I fluorescently labelled the nuclei and imaged whole mount brains with confocal microscopy. The optic tract was labelled anterogradely at the retina with horseradish peroxidase (HRP). The area occupied by cell bodies in a given  $50 \times 50 \mu\text{m}$  region (on the rostral and the caudal side of the landmark bend in the OT area where axons turned) was determined (Figure 5-1 b). I looked at the bend region, as stiffness gradients were a potential axon guidance cue, encouraging the turning behaviour of the tract. Cell body densities rostral to the optic tract, where the tissue is stiffer, were significantly higher than caudal to it ( $p = 0.0039$ ), suggesting that brain tissue stiffness scales with local cell body density also in *Xenopus* (Figure 5-1 c).

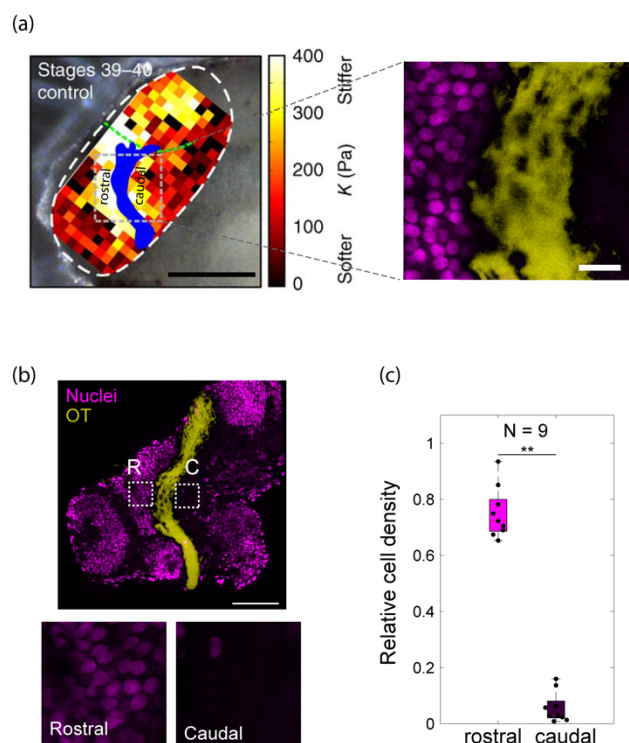


**Figure 5-1 Increased cell body density correlates with tissue stiffness.**

*(a) Left: Image of a Xenopus embryo brain with overlaid AFM-based stiffness maps of the exposed brain tissue. Colour encodes the apparent elastic modulus  $K$  assessed at an indentation force of  $7nN$ . The blue shape shows the OT location (identified with from fluorescent images). The green line indicates the tectum boundary. The grey dashed region indicates the region shown in the image to the right. Scale bar is  $200\ \mu m$ . Data from David Koser and published in (Koser et al., 2016) Right: Immunohistochemistry demonstrating nuclei (magenta) density rostral to the OT (yellow). Scale bar is  $20\ \mu m$ .*

*(b) Representative confocal image of whole mount brain. Nuclei were labelled with DAPI (magenta) and the OT was visualized using HRP (yellow). A  $50 \times 50\ \mu m$  region was selected on the rostral and caudal side of the OT. Scale bar is  $100\ \mu m$ . Below: enlargement of regions in dashed lines.*

*(c) Quantification of nuclei density on both sides of the OT; cell density is significantly higher rostral to the OT ( $p = 0.0039$ ). Data was assessed with a Wilcoxon signed-rank test.  $N$  denotes the number of brains assessed. Boxes show the 25th, 50th (median), and 75th percentiles; whiskers show the spread of the data. C: caudal, OT: optic tract, R: rostral.*

## 5.2 Tissue stiffness changes *in vivo* correlate with local cell body densities in the developing brain

As previously stated, the stiffer region rostral to the optic tract was observed at a later stage of development, i.e. stage 39-40. Earlier in development, at stage 33/34, there is no stiffness gradient perpendicular to the growing axons (Koser et al., 2016). This suggested that if cell body density did indeed affect brain tissue stiffness in the developing *Xenopus* brain, there were three possible explanations for our observations at the earlier developmental stage: (i) cell bodies were more homogeneously distributed earlier than at stage 39-40; (ii) the local density of cell bodies was lower overall at earlier stages; or (iii) cell bodies were similarly distributed as at later stages but were intrinsically softer earlier in development.

To study the evolution of this stiffness gradient and its relationship to cell body density, Amelia J. Thompson conducted time-lapse AFM stiffness mapping measurements of the brain starting at stage 33/34 up to stage 37/38, while simultaneously visualizing fluorescently labelled RGC axons. She found that the onset of the stiffness gradient in the brain preceded axon turning in the mid OT (Thompson, Pillai et al., 2019), suggesting that tissue stiffness could be instructive to axon guidance in this context. I then assayed cell densities at three different developmental stages (stages 33/34, 35/36 and 37/38), using DAPI labelling of the nuclei in whole-mounted brains with fluorescently labelled optic tracts (Figure 5-2 a).

At stage 33/34, before a stiffness gradient was present, cell densities were similar on both sides of the optic tract. At later stages, however, cell densities increased significantly in the region rostral to the optic tract (where the tissue was stiffer) than caudal to it, indicating that tissue stiffness correlated with cell density (Figure 5-2 b). Moreover, these results were in agreement with previous works published on the correlation between cell densities and tissue stiffness, ranging from ruminant retinae (Weber et al., 2017) to *Xenopus* mesoderm (Barriga et al., 2018).

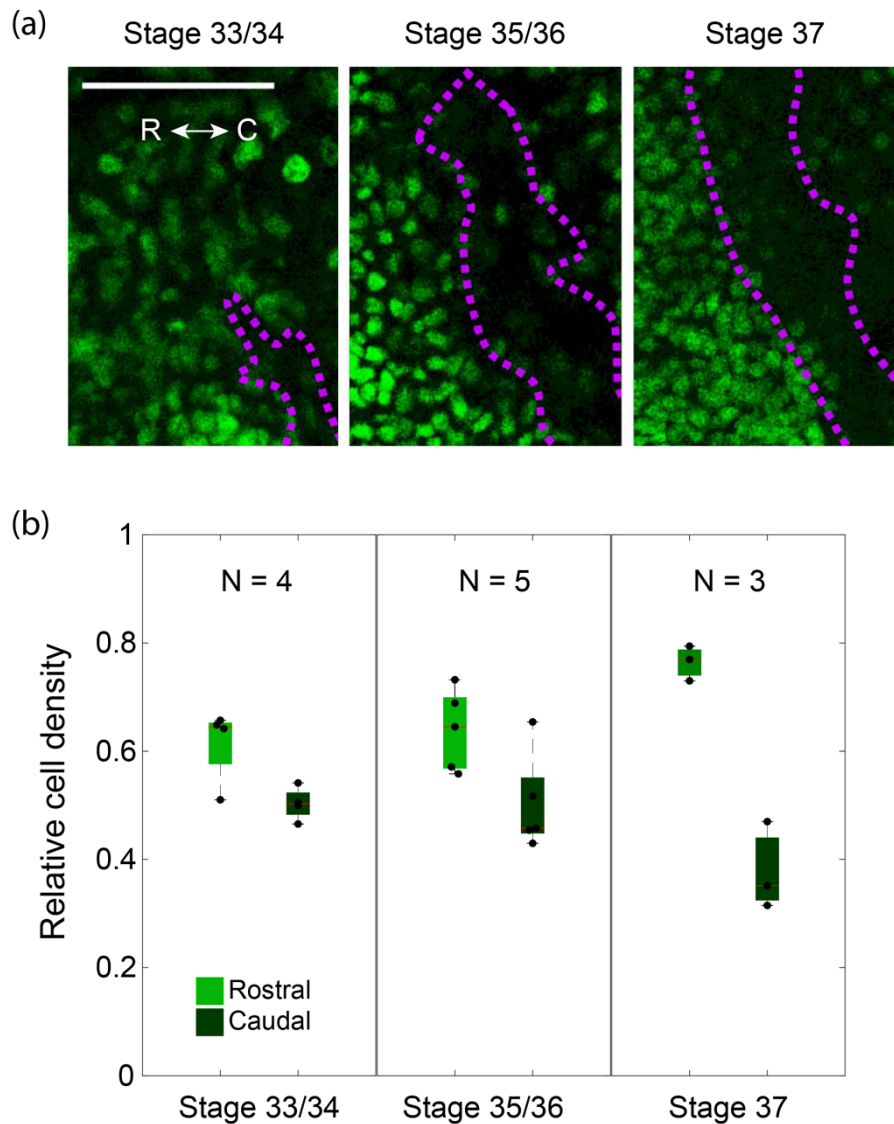


**Figure 5-2** Relative cell body density increases in the region rostral to the optic tract, as the embryonic brain develops.

*(a) Immunohistochemistry of nuclei (green) from lateral whole-mount Xenopus embryo brains at successive developmental stages. OT axons are outlined in magenta. Scale bar is 100  $\mu\text{m}$ . (b) Local cell body densities are relatively similar on either side of the OT at stage 33/34 but by stage 37, cell body densities are higher on the rostral side, compared with the caudal side. Relative cell density is the ratio of the area occupied by nuclei to the total measured area. N indicates number of brains. Boxes show the 25th, 50th (median), and 75th percentiles; whiskers show the spread of the data. C: caudal, R: rostral. Image adapted from (Thompson, Pillai et al., 2019).*

### 5.3 Blocking mitosis *in vivo* results in reduced local cell body density, diminished stiffness gradients, and decreased optic tract elongation

As cell density correlated with tissue stiffness, we hypothesized that perturbing cell proliferation (and therefore altering cell density), would prevent the observed increase in tissue stiffness. Nuclei staining and time-lapse AFM measurements were therefore repeated on *Xenopus* embryos treated with BI2536, a Polo-like kinase inhibitor that arrests cells in mitosis (Lénárt et al., 2007). BI2536 was shown to successfully inhibit *in vivo* cell proliferation in the embryonic zebrafish retina (Weber et al., 2014).

The cross-sectional area of BI2536 treated *Xenopus* brains decreased significantly compared with control brains ( $p = 5.7E-5$ ), suggesting a reduction in overall cell numbers (Figure 5-3 b). Additionally, I used phosphorylated-histone3 (pH3) staining to confirm that BI2536 triggered mitotic arrest (Hans and Dimitrov, 2001) (Figure 5-3 a). Histone H3 phosphorylation at serine 10 is a marker of mitotic cells. Ser10 phosphorylation begins in G2 and decreases upon exit from mitosis. In coronal sections of BI2536-treated embryos, the number of pH3-positive cells increased significantly over time from stage 35/35 to stage 37/38 compared to control brains ( $p = 2.2E-4$ ) (Figure 5-3 c), suggesting that that the BI2536 treatment did indeed trigger mitotic arrest, resulting in a reduction of cell density.

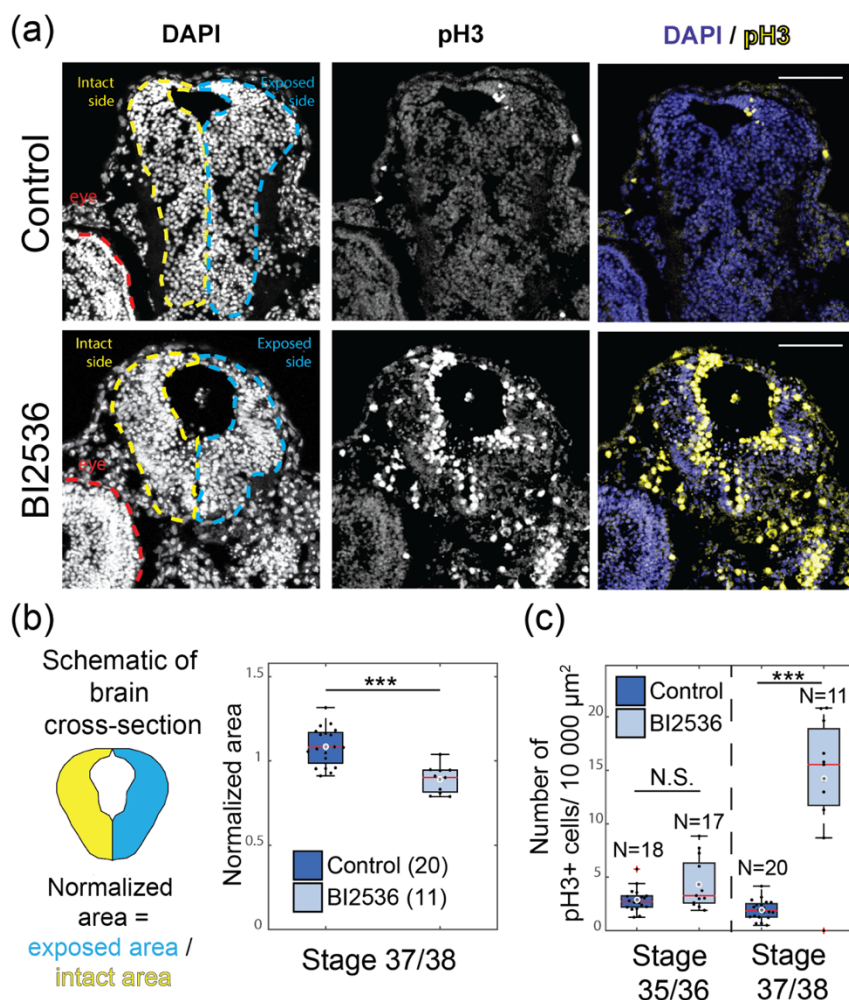


**Figure 5-3 BI2536 treatment arrests cells in mitosis and decreases brain cross-sectional area.**

*(a) Coronal sections of stage 37/38 control and BI2536-treated embryos stained for DAPI and phospho-histone3 (pH3). (b) Normalized brain area is significantly lower in BI2536-treated embryos, compared with controls ( $p = 5.7E-5$ ), indicating a decrease in total cell numbers. Number of sections for each condition are indicated in parentheses. Data was assessed with a Wilcoxon rank-sum test. (c) The number of pH3+ cells per 10 000  $\mu\text{m}^2$  brain area is initially not significantly different in the early embryo, but as development progresses to stage 37/38, it increases significantly in BI2536-treated embryos ( $p = 2.2E-4$ ), compared with controls.  $N$  denotes the number of sections. Boxes show the 25th, 50th (median), and 75th percentiles; whiskers show the spread of the data. C: caudal, R: rostral. Image adapted from (Thompson, Pillai et al., 2019).*

In addition, I found that BI2536-treatment decreased the nuclear density when compared to stage-matched healthy controls, particularly rostral to the optic tract, in lateral mount whole brains (Figure 5-4 a, b).

Time-lapse AFM measurements showed that *Xenopus* brain tissue treated with BI2536 was significantly softer than control tissue (data shown in (Thompson, Pillai et al., 2019)). Moreover, the stiffness gradient did not evolve, and concomitantly the optic tract turning angle did not increase (presented in (Thompson, Pillai et al., 2019)). BI2536-treatment also resulted in a significant decrease of optic tract elongation ( $p = 0.001$ ) (Figure 5-4 c). In conclusion, these results suggested that the gradient in cell densities contribute to the stiffness gradient that affect axon growth and turning behaviour.

To confirm that the change in stiffness was indeed due to the reduced cell density and not a side-effect specific to one particular chemical treatment, we also decreased cell density by using hydroxyurea/aphidicolin (HUA), which blocks mitosis via a different mechanism (inhibition of DNA replication). HUA-treatment similarly reduced the nuclear densities rostral to the optic tract when compared to stage-matched controls, resulting in an attenuated stiffness gradient and defects in optic tract growth (data not shown here, published in (Thompson, Pillai et al., 2019)). Both the BI2536 and HUA treatment experiments highlighted the importance of regulating local cell proliferation in mechanosensitive cellular processes *in vivo*.

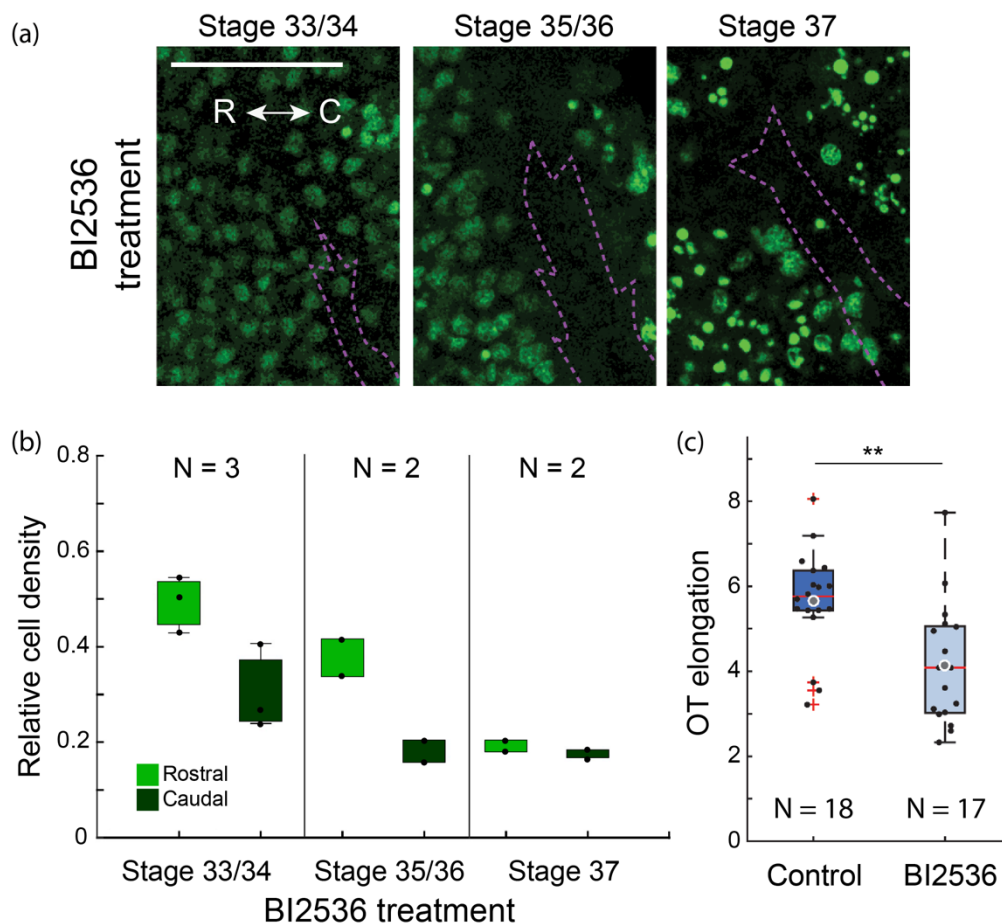


**Figure 5-4 BI2536 treatment results in a decrease of relative cell density and affects OT elongation.**

(a) *Immunohistochemistry of nuclei (green) from lateral whole-mount *Xenopus* embryo brains at successive developmental stages. OT axons are outlined in magenta. Scale bar is 100  $\mu$ m. (b) Local cell body densities are relatively similar rostral and caudal to the optic tract. (c) BI2536-treatment results in a significant decrease of optic tract elongation at stage 37/38 ( $p=0.001$ ). Data was assessed with a Wilcoxon rank-sum test.  $N$  denotes the number of brains. Boxes show the 25th, 50th (median), and 75th percentiles; whiskers show the spread of the data. C: caudal, OT: optic tract, R: rostral. Image adapted from (Thompson, Pillai et al., 2019).*

## 5.4 Decreased tissue stiffness in Piezo1 downregulated tissue is not the result of altered nuclei density

Piezo1-downregulated tissue is softer than stage matched control injected or wild-type brains (Figure 4-1). As I have shown that cell body density correlates with tissue stiffness, I investigated if the softening of tissue in Piezo1-knockdown brains was due to a corresponding decrease in cell body density.

At stage 39-40, the nuclei density was significantly higher rostral to the optic tract than caudal to it in both control injected brains ( $p = 0.017$ ) and in brains where Piezo1 was downregulated in both the OT and neuroepithelia ( $p = 0.0078$ ). When relative cell densities were compared across the rostral regions of control brains, or in brains where Piezo1 was downregulated solely in the OT, only in the neuroepithelia, or in both the OT and neuroepithelia, no significant difference was found. Similarly, relative cell densities of the caudal region for all the conditions described were not significantly different, showing that in Piezo knockdown brains cell body densities remained distributed in a similar manner across the mid-optic tract bend region, despite the overall decrease in tissue stiffness (Figure 5-5). In conclusion, my results showed that, while Piezo1 downregulation results in tissue softening, this phenomenon is not dictated by decreasing cell densities in the brain.

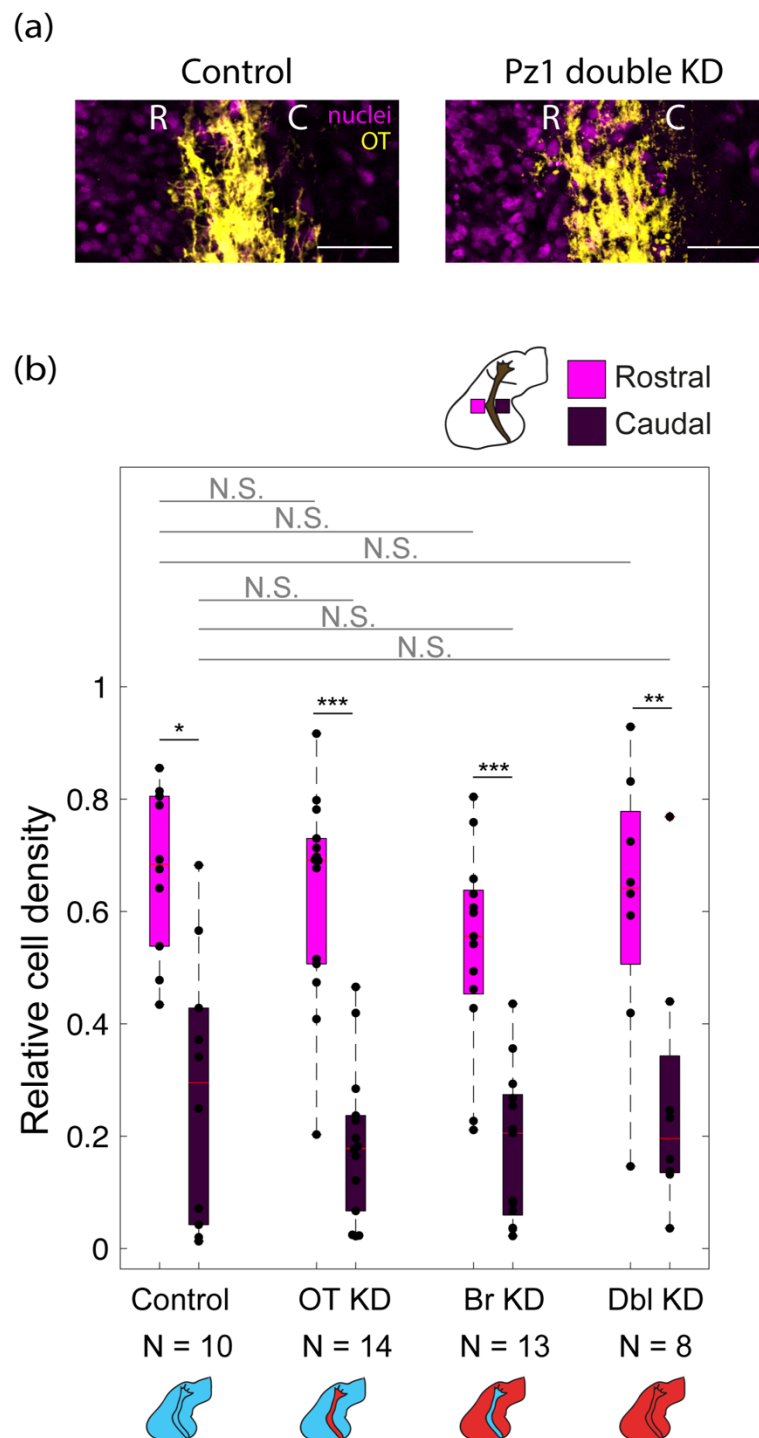


**Figure 5-5 Piezo1 downregulation does not alter local cell body densities.**

(a) Representative images of nuclei (magenta) across the rostral and caudal sides of the optic tract (yellow) bend in stage 40 *Xenopus* embryos. Nuclei were labelled with DAPI (magenta) and the OT was visualized using DiI (yellow). Scale bar is 50  $\mu\text{m}$ . (b) Relative cell densities are significantly higher in the region rostral of the optic tract, in the control ( $p = 0.017$ ), OT KD ( $p = 1.2E-4$ ), Br KD ( $p = 2.4E-4$ ) and Dbl KD ( $p = 0.0078$ ).

*Data between rostral and caudal regions of each condition were assessed with a Wilcoxon signed-rank test (black significance bars). Relative cell densities were not significantly different between the rostral regions of control, OT KD, Br KD and Dbl KD samples. Similarly, relative cell densities were not significantly different between caudal regions for all samples. Data across different samples were assessed with a Kruskal-Wallis test ( $2.9E-8$ ) and with a Tukey post-hoc test. N denotes the number of brains assessed. Boxes show the 25th, 50th (median), and 75th percentiles; whiskers show the spread of the data. Br KD: brain (neuroepithelia) knockdown, C: caudal, Dbl KD: double knockdown (in both the optic tract and neuroepithelia), OT KD: optic tract knockdown, Pz1 KD: piezo1 knockdown (or downregulation), R: rostral. Data are from two biological replicates.*

## 5.5 Discussion

### 5.5.1 Cell body density as a readout of tissue stiffness

In summary, we found that in early embryonic brain development, local tissue stiffness changes within tens of minutes, leading to heterogeneous stiffness distributions across the brain that instruct axon pathfinding. The stiffness heterogeneities correlated with changes in cell body densities across development. However, the composition of brain tissue is heterogeneous, comprising various cell types, with diverse cell adhesion molecules and a myriad ECM molecules (Lindsey et al., 2018; Ruoslahti, 1996; Sakisaka, 2005). Different combinations of these elements can result in the same stiffness value. Thus, while cell body density can be used as an estimate of tissue stiffness, other components of the tissue (e.g., the ECM and cell adhesion molecules distribution) are also likely to contribute to local tissue mechanics and should be investigated.

Live imaging of nuclei during the relevant developmental stages could potentially provide further information on the spatiotemporal dynamics of cell proliferation or cell body movement, e.g. whether or not cell bodies caudal to the tract are shifted or if there was increased proliferation rostral to the optic tract. These studies were done on laterally mounted whole brains. It would also be interesting to investigate the cross section of the brain to better understand the depth distribution of nuclei and if this too is altered. Furthermore, the perturbation of cell divisions using BI2536 may not only have altered tissue stiffness but also topological and biochemical cues that provide growth and

guidance signals to the axons. For instance, reducing the number of cell bodies rostral to the OT potentially decreases steric hindrance that would usually prevent the axons from growing into that space. Furthermore, BI2536 could induce apoptosis at the application site. While apoptotic cells do not release their cellular constituents or invoke an inflammatory response, these cells do alter the expression of cell surface markers to enable phagocytic recognition (Elmore, 2007). Moreover, within the cell, apoptotic events include degradation of nuclear and cytoskeletal proteins, and reorganization of the cytoskeleton (Elmore, 2007), which in turn could alter intrinsic cell (and therefore tissue) mechanics. More broadly, inhibiting mitosis arrest cells at earlier stages of development, these cells have intrinsically different mechanical properties from “older” cells. The transcriptional/translational capacities of the cells may also be different resulting in alterations of tissue stiffness that are independent of cell density.

Nonetheless, at present there are no methods that will decrease cell density, without perturbing biochemistry, except potentially physical ablation of individual cells of the neuroepithelia, which is both experimentally challenging and poses its own limitations (e.g. tissue damage).

### 5.5.2 Piezo1 depletion and tissue softening

Piezo1 activation has been shown to trigger cell division in zebrafish epithelia and proliferation in *Drosophila* glioma models (Chen et al., 2018; Gudipaty et al., 2017). Conversely, Piezo1 provides negative feedback for oligodendrocyte progenitor cell proliferation and induces apoptosis in pneumocytes of acute respiratory distress syndrome-model rats (Liang et al., 2019; Segel et al., 2019). Thus, I postulated that tissue softening from Piezo1 downregulation could be the result of altered cell proliferation and density. However, the analysis of Piezo1-downregulated brains revealed that tissue stiffness can change without a change in cell body densities, suggesting that other structures also contribute to tissue mechanics. Likely contributors include both cellular constituents (e.g. nuclei, cytoskeletal elements, organelles, cell adhesion molecules, plasma membrane components) and non-cellular constituents (e.g. ECM (Moeendarbary et al., 2017)). An important follow up experiment is to parse the ECM composition of control and Piezo1-downregulated tissue.

In addition, Piezo1 activation can lead to the remodelling of cytoskeleton and cell-cell adhesions, which could in turn affect tissue stiffness. Piezo1 is important in touch sensing

but beyond its acute response, in endothelial tissue at least, this protein also controls structure formation during development, through the remodelling of cell junctions and cytoskeletal organization. For example Piezo1 is essential in the development of vasculature (Ranade et al., 2014) and in the formation of lymphatic valves (Nonomura et al., 2018) in mice. Therefore, Piezo1 downregulation could affect the organization of the cytoskeleton or junctional elements, leading to alterations in tissue structure and mechanical properties.

*In vitro* as well, Piezo1 downregulation affects stress fibre organization and cell orientation of human umbilical vein endothelial cells (HUVECs) in response to shear stress (Li et al., 2014). Furthermore, Piezo1 colocalizes and interacts with adhesion molecules that mediate cell and junctional integrity to subcellularly tune force responses, e.g. CD31 and VE-cadherin (Chuntharpursat-Bon et al., 2019).

Integrins are also involved in Piezo1 signalling. Integrins play a fundamental role in cell adhesion, coupling the cytoskeleton to the ECM when activated. siRNA knockdown of Piezo1 in epithelial cells showed poorer cell adhesion due to reduced  $\beta 1$  integrin activation (McHugh et al., 2010). In *Drosophila* glioma models, Piezo1 localized at focal adhesions, activating integrin-focal adhesion kinase (FAK) signalling and regulating ECM, resulting in increased tissue stiffness (Chen et al., 2018). Chen et al. also found that the increase in tissue stiffness further upregulated Piezo1, exhibiting a feedforward circuit between tissue stiffness and Piezo1 expression. Moreover, knocking down Piezo1 in glioblastoma cell lines resulted in a failure to assemble focal adhesion structures. I hypothesize that this could be true of *Xenopus* Piezo1 knockdown brains, especially as the retinal pigment epithelium of knockdown embryos often adhered poorly to the underlying tissue, suggesting severe adhesion defects. In conclusion, it is likely that downregulating Piezo1 affects the ECM, organization of cytoskeletal elements and intracellular adhesions which could potentially lead to tissue softening in the CNS and other organ systems.

Moreover, one should not discount that different cell types within the neuroepithelia could also inherently have different mechanical properties. For instance, glia were found to be softer than neurons (Lu et al., 2006). The spatial distribution of different cell types may also contribute to heterogenous stiffness distributions in wild-type brain tissue. For example, radial glial cells are known to play a role in maintaining the structural integrity of the retina (MacDonald et al., 2015), and how they are distributed in the neuroepithelia could affect local tissue stiffness. As the exact composition of cell types within brain tissue

of Piezo1-downregulated embryos or, indeed, in wild-type *Xenopus* embryos, has not yet been characterised in much detail, this remains an open question.

Additionally, tissue softening could then be due to cell fate changes from depleting Piezo1 early in development. Piezo1 was shown to transduce mechanical cues from the environment to direct the cell fate of human neural and mesenchymal stem cells (Pathak et al., 2014; Sugimoto et al., 2017). In mesenchymal stem cells, Piezo1 activation resulted in increased osteoblast differentiation while adipocyte differentiation was inhibited (Sugimoto et al., 2017). While these two cell types arise from the same lineage, they differentiate to produce cells with very different mechanical properties. In brain-derived human neural stem/progenitor cells (hNSPC), Piezo1 inhibition or downregulation suppressed neurogenesis and enhanced astrogenesis (Pathak et al., 2014). In support of this result, glial cells were found to be about twice as soft as neurons in acutely dissociated mouse hippocampi (Lu et al., 2006). Therefore, the decrease in tissue stiffness in *Xenopus* neuroepithelia from Piezo1 depletion, could be the result of cell fate changes resulting in non-neuronal cells. An alteration of cell fate could also account for the decrease in *sema3A* levels (as it may be the wrong type of cell to produce this guidance cue). If alterations in cell lineage were sufficient to account for the change in stiffness and decrease in *sema3A* mRNA level, depleting

Piezo1 in a more spatio-temporally controlled manner, e.g. by electroporating the *piezo1* morpholino directly in the brain or optic tract, or the use of photo-cleavable morpholinos (in which light activation on a specific tissue region enables morpholino binding), would help address this.



# 6 A NEW AND IMPROVED MORPHOLINO

In the results presented in chapters 3 - 5, Piezo1 downregulation was achieved using a translation blocking morpholino designed against the *Xenopus tropicalis piezo1* sequence (PzT MO), as at the point that we published our first works on Piezo1 (Koser et al., 2016), the full *Xenopus laevis* genome had not been sequenced yet. *X. tropicalis* is closely related to *X. laevis* and Piezo1 protein downregulation in morpholino-injected embryos could be confirmed by Western blot (Koser et al., 2016).

*X. laevis* is an excellent model organism for studying axon guidance, however, as an allotetraploid animal it is not the most genetically tractable model organism. There are two homeologs of Piezo1 (Piezo1.L and Piezo1.S). Once the *X. laevis* sequence was made available (Session et al., 2016), with help from Toshiaki Shigeoka, I found two mismatches between *X. laevis piezo1.L mRNA* and the PzT MO, while there were four mismatches between *piezo1.S mRNA* and our PzT MO (refer to Table 2). Since successful morpholino knockdown does tolerate a degree of mismatch between the morpholino and target site (Rana et al., 2006), the Piezo1.L homeolog was more likely to be downregulated by the *X. tropicalis* morpholino than the Piezo1.S homeolog.

To increase the morpholino binding specificity, I therefore designed new morpholinos based on the *Xenopus laevis piezo1.L mRNA* (PzL MO) sequence. While Western blot analysis for the PzT MO morpholino convincingly showed Piezo1 downregulation in *X. laevis* embryos, I wished to examine more critically if the downstream effects observed (e.g. optic tract defects, tissue softening, and the *sema3A* decrease presented in chapters 0 and 4 were indeed due solely to Piezo1 protein downregulation, rather than additional off-target effects. Hence, I repeated some of the experiments discussed in previous chapters with the PzL MO.

## 6.1 Piezo1 is downregulated by the *X. laevis piezo1.L* morpholino (PzL MO)

Western blots for Piezo1 using stage 40 head tissue from embryos that I injected with either the new PzL MO or the PzT MO, demonstrated a knockdown of  $42\% \pm 18\%$  or  $19\% \pm 25\%$  respectively, compared with control morpholino injected embryos (Figure 6-1). This suggested a higher downregulation efficiency with the new morpholino design, although the PzL MO might also downregulate Piezo1.S. For the purposes of my project thus far, the distinction between the two homeologs is not highly critical, as I am interested in Piezo1 knockdown in general. Furthermore, when homologous gene pairs are both expressed, the L copy expression tends to be higher than that of the S copy, in adult tissues at least (Session et al., 2016). However, for studies at much earlier stages in development, this difference might not be so distinct, because *piezo1.S* RNA is highly expressed between stages 5-10 (Karimi et al., 2018).

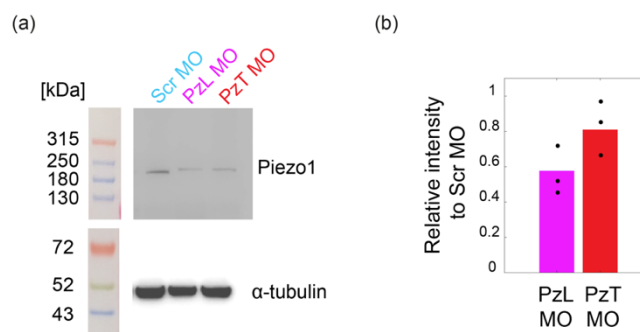


**Figure 6-1 Validation of Piezo1 downregulation using PzL MO.**

*(a) Representative Western blots of stage 40 Xenopus head tissue from double dorsal blastomere injections with Scr MO, PzL MO or PzT MO. Piezo1 was detected using a polyclonal antibody (NBP1-78446, Novus Biological, 1:500). Intensity values were normalized to alpha-tubulin (ab7291, Abcam, 1:10k). (b) Quantification from three Western blots. Each lane was normalized to the corresponding Scr MO lane. The bar shows the mean of three replicates, dots represent the mean value of each replicate (each replicate had lysates loaded in duplicate or triplicate). PzL MO significantly downregulated Piezo1 ( $p = 3.4E-4$ , one sample *t*-test on values normalized to Scr MO, from 8 measurements). PzT MO downregulated Piezo1, but the threshold of significance was not reached ( $p = 0.084$ , one sample *t*-test on values normalized to Scr MO, from 8*

*measurements*). **PzL MO: *X.laevis piezo1.L morpholino*, PzT MO: *X.tropicalis piezo1 morpholino*, Scr MO: *scrambled control morpholino*.**

## 6.2 Piezo1 downregulation with both morpholinos results in *in vivo* axon pathfinding defects

Similar to (section 3.4) I injected both dorsal blastomeres of four-cell stage embryos with 15ng/blastomere of Scr, PzT or PzL MO and visualized the optic tract in whole lateral mount brains at stage 40. In both PzT and PzL MO injected embryos, there was a decrease in axon elongation compared with controls; in PzT MO, this decrease was significant ( $p = 0.0019$ ), but the threshold of significance was not reached for PzL MO ( $p = 0.6$ ) (Figure 6-2 a). With both PzT and PzL MOs, fewer than 20% of brains had normal optic tract projections, while over 80% of control brains had normal optic tracts. In both PzT and PzL MO downregulated brains, >80% of brains had axon stalling or misprojection defects (Figure 6-2 b). These results indicate that the optic tract phenotypes observed with the PzTMO in Chapter 3 are unlikely to be the result of only random off-target event and instead is indeed the result of downregulating Piezo1, despite the 2 nucleotide mismatch. The new, more specific PzLMO provides an excellent option to downregulate Piezo1 expression in *Xenopus laevis*.

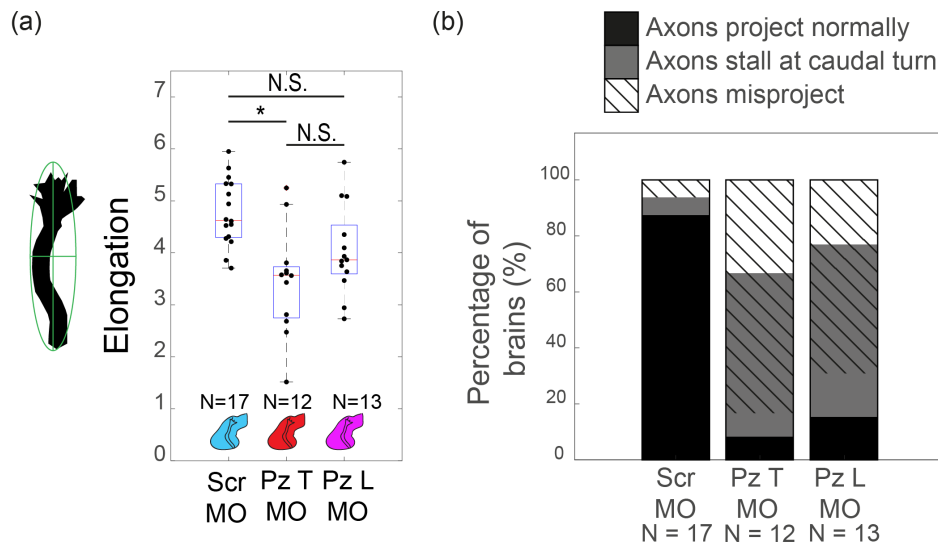


**Figure 6-2 Characterizing the optic tract of Piezo1 downregulated embryos.**

*(a) Quantification of OT elongation at stage 40. Left: example ellipse fitting to the outline of an optic tract; the ratio of long and short axes determines the elongation. Right: Boxplot shows median, first, and third quartiles; whiskers show the spread of data. N denotes the number of brains. Data was assessed with a Kruskal-Wallis test (0.025), and with a Tukey post-hoc test. Optic tract elongation was significantly different between control and PzT MO ( $p = 0.019$ ), but not between Scr and PzL MO samples ( $p = 0.6$ ) or between PzT MO and PzL MO ( $p = 0.18$ ). (b) Scoring of percentage of brains with axon guidance defects, N denotes the number of brains. PzL MO: *X. laevis piezo1.L* morpholino, PzT MO: *X.tropicalis piezo1* morpholino, Scr MO: scrambled control morpholino. Data are from two biological replicates.*

### 6.3 Brain tissue stiffness decreases with Piezo1 downregulation using PzL MO

I once more turned to AFM and acquired tissue stiffness maps of stage 40 embryos that were injected in both dorsal blastomeres, at the 4-cell stage, with either Scr MO, PzT MO or PzL MO. Piezo1 downregulation using both PzT MO and PzL MO resulted in a significant decrease in tissue stiffness compared with Scr MO-injected embryos ( $p = 3.8E-9$  and  $p = 3.8E-9$ , respectively) (Figure 6-3 a). Mean stiffness of both PzT MO and PzL MO were very similar ( $p = 0.64$ ), at  $K = 400 \pm 280$  Pa and  $394 \pm 310$  Pa respectively, while the mean stiffness of Scr MO brains was  $575 \pm 330$  Pa.

In chapter 5, I showed how cell body density scales with tissue stiffness in *Xenopus* embryonic brain development. To investigate if the altered tissue mechanics observed here resulted from changes in cell body density in the brain, I conducted a similar set of experiments as described in section 5.4. As in the PzT MO-treated brains, the nuclear density was significantly higher on the rostral side compared with the caudal side of the optic tract in all conditions studied, including both Piezo1 knockdown conditions ( $p_{Scr} = 6.3E-5$ ,  $p_{PzT} = 9.8E-4$ ,  $p_{PzL} = 0.0039$ ) (Figure 6-3 b). The nuclear density was very similar on the rostral side ( $p_{Scr vs PzT} = 0.98$ ,  $p_{Scr vs PzL} = 0.95$ ,  $p_{PzT vs PzL} = 1.0$ ) and on the caudal side ( $p_{Scr vs PzT} = 1.0$ ,  $p_{Scr vs PzL} = 0.98$ ,  $p_{PzT vs PzL} = 0.97$ ), confirming that, while Piezo1 downregulation resulted in softened brain tissue, the tissue softening is not due to a decrease in cell body densities in the brain.

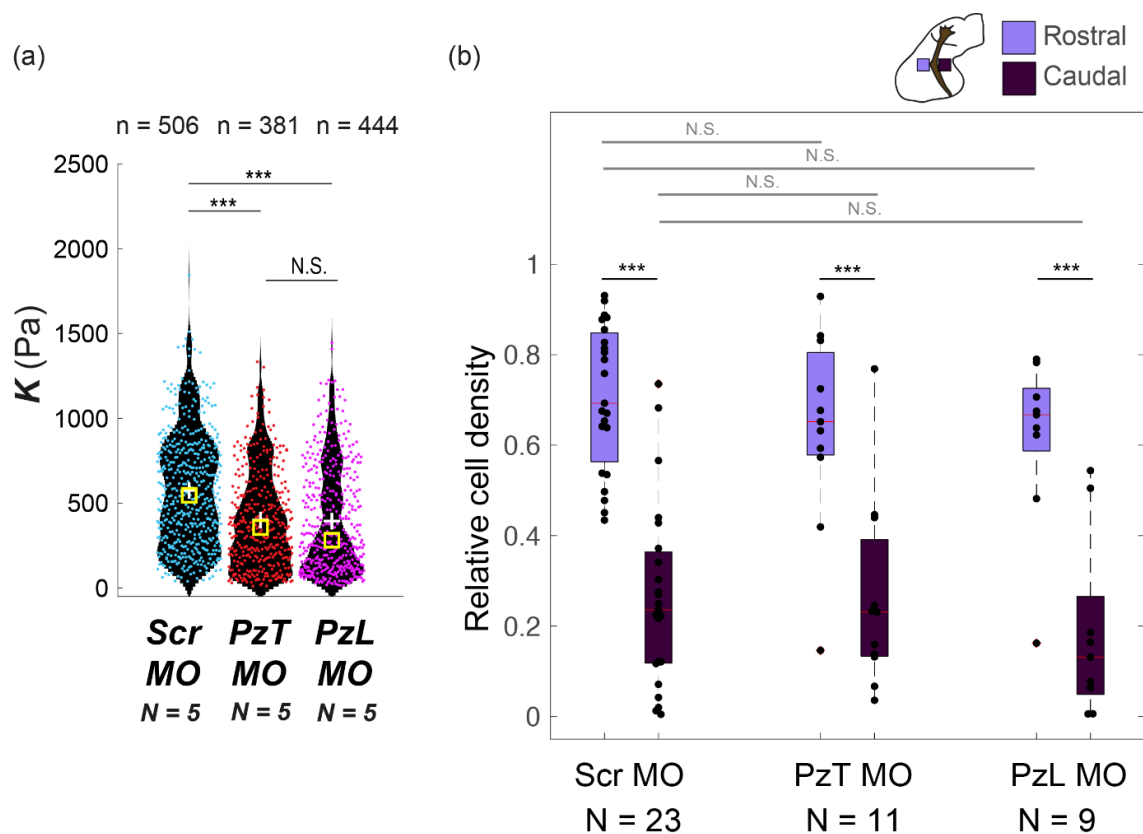


**Figure 6-3 Tissue stiffness and nuclei density distribution is very similar between PzT MO and PzL MO knockdown brains.**

*(a) AFM stiffness measurements of stage 40 brains, shown as a violin plot with the scatter of individual stiffness measurements for each condition. The means and medians*

are indicated as white crosses and yellow squares respectively.  $N$  denotes the number of brains, while  $n$  denotes the number of measurements. Data was assessed with a Kruskal-Wallis test ( $1.5E-22$ ) and with a Tukey post-hoc test. Scr MO brains were significantly stiffer than PzT MO and PzL MO brains ( $p = 3.8E-9$  and  $p = 3.8E-9$ , respectively). There was no significant difference between brain tissue stiffness of PzT MO and Pz L MO ( $p = 0.64$ ). (b) Relative cell densities are significantly higher in the region rostral of the optic tract compared with caudal to it, in the Scr MO ( $p = 6.3E-5$ ), PzT MO ( $p = 9.8E-4$ ), and PzL MO ( $p = 0.0039$ ). Data between rostral and caudal regions of each condition were assessed with a Wilcoxon signed-rank test (black significance bars). Relative cell densities were not significantly different between the rostral regions of Scr MO, PzT MO and PzL MO. Similarly, relative cell densities were not significantly different between caudal regions for all samples. Data across different samples were assessed with a Kruskal-Wallis test ( $9.1E-9$ ) and with a Tukey post-hoc test.  $N$  denotes the number of brains assessed. Boxes show the 25th, 50th (median), and 75th percentiles; whiskers show the spread of the data.  $*p \leq 0.05$ ,  $**p \leq 0.01$ ,  $***p \leq 0.001$ . N.S. = not significant. PzL MO: *X.laevis piezo1.L morpholino*, PzT MO: *X.tropicalis piezo1 morpholino*, Scr MO: scrambled control morpholino.

#### 6.4 *Sema3A* RNA expression is attenuated with PzL MO depletion of Piezo1 in the CNS

Besides mechanically characterizing the brain, I confirmed that *sema3A* expression was attenuated in the whole PzL MO-treated embryo. *In situ* hybridization with an antisense *sema3A* probe was conducted on whole embryos at stage 40 (as described in 0), comparing the different Piezo1 morpholinos. While the data with PzL MO is from a pilot study with a single biological replicate, and we will need to repeat these experiments to test for statistical significance, Piezo1 downregulation in the CNS appears to result in a global decrease of *Sema3A* RNA expression in knockdown tissue for both PzT MO and PzL MO (Figure 6-4 a, b).

To study *sema3A* expression more quantitatively, I verified these results using qPCR. *Sema3A* expression in the telencephalon was compared against four different reference genes (Figure 6-4 c). While an ANOVA with a Bonferroni post-hoc test did not detect significance for all of the reference genes (except in *mtch21* and *sub11*,  $p = 0.029$  and  $p =$

0.029, respectively)– there was a trend towards decreased *sema3A* expression in both PzT MO and PzL MO downregulated-brains compared with controls.

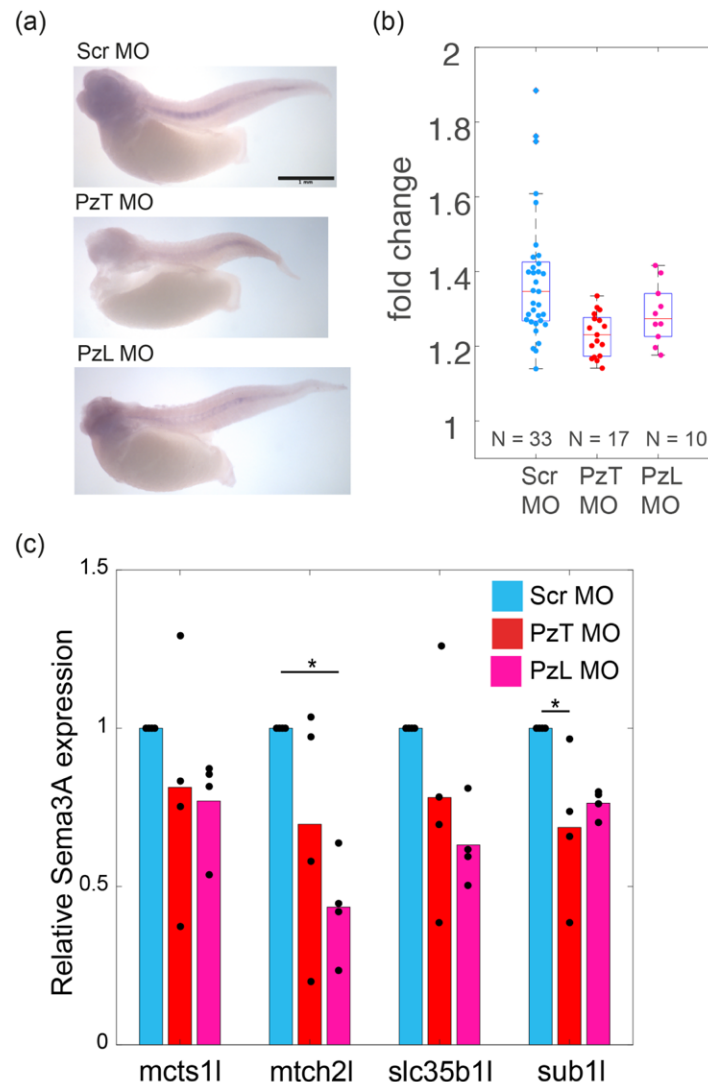


**Figure 6-4 *Sema3A* RNA expression is attenuated when Piezo1 is downregulated.**

*(a) Representative images of in situ hybridization a *sema3A* antisense probe on stage 40 Scr MO, PzT MO and PzL MO embryos. Scale bar is 1 mm. (b) Plot of fold change of *sema3A* mRNA expression in Scr MO, PzT MO, and PzL MO. Fold change of *sema3A* expression for each embryo was taken as the mean ratio of the maximum intensity to background for sequential perpendicular line profiles that were made across a region of interest (schematic of analysis method for obtaining fold change is shown in Figure 4-3). N denotes the number of embryos assessed. Means are indicated by red lines. Fold change is taken as the ratio of the average maximum intensity to background. Data is*

for one biological replicate. (c) qPCR analysis of relative *sema3A* expression levels in Scr MO, PzT MO and PzL MO compared with various reference genes (labelled on the x-axis). The bars indicate the mean of four biological replicates, the data for individual replicates are scattered over the bar. For each reference gene, the PzL MO or PzT MO injected embryos *sema3A* expression levels were normalized to Scr MO injected embryos *sema3A* levels. Data was assessed by an ANOVA followed by a Bonferroni post hoc test. The ANOVA identified significance between the three conditions for *mtch2.L* and *sub1.L* (0.029 for both) but no significance between the conditions for *mcts1.L* and *slc35b1L* (0.38 and 0.11 respectively). *Sema3A* RNA expression was significantly lower in PzL MO injected embryos, compared with Scr MO when *mtch2.L* was taken as the reference gene ( $p = 0.0283$ ). *Sema3A* RNA expression was significantly lower in PzT MO injected, with *sub1.L* as a reference gene ( $p = 0.035$ ). With all the conditions, there was a trend towards decrease in *sema3A* RNA expression with *Piezo1* downregulation, regardless if PzT MO or PzL MO were injected.  $*p \leq 0.05$ ,  $**p \leq 0.01$ ,  $***p \leq 0.001$ . PzL MO: *X.laevis piezo1.L* morpholino, PzT MO: *X.tropicalis piezo1* morpholino, Scr MO: scrambled control morpholino.

## 6.5 Summary

I found that the effects of *Piezo1* downregulation using PzL MO were very similar to those of PzT MO. Axon pathfinding defects occurred when either of the *Piezo1* morpholinos were used. Brain tissue was also significantly softer compared with controls and the cell body density distribution between PzT MO and PzL MO were very similar. Additionally, I found (both with *in situ* hybridization and qPCR) that *sema3A* mRNA expression was attenuated when *Piezo1* was downregulated with either PzT MO or PzL MO. In conclusion, the effects of *Piezo1* downregulation with PzT MO and PzL MO are very similar, and the results discussed in the preceding chapters are highly likely to be direct results of decreased *Piezo1* expression rather than random off-target effects of the morpholinos used. Furthermore, *in vitro* eye primordia explants cultures from PzL MO injected embryos had highly improved adhesion rates compared with PzT MO (Foster, 2020). Therefore, the new morpholino is more specific and likely to be superior to the PzT MO.

As *Piezo1* depletion resulted in both changes in tissue mechanics and *sema3A* levels, the question remains if reduced tissue stiffness caused the decrease in *sema3A* expression or

if conversely, the reduction in *sema3A* mRNA expression resulted in altered tissue mechanics? The next chapter veers from axon guidance towards a better understanding of the relationship between tissue mechanics and Sema3A levels.

## Acknowledgments

Western blot and protein quantification in Figure 6-1 were done by Katrin Mooslehner.

AFM mapping and data analysis in Figure 6-3 (a) were done in collaboration with Amelia J. Thompson.

In situ hybridizations of whole *Xenopus* embryos in Figure 6-4 (a) were done by David Mafullul, for a summer studentship under my supervision.

RNA extraction and qPCR in Figure 6-4 (c) were done with assistance from Katrin Mooslehner and Ross McGinn.



# 7 THE RELATIONSHIP BETWEEN TISSUE MECHANICS, SEMA3A, AND PIEZO1

In the previous chapters, I characterized Piezo1-downregulated neuroepithelia and found that both tissue stiffness and *sema3A* mRNA levels were decreased. This chapter describes my experiments to unravel causal relationships between Piezo1 activity, Sema3A expression, and tissue mechanics. Does Piezo1 activity regulate tissue stiffness and tissue stiffness Sema3A levels? Or, *vice versa*, does Piezo1 activity regulate Sema3A levels and Sema3A levels tissue stiffness? Or are other effectors at play?

Briefly, I addressed if:

- Sema3A expression affects tissue mechanics
- environmental stiffness may change Sema3A expression
- Piezo1 activity, rather than levels, affects Sema3A expression and/or tissue mechanics

## 7.1 The effect of Sema3A downregulation on tissue mechanics

To deplete endogenous Sema3A in the neuroepithelia without altering Piezo1 levels, and to avoid developmental defects related to Sema3A depletion early in development (Osborne et al., 2005), I electroporated forebrains of stage 29/30 embryos with a *sema3A* morpholino (Sema3A MO) or scrambled control morpholino (Scr MO) rather than injecting the morpholinos at the 4-cell stage as done in the previous chapters. Embryos were left to develop to stage 40 and tissue stiffness maps were made using AFM. As the morpholinos used were fluorescein-tagged, I could visualize the brain region that had been electroporated. Hence, when screening, only embryos in which the morpholino was present in the region of interest, i.e. the brain region that normally produces Sema3A, were selected for stiffness mapping (Figure 7-1 a).

I found that brains electroporated with Sema3A MO were overall significantly stiffer than Scr MO electroporated brains ( $p = 6.0E-5$ ) (Figure 7-1 b, c). This comparison included brain regions that were adjacent to the electroporated region but had not themselves been electroporated. When only the electroporated regions were compared, Sema3A depleted tissue was significantly stiffer than control electroporated tissue ( $p = 1.3E-4$ ), whereas adjacent regions (that were non-electroporated) were not significantly different when Sema3A MO and Scr MO embryos were compared ( $p = 0.67$ ) (Figure 7-1 d, e).

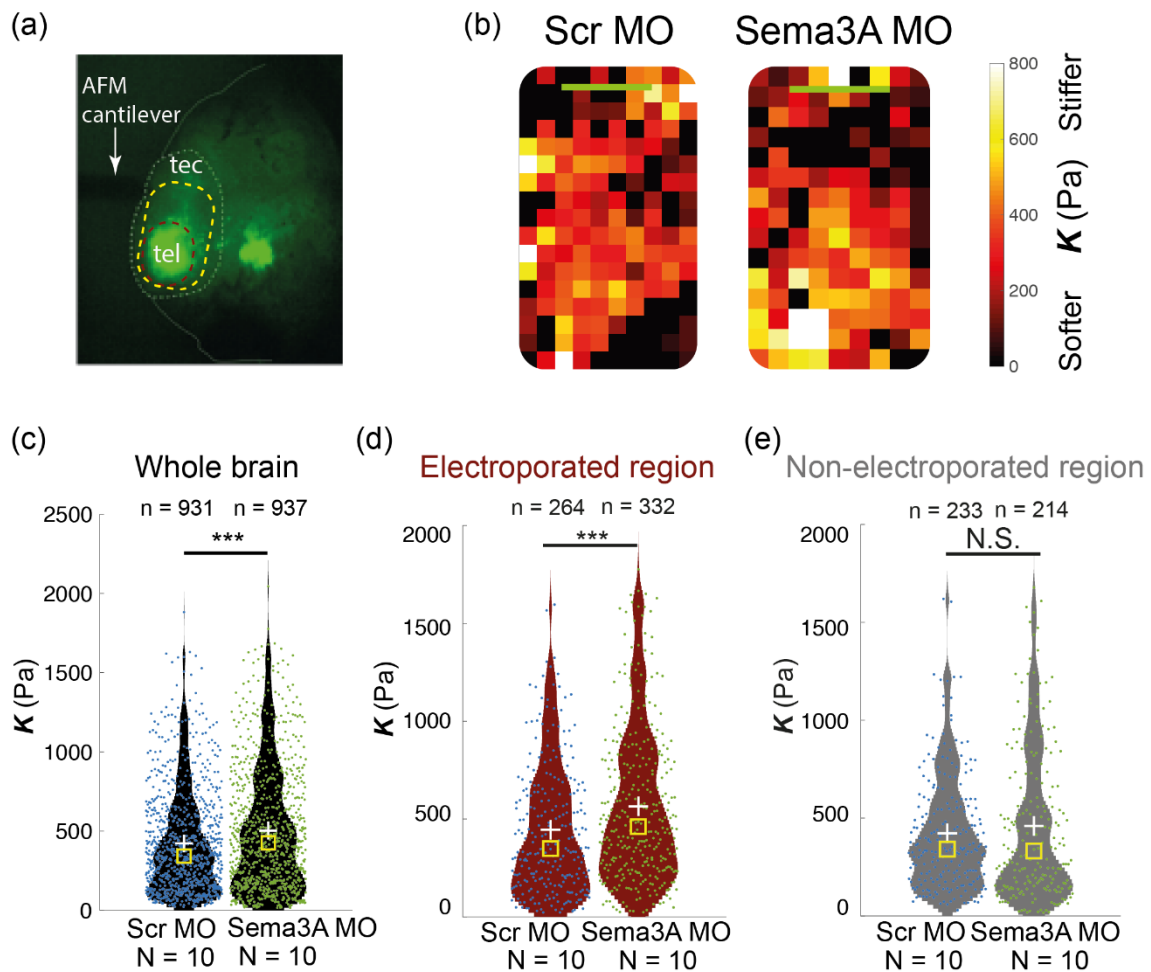


**Figure 7-1 Sema3A downregulation in the neuroepithelia resulted in tissue stiffening.**

*(a) Sample exposed brain preparation of stage 40 *Xenopus* embryos electroporated with either Scr MO or Sema3A MO. Morpholinos were fluorescein tagged, which enabled visualization of the electroporated region. The approximate region mapped by AFM for the whole brain (yellow dashed line) and electroporated region (red dashed line) is shown. (b) Representative AFM stiffness maps for stage 40 brains electroporated with a*

*Scr MO or Sema3A MO. Colour encodes the apparent elastic modulus,  $K$ , assessed at an indentation force of 10nN. Scale bars are 100  $\mu\text{m}$ . (c-d) Violin plot with scatter of individual stiffness measurements for each condition. The means and medians are indicated as white crosses and yellow squares respectively.  $N$  denotes the number of brains measured, while  $n$  denotes the number of measurements made. (c) Whole brain stiffness measurements shown that Sema3A downregulation results in a significant increase in tissue stiffness,  $p = 6.0E-5$ , data was assessed with a Wilcoxon rank-sum test. (d) Stiffness of only electroporated regions shows Sema3A downregulation results in a significant increase in tissue stiffness,  $p = 1.3E-4$ , data was assessed with a Wilcoxon rank-sum test. (e) Stiffness of non-electroporated regions, adjacent to the fluorescent region,  $p = 0.67$ , data was assessed with a Wilcoxon rank-sum test.  $*p \leq 0.05$ ,  $**p \leq 0.01$ ,  $***p \leq 0.001$ , N.S.: not significant. Sema3A MO: semaphorin3A morpholino, Scr MO: scrambled control morpholino, tec: optic tectum, tel: telencephalon.*

This result indicates that Sema3A expression does affect tissue stiffness, however, not in the direction I initially hypothesized. Previous results have shown that when brain tissue was softened -through chemical treatments, perturbing mitosis, or Piezo1 downregulation, OT axons *in vivo* were shorter (Koser et al., 2016; Thompson, Pillai et al., 2019). Similarly, both the Holt and McFarlane labs found that diminished Sema3A levels resulted in axons stalling instead of growing to the tectum (Atkinson-Leadbetter et al., 2010; Leung et al., 2013). Thus, I expected that depleting Sema3A would result in lower tissue stiffness. The effect of Sema3A perturbation on tissue stiffness will be discussed more extensively in the discussion section. However, this result does indicate that Sema3A reduction in the Piezo1 downregulated tissue was not likely the cause for the decrease in tissue stiffness observed in those embryos. While we replicated all the reagents, instruments and conditions used in the Holt lab and published in (Leung et al., 2013) we will still need to verify that Sema3A protein is indeed downregulated in the electroporated tissue, for example by Western blotting.

Sema3A depletion was done by electroporation and was compared to embryos electroporated with a control construct. However, electroporation itself is a nontrivial manipulation which could on its own change tissue stiffness, thus obscuring our insight into the actual tissue mechanics changes in response to reduced *sema3A* translation. Therefore, I compared the tissue stiffness of stage 40 wild-type, Scr MO-blastomere injected, and Scr MO electroporated brain tissue (Figure 7-2). The samples used in this

comparison were not sibling embryos but were measured with similar parameters; Scr MO-blastomere injected data was obtained from the differential Piezo1 knockdown work presented earlier in Chapter 4 of this thesis, wild-type data was obtained from the control individuals in chondroitin sulphate treatment experiments (shown in section 7.2.1 below), and Scr MO electroporated results are from above.

There was no significant difference in stiffness between wild-type and Scr MO-blastomere injected brains ( $p = 0.49$ ). However, Scr MO-electroporated brains were significantly softer than wild-type ( $p = 3.8E-9$ ) and Scr MO injected ( $p = 1.0E-4$ ) brains. Thus, the electroporation method itself led to a significant softening of brain tissue and was thus not likely to be causing the observed stiffening of brains with downregulated Sema3A expression.

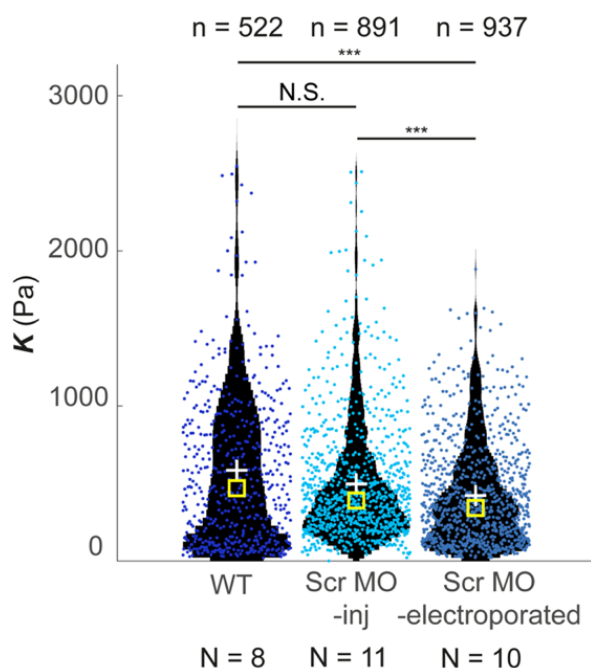


**Figure 7-2 Electroporation itself does not cause tissue stiffening.**

*Violin plot with scatter of individual stiffness measurements for wild-type, and Scr MO injected or electroporated stage 40 embryonic brains. The means and medians are indicated as white crosses and yellow squares respectively. N denotes the number of brains measured, while n denotes the number of measurements made. Wild-type brain stiffness values were not significantly different from Scr MO-blastomere injected brain tissue ( $p = 0.49$ ) but significantly stiffer than Scr MO-electroporated brain tissue ( $p = 3.8E-9$ ; Kruskal-Wallis test followed by Tukey post-hoc test.). Scr MO-blastomere injected brains were also significantly stiffer than Scr MO-electroporated brain tissue ( $p = 1.0E-4$ ).  $*p \leq 0.05$ ,  $**p \leq 0.01$ ,  $***p \leq 0.001$ . N.S.: not significant; inj: blastomere injection, Scr MO: scrambled control morpholino, WT: wild-type.*

## 7.2 The effect of environmental stiffness on *sema3A* RNA levels

My previous results demonstrated that Piezo1 downregulation resulted in tissue softening and a decrease in *sema3A* mRNA levels. However, *Sema3A* depletion alone resulted in tissue stiffening. To better understand the interaction between tissue mechanics and *Sema3A* expression levels, I next tested if mechanical perturbations (e.g. softening or stiffening the environment) altered *Sema3A* in wild-type *Xenopus* neuroepithelia. Tissue

stiffness *in vivo* and environmental stiffness *in vitro* were altered, and *sema3A* mRNA expression measured using qPCR.

### 7.2.1 Softening brain tissue *in vivo* does not significantly alter *sema3A* RNA levels

The brains of wild-type embryos were exposed at stage 33/34 and chondroitin sulfate (CS) or a control solution was bath applied. CS-treatment is known to soften brain tissue and cause axon pathfinding errors *in vivo* (Koser et al., 2016; Walz et al., 2002). The embryos were left to develop to stage 40 after which qPCR was used to quantify *sema3A* mRNA levels in the forebrain. For each replicate, I acquired tissue stiffness maps of at least one embryo per condition, to confirm that stiffness had indeed decreased following the treatment (Figure 7-3 a, b). CS-treatment significantly softened brains ( $p = 5.0E-12$ ), however *sema3A* RNA expression was not significantly altered (Figure 7-3 c). Hence, softening the brain with CS did not cause alterations of *sema3A* mRNA levels.

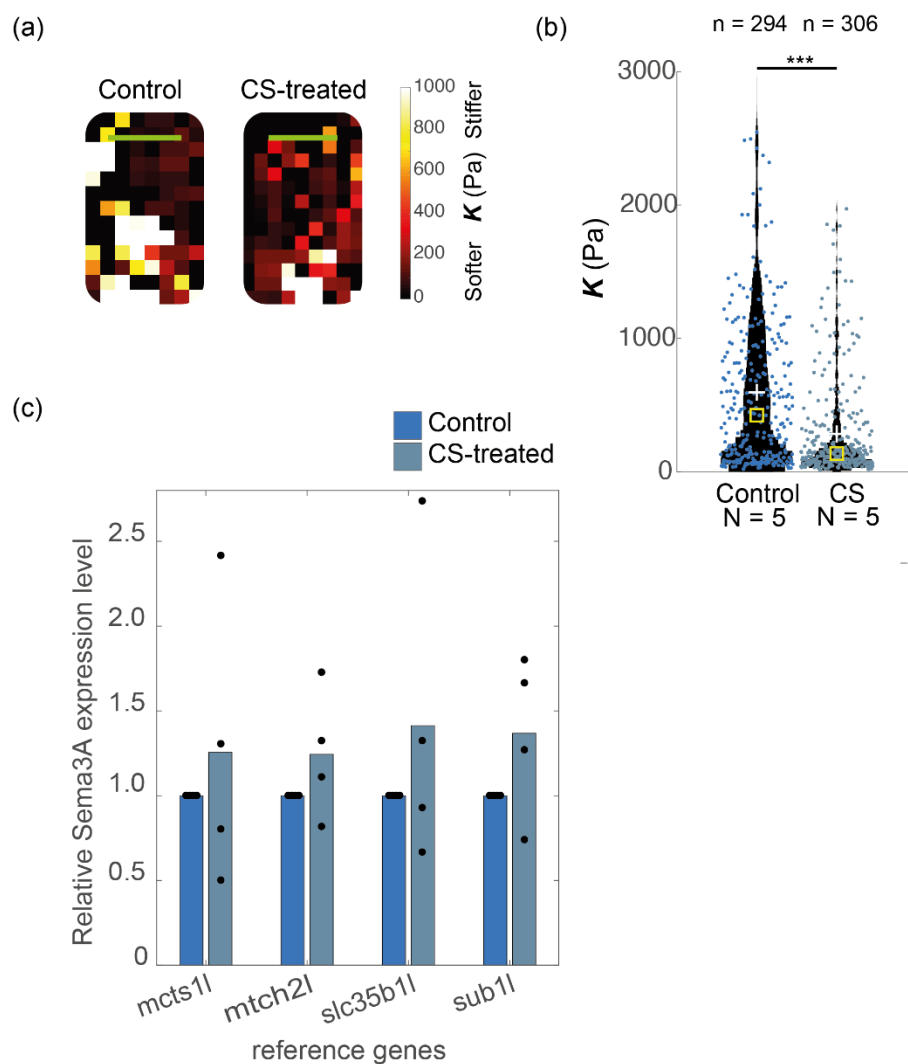


**Figure 7-3 CS treatment decreases brain tissue stiffness but does not significantly alter *sema3A* RNA levels.**

(a) Representative AFM stiffness maps control and CS-treated brain tissue at stage 40. Colour encodes the apparent elastic modulus,  $K$ , assessed at an indentation force of 10nN. Scale bars are 100  $\mu\text{m}$ . (b) Violin plot with scatter of individual stiffness measurements for each condition. The means and medians are indicated as white crosses and yellow squares respectively.  $N$  denotes the number of brains, while  $n$  denotes the number of measurements. Data was assessed with a Wilcoxon rank-sum test ( $p = 5.0E-12$ ). (c) qPCR analysis of relative *sema3A* mRNA levels in Control and CS-treated brains, compared with various reference genes. The bars indicate the mean of four biological replicates, the data for individual replicates are scattered over the bar. For each reference gene, CS-treated embryo *sema3A* mRNA expression levels were normalized to Control embryo *sema3A* mRNA expression levels. Data was assessed by

***an ANOVA ( $p = 0.7$ ) followed by a Bonferroni post-hoc test. There was no significant difference ( $p > 0.99$ ) between every combination of groups. CS: chondroitin sulfate.***

Softening the brain with CS however was a rather inelegant approach, as on top of reducing tissue stiffness, this treatment may alter various other tissue properties by biochemical means. For instance, CS interacts with growth factors, cell adhesion molecules, and other ECM molecules in the local environment that may regulate neuroepithelial cells' biological activity. Therefore, bath treatment of CS is likely not altering tissue mechanics without causing chemical changes in the environment.

To reduce the complexity of the system and to test more explicitly if environmental stiffness alone could alter *Sema3A* expression, I switched to an *in vitro* system.

### 7.2.2 Substrate stiffness modulates *sema3A* RNA levels *in vitro*

The telencephalon region of early stage 35-36 embryos was dissected, cells dissociated, and then cultured on a soft or stiff hydroxy-acrylamide substrate, with a shear modulus of 0.1 and 1.0 kPa respectively. These stiffnesses are representative of the lower and upper bounds of brain tissue stiffness *in vivo*. The substrates were coated with laminin and an equal number of brain regions were dissociated and plated on each gel. Substrate stiffness was verified by Ross McGinn using AFM.

RNA was extracted from the cells growing on the substrates after 24 hours in culture and *sema3A* mRNA levels were measured using qPCR. *Sema3A* mRNA levels in samples were normalized to *sema3A* mRNA values of acutely dissociated cells from the same brain region (of stage-matched sibling embryos that had not been cultured on a substrate).

For three of the four reference genes (*mcts1L*, *mtch2L* and *slc35b1L*), *sema3A* levels were higher on stiff substrates, compared with the soft. However, for one reference gene, *sub1L*, *sema3A* levels were higher on soft than stiff substrates. This experiment needs to be repeated before any strong conclusions can be drawn. From this single replicate, the data suggests that *sema3A* mRNA expression potentially scales with environmental stiffness.

### 7.2.3 *In vitro* substrate stiffness affects *sema3A* RNA expression in cells that do not usually produce *sema3A* *in vivo*

Similar to the *in vitro* experiments in 7.2.2, but here I instead dissected the hypothalamus region (where *sema3A* RNA -and presumably protein- is not normally present) and

dissociated and cultured the cells on soft (0.1kPa) or stiff (1kPa) substrates. RNA was extracted from the cells growing on the gels after 24 hours of culture and *sema3A* mRNA levels was measured using qPCR. *Sema3A* levels were normalized to RNA from acutely dissociated cells (from the same brain region). For all four reference genes, *sema3A* RNA expression was higher on stiff gels, compared with the soft. The data is from a single biological replicate and this experiment will need to be repeated before stronger conclusions can be drawn. However, this result suggests that stiffer substrates may increase *sema3A* transcription in neuroepithelial cells that normally do not produce measurable amounts of *sema3A*.

### 7.3 The effect of Piezo1 activity on brain tissue stiffness and *sema3A* RNA levels

Thus far, I have explored if *Sema3A* depletion results in a change of tissue stiffness, and if altering the environmental stiffness affects *Sema3A* expression. To re-introduce Piezo1 to the equation, I investigated if altering Piezo1 function, rather than downregulating its expression, would lead to any changes in stiffness or *sema3A* mRNA expression.

#### 7.3.1 Piezo1 inhibition

To inhibit the activity of Piezo1, I applied GsMTx4, a peptide that inhibits cationic mechanosensitive ion channels (Bae et al., 2011), to exposed stage 33/34 wild-type embryo brains. Piezo1 inhibition was to be followed by tissue stiffness mapping and investigation of *sema3A* mRNA expression. 25 $\mu$ M GsMTx4 was bath applied and embryos were left to develop to stage 40. The concentration used was based on published work from our group (Koser et al., 2016).

Unfortunately, the GsMTx4-treated embryos did not survive, while controls flourished. After several attempts, with a close to 100% death rate in treated embryos, we postulated that the GsMTx4 (Abcam) may have a different potency compared with the GsMTx4 in our published work (a gift from F. Sachs, University of Buffalo, USA). The difference in potency was confirmed *in vitro* (personal communication with Sarah Foster). Therefore, I tried a concentration titration of GsMTx4 (between 1.5 to 25 $\mu$ M). At concentrations higher than 7 $\mu$ M GsMTx4, the eight hour-overnight treatment was lethal. As the embryos survived at least 4 hours after treatment, I increased the embryo incubation temperature to accelerate development to stage 40 but this merely resulted in accelerated death rates. I

also tested GsMTx4 from a different supplier (Tocris) but found that embryo viability was exceedingly low at similar concentrations to the Abcam GsMTx4. With more careful titration, embryos survived, but just barely, between 5 to 7 $\mu$ M of GsMTx4; typically, less than 5% of embryos made it through the night. At  $\leq 5\mu$ M GsMTx4, embryos survived at the same rate as controls, however there were no discernible optic tract defects. Optic tract defects are a simple marker of altered tissue stiffness or chemical guidance molecules, suggesting that these concentrations of GsMTx4 may have been insufficient to effectively decrease Piezo1 activity. Hence, no downstream experiments were attempted (e.g. stiffness mapping or *sema3A* RNA quantification).

## 7.4 Discussion

As Piezo1 downregulation resulted in both tissue softening and a decrease in *sema3A* RNA expression, my main aim in this chapter was to disentangle if the decrease in *sema3A* resulted in tissue softening, or if tissue softening caused the decrease in, and if these effects were Piezo1-dependent.

### 7.4.1 Sema3A as a regulator of tissue stiffness

I showed that Sema3A depletion in the neuroepithelia by electroporating a translation blocking *sema3A* morpholino led to an increase in tissue stiffness. Consistent with this, chondroitinase treatment which degrades chondroitin sulphate proteoglycans thereby reducing extracellular Sema3A (Zimmer et al., 2010), produced ectopic mechanical gradients, quite notably, stiffening in the mid-diencephalon region of stage 40 *Xenopus* brains (Thompson, 2018). Chondroitinase treatment in (Thompson, 2018) was originally used to alter tissue stiffness as it degrades chondroitin sulphate proteoglycans, but from subsequent literature search, this treatment was shown to reduce extracellular Sema3A, therefore altering both biochemical and mechanical properties of the tissue. This suggests that the decrease in *sema3A* levels in Piezo1 downregulated tissue (shown in 0 and 6.4) is unlikely to be directly responsible for tissue softening.

The classical repulsive Sema3A signalling modality through plexin receptors modulates changes in cytoskeletal elements and cell adhesion, by negatively regulating actin and microtubules, and reducing cell adhesions (Hota and Buck, 2012). Any of these alterations could result in changes tissue stiffness. For example, in *Xenopus* neural crest cells, exposure to Sema3A resulted in reduced cell-matrix adhesion, smaller and more circular

cells with fewer protrusions, and a decrease in the number of large focal adhesions (Bajanca et al., 2019). Thus, the depletion of Sema3A could lead to larger and more persistent focal adhesions along with reduced actin disassembly. This could potentially lead to higher environmental stiffness as more decreased actin disassembly could result in higher cortical rigidity and therefore stiffer cells.

Conversely, in thymocytes (a hematopoietic progenitor cell type), *in vitro* Sema3A treatment resulted in cytoskeletal rearrangements, with more F-actin at the cell cortex and increased cortical stiffness (Lins et al., 2018). Furthermore, coculturing human corneal epithelial cells with Sema3A-releasing corneal fibroblasts resulted in increased E- and N-cadherin expression (Ko et al., 2010). While no direct measurements were made of tissue mechanics in this study, an increase in cadherins would likely lead to higher cell-cell adhesion, which in turn could result in increased tissue stiffness. Hence, none of these mechanisms can explain the stiffening of brain tissue after Sema3A knockdown (Figure 7-1).

However, the Sema3A receptor complex itself can also include other cell-adhesion molecules, such as L1CAM (Castellani et al., 2000). L1CAM is highly expressed in the nervous system of developing *Xenopus* (Date et al., 2019). When Sema3A is present, the cell-surface expression of L1CAM decreases, as L1CAM and neuropilin1 are endocytosed upon Sema3A binding to the receptor complex (Castellani et al., 2004). L1CAM binds several partners, such as  $\beta$ -integrins and ECM components. L1CAM also interacts with the cytoskeleton, and affects cell migration, axon branching and fasciculation (Anderson et al., 2006; Castellani et al., 2002; Dahlin-Huppe et al., 1997; Davis and Bennett, 1994; Ohyama et al., 2004; Schäfer and Frotscher, 2012). With Sema3A depletion, cell-surface expression of L1CAM might thus be higher and potentially explain why tissue stiffness was increased.

#### 7.4.1.1 The effect of Sema3A downregulation on RGC axons

Depletion of Sema3A in the neuroepithelia led to a ~40% increase in tissue stiffness; however, I did not study the effects of this stiffening on RGC axons in this work. Sema3A depletion has previously been shown to lead to partial stalling at the optic tract's caudal turn, and to axon misprojections (Leung et al., 2013). The phenotypes shown were relatively mild and quite similar to my observations in Piezo1 downregulated RGC axons. In another study where *sema3A* mRNA was downregulated alongside another critical

guidance cue, *slit1*, axons stalled dramatically at the caudal turn (Atkinson-Leadbetter et al., 2010). This is similar to the optic tract phenotype we observed when we stiffened brain tissue with transglutaminase (data not shown, and personal communication with Amelia J. Thompson, however in our transglutaminase work, we postulated that axons may have been crosslinked by the transglutaminase treatment and were thus unable to grow, rather than stiffness alone resulting in changes in axon growth). We also found that RGC axons that were presented with ectopically stiffened tissue grew away from these regions (Koser et al., 2016). Given the similarities in the phenotypes resulting from these mechanical and chemical perturbations, it would therefore be interesting to study if the depletion of Slit1 or both Sema3A and Slit1, would lead to more dramatic changes in tissue stiffness and if this may cause severe optic tract stalling.

In developing *Xenopus* brain tissue, it would be interesting to see if overexpressing or bath applying Sema3A would decrease tissue stiffness. This would help reveal the relationship between Sema3A levels and changes in brain tissue stiffness. A mechanistic explanation of this phenomenon would require closer investigation of the expression and distribution of various downstream cell adhesion molecules and cytoskeletal components.

#### 7.4.2 Environmental stiffness as a modulator of *sema3A* RNA levels

As decreasing Sema3A expression *in vivo* did not result in tissue softening, I was interested in determining if tissue softening was sufficient to induce a reduction in *sema3A* transcription in wild-type tissues. *In vivo* tissue softening by chondroitin sulphate treatment did not alter *sema3A* levels. This could suggest that tissue stiffness does not modulate *sema3A*. However, chondroitin sulphate treatment alters both mechanical and biochemical properties of *Xenopus* brain tissue (Koser et al., 2016; Walz et al., 2002), and its many chemical effects might override the effect of tissue softening. Extrinsically applied chondroitin sulphate probably softens tissue by increasing hydration through the introduction of additional sulphate groups (Koser et al., 2016; Singh et al., 2009). Other methods of tissue softening such as through mitotic blocking were avoided, as the consequences of blocking mitosis would have far more downstream consequences than alterations of Sema3A expression alone (e.g., fewer cells that are less able to produce other proteins/molecules required in normal development). The effects of tissue stiffening (for example by transglutaminase treatment, or by mechanically strain stiffening the tissue *in*

*vivo*) on *sema3A* levels have not yet been tested and would be interesting to explore in future.

To isolate the effect of mechanics from the cacophony of cues found *in vivo*, I developed an *in vitro* assay in which cells from the Sema3A expressing brain regions were cultured on substrates of different stiffnesses. The preliminary results from this assay suggest that cells cultured on stiffer substrates produce more Sema3A than those on soft. I also found that regions not otherwise thought to produce Sema3A increased Sema3A expression on stiffer gels. This pilot study strongly implies that environmental stiffness independently modulates *sema3A* mRNA expression, further replicates will be conducted to test the reproducibility of this result.

In practise however, the dissociation of cells could mean that *in vitro* observations, and in isolated single cells, may not be very representative of what occurs in brain tissue *in vivo*. Additionally, the response of these cells to changes in stiffness is not well understood, there is a possibility that reference gene levels also alter in response to substrate stiffness, which will be studied more closely in further replicates. However, the riotous mix of ECM molecules and various cell-cell interactions *in vivo* prevent simple predictions of changes in individual parameters. Therefore, this is a reasonable and promising first measure of the effect of environmental stiffness on *sema3A* transcription in neuroepithelial cells.

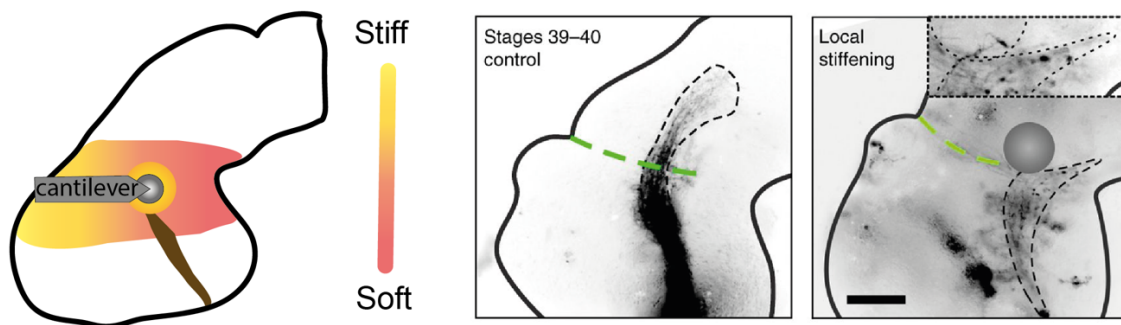
The *in vitro* experiments enabled changing exclusively environmental stiffness while ensuring that the chemical environment was identical. However, the developing brain is far more complex than a cell culture dish, and ultimately *in vitro* findings must be tested *in vivo*. While we do not yet have a method to soften tissue *in vivo* without altering the biochemical environment or affecting mitosis, we are able to stiffen tissue purely mechanically by applying a sustained compressive force to the tissue (Koser et al., 2016). This could be done in wild-type embryos to see if Sema3A expression changes. Sema3A is already expressed at the telencephalon at the stages where compression stiffening is possible, so it would not be possible to induce stiffening and check if this directly caused Sema3A expression. However, we could study at multiple developmental stages if strain stiffening increased relative *sema3A* mRNA levels compared with in non-strain stiffened stage matched embryos.

Furthermore, it would be exciting to strain stiffen a region of the brain that does not express Sema3A to see if stiffening tissue could ectopically induce Sema3A expression. From previous strain stiffening experiments, we found that axons turn away from

ectopically stiffened brain regions (Koser et al., 2016) and this may be due to a direct response to the stiffness gradient or is potentially the result of increased steric hindrance in that region of the tissue. Hypothetically, it could also be the result of an increase in *sema3A* transcription in the artificially stiffened regions, should stiffness be a direct regulator of *sema3A* RNA expression.

One caveat is that even if *Sema3A* levels are modulated by mechanical signalling, we cannot preclude that other mechanotransduction pathways (besides Piezo1 signalling) could also be involved. Another caveat is that we do not fully understand the biochemical implications of compression stiffening brain tissue, especially considering the presence of various mechanosensors and transducers in these tissues.

(a) Strain stiffening the neuroepithelia



(b) Alterations in *sema3A*?



**Figure 7-4 Perturbing in vivo tissue stiffness may alter *sema3A* RNA transcription.**

*(a) Left: Schematic illustration of local tissue stiffening by continuous indentation of the neuroepithelia with an AFM cantilever for 6 hours. This shows the outline of a Xenopus brain, the bead on the end of the cantilever indicates the indented tissue region, the optic tract is in brown, and the background colour indicates tissue stiffness (red-*

*yellow, soft-stiff). Centre: In control brains, axons grow normally. Right: In strain stiffened tissue, axons grew away from the cantilever probe (indicated by the grey circle). Scale bar is 100  $\mu\text{m}$ . the green dashed line indicates the tectal boundary, black dashed lines indicate the OT outline. Images of brains are from (Koser et al., 2016). Scale bar is 100  $\mu\text{m}$ . (b) Strain stiffening may alter *sema3A* mRNA levels. Tissue stiffness ((red-yellow, soft-stiff) and *Sema3A* RNA expression (purple) are shown together. Left: Schematic of *sema3A* levels and tissue stiffness on a control brain. Right: Schematic of hypothetical *sema3A* levels and tissue stiffness gradient shown with strain stiffening.*

### 7.4.3 Understanding the spatio-temporal dynamics of Sema3A

On top of the effects described in Figure 7-4 it would be interesting to explore if substrate stiffness modulated the expression of *sema3A* mRNA through these different development stages. Our knowledge of the localization of *sema3A* expression in *Xenopus* has been based on *in situ* hybridizations. *In situ* hybridizations can reveal RNA distribution but are only semi-quantitative and cannot provide information on protein expression. It would be useful to quantify, using qPCR for example, *sema3A* mRNA levels during these critical stages.

It would also be interesting to study if perturbing stiffness results in alterations of *sema3A* levels in the posterior tectum and other tissues which produce Sema3A, e.g. tissue regions flanking migrating neural crest cells, to see if this is a neuroepithelia-specific or more global phenomenon. Finally, it would also be exciting to study Sema3A translation between these stages, and to test more generally if translation is affected by substrate stiffness.

A significant challenge in advancing our insight into the interplay between Sema3A and tissue mechanics is that the extracellular and intracellular localization of Sema3A proteins is unknown. Adding to this quandary, Sema3A is not membrane bound but is instead secreted, requiring a fixation and staining protocol that would not wash away secreted proteins. Finding suitable antibodies for *Xenopus* immunohistochemistry is notoriously difficult and coupled with the dearth of reliable and specific Semaphorin antibodies, *sema3A* mRNA expression has been used instead of immunolabelling of proteins. One way to directly study the effects of substrate stiffness on Sema3A protein expression would be to culture neuroepithelial cells on substrates of varying stiffness and perform an ELISA

assay to quantify Sema3A protein secretion from the cells. In addition to deeper studies on the effects of substrate mechanics on Sema3A expression, future work on understanding where and how Sema3A is produced and secreted would be exceedingly useful in understanding what occurs upstream of the Sema3A signalling pathway.

If Sema3A transcription or translation is indeed mechanically regulated, this potentially implies that Sema3A is downstream of or converges with Piezo1 signalling. A better understanding of where these two signalling pathways converge may explain why Piezo1 downregulation results in tissue softening and a reduction of *sema3A* levels (though these two effects may be independent of Sema3A signalling).

#### 7.4.4 Piezo1 activity in tissue mechanics and *sema3A* expression

It was not possible to ascertain how alterations of Piezo1 activity affected tissue mechanics of *sema3A* expression, since the GsTMx4 experiments were thus far unsuccessful. A further consideration is that GsMTx4 does not block the pore of Piezo1 but instead is incorporated into the membrane, distorting tension near the channel (Gnanasambandam et al., 2017). Thus, the transfer of force from the bilayer to channel is less efficient, resulting in decreased channel activity. In that sense, I would be decreasing Piezo1 activity but also affecting the membrane properties of tissues in contact with the treatment. Hence, it is unclear if making stiffness measurements of the brain tissue would yield meaningful data for comparison with Piezo1 downregulation. While the mechanism of GsMTx4 is still not well-understood, Piezo1 pharmacology is in its infancy and GsMTx4 was the most selective of the available options (e.g. Ruthenium Red and Gadolinium), hence its use in this work. It would be useful to reattempt these experiments when a more specific Piezo1 inhibitor is found.

An alternative strategy would be to activate rather than inhibit Piezo1. A range of small molecule agonists specific to Piezo1 have been synthesized in the last few years; quite ingeniously named Yoda1 (Syeda et al., 2015), Jedi1 and Jedi2 (Wang et al., 2018). I hope to test these agonists *in vivo* in future.

Another distinct possibility, unless the results in 7.2.2 and 7.2.3 can be replicated, is that *sema3A* levels are entirely independent of environmental stiffness. Besides decreasing tissue stiffness and attenuating *sema3A* expression, Piezo1 downregulation may be altering embryonic development at a more fundamental level and cell fate decisions could be

affected (discussed in section 5.5.2), as the morpholino is injected already at the four-cell stage, long before the nervous system forms. A change in cell fate may account for both the decreased tissue stiffness and the inability of the neuroepithelial cells to effectively produce *sema3A*.

While several encouraging findings came out of these experiments, there is more to be done in clearly disentangling environmental mechanics from Sema3A expression and to explore where the pieces fall in place with regards to Piezo1 downregulation. The latter will be easier to study with the advent of new Piezo1 genetic and pharmacological tools.

## Acknowledgments

All AFM mapping and data analysis were done in collaboration with Amelia J. Thompson. RNA extraction and qPCR in Figure 7-3 (c) and described in section 7.2.2 and 7.2.3 were done with assistance from Katrin Mooslehner and Ross McGinn.



# 8 CONCLUSIONS

## 8.1 Key findings

The results presented here demonstrate that Piezo1 is important in both the cell-autonomous and non-cell-autonomous regulation of retinal ganglion cell (RGC) axon guidance. As downregulation of Piezo1 in the neuroepithelia resulted in more severe axon guidance defects *in vivo* compared with downregulation in the axons alone, the rest of my project focused on the non-cell-autonomous roles of Piezo1 in axon guidance.

Chemical and mechanical cues are both known to be important in guiding RGC axons to their target, and here I found that Piezo1 depletion affected both these signalling modalities. Both tissue stiffness and levels of *sema3A* mRNA, a key chemical guidance cue involved in the formation of the mid-optic tract bend (Atkinson-Leadbetter et al., 2010; Campbell et al., 2001), were decreased when Piezo1 was downregulated.

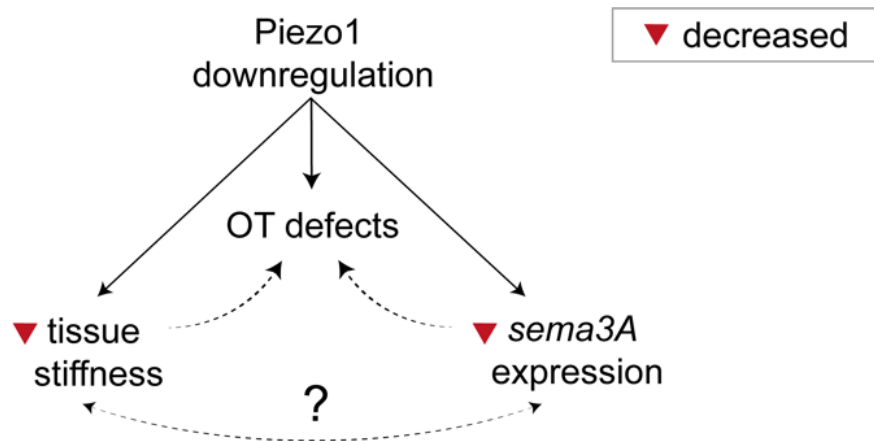


**Figure 8-1: Summary of the findings of this project.**

***Piezo1 downregulation in the developing nervous system of *Xenopus laevis* results in optic tract defects, decreased tissue stiffness, and decreased *sema3A* mRNA expression. The optic tract defects are due to attenuation of axon mechanosensing but also due to alterations in the tissue mechanics and the availability of chemical guidance cues.***

In order to determine the relationship between these two effects of Piezo1 downregulation, I then studied the effects of independently altering *Sema3A* expression or tissue mechanics, to test if (i) the decrease in tissue stiffness caused the reduction in *sema3A* or (ii) the *sema3A* decrease resulted in tissue softening. Depleting *Sema3A* protein in the forebrain did not cause a decrease in tissue stiffness, in fact brain tissue stiffness increased. On the other hand, softening the brain *in vivo* by applying chondroitin sulphate proteoglycans did not alter *sema3A* mRNA expression. Therefore, no simple causal relationship between environmental stiffness and *sema3A* levels was immediately apparent from *in vivo* experiments.

The nature of the relationship between *sema3A* and tissue stiffness may have been obscured by the different tools used and the complexity of the *in vivo* environment studied. However, when dissociated neuroepithelia cells were cultured on compliant substrates, *sema3A* RNA expression was higher on stiff compared with soft substrates, suggesting some interdependence between substrate mechanics and chemical guidance cue levels.

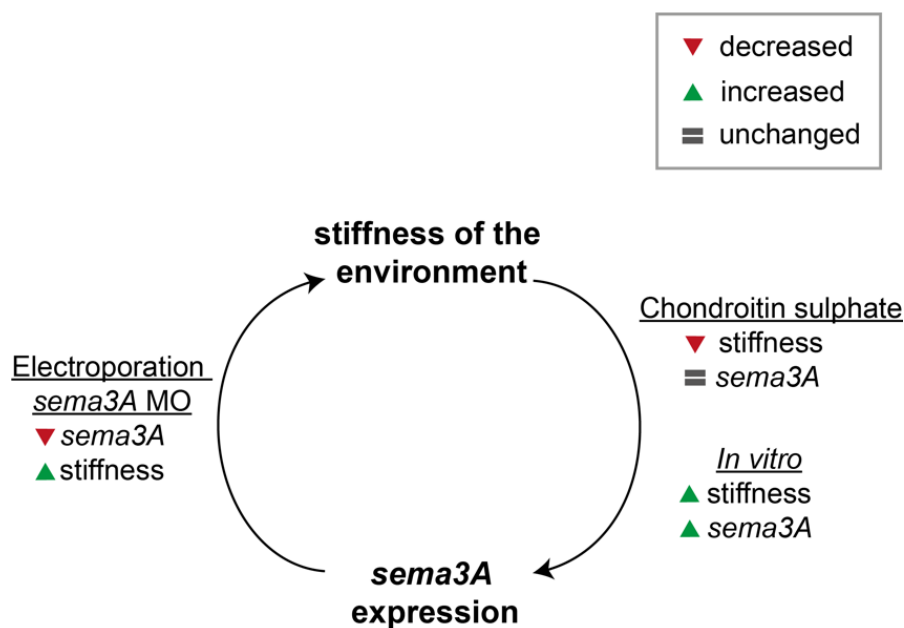


**Figure 8-2** Summary of results for independent perturbation of *sema3A* RNA expression and environmental stiffness.

*Downregulating Sema3A in vivo resulted in an increase in tissue stiffness, while decreasing tissue stiffness in vivo did not result in an alteration in sema3A RNA expression. However, increasing tissue stiffness in vitro resulted in an increase in sema3A RNA expression.*

## 8.2 Characterizing the mechanical environment of cells

The role of spatio-temporally controlled tissue mechanics in moulding the shape and form of an organism was postulated by D'Arcy Thompson over a century ago (Thompson, 1917) and has been demonstrated more recently in multitudinous tissues, in a variety of organisms (Guillot and Lecuit, 2013; Heisenberg and Bellaïche, 2013; Keller et al., 2003; Miller and Davidson, 2013). The major advances in biophysical methods such as AFM (Gautier et al., 2015), magnetic resonance elastography (Sack et al., 2008), Brillouin microscopy (Scarcelli and Yun, 2012), and magnetically responsive ferrofluid microdroplets (Serwane et al., 2017) have enabled us to measure tissue stiffness *in vivo* but often with some loss of temporal information that would be crucial in understanding the dynamics of tissue mechanics during development. Our time-lapse AFM method (Thompson, Pillai et al., 2019) has enabled us to make time-resolved measurements and therefore to study the dynamic development of tissue mechanics, *in vivo*, in an intact organism. While AFM is a brilliant method for measuring topographical features and

tissue stiffness of a surface, it is not able to obtain much information beyond the surface of the sample (Chang et al., 2012). Therefore, the study of mechanics in this thesis has been restricted to tissue stiffness. It was not possible to study other mechanical cues within the intact, live, embryo for example the 3D-architecture of the brain tissue as axons grow through it to reach their target.

From a more three-dimensional context, one could speculate that, in addition to environmental stiffness, spatial confinement may be an important mechanical cue for axons *in vivo*. Tissue with more densely packed cellular or extracellular components may appear stiffer when measured by AFM (Koser et al., 2018; Moeendarbary et al., 2017). However, one of the cues that axons could be probing in the three-dimensional tissue is space to grow into. Therefore, in ‘stiffer’ or more densely packed environments, axons are perhaps growing more directionally in space (along more clearly delineated corridors) or stalling, should space be limited (Harrison, 1914; Weiss, 1934). However, in ‘softer’ tissue that may have lower cell density (Figure 5-1) or sparser extracellular components, axons can move more freely into space (Fig 8-3). Moreover, less densely packed space could contribute to the rate and directionality of diffusing molecules (Nicholson and Tao, 1993) such as chemical guidance cues, assuming that long-range diffusion occurs in these tissues. In altering tissue stiffness *in vivo* to study the effects of tissue mechanics on axon pathfinding, we could also alter the steric environment of neurons. By contrast, in *in vitro* experiments in two-dimensional cultures, substrate stiffness can be altered without changing the steric environment. This combination of steric and stiffness-related cues may explain some of the inconsistencies between *in vitro* and *in vivo* RGC axon growth. Thus, it would be very interesting to explore 3-D tissue mechanics in an organism, when a technique with suitable spatial and temporal resolution is developed.

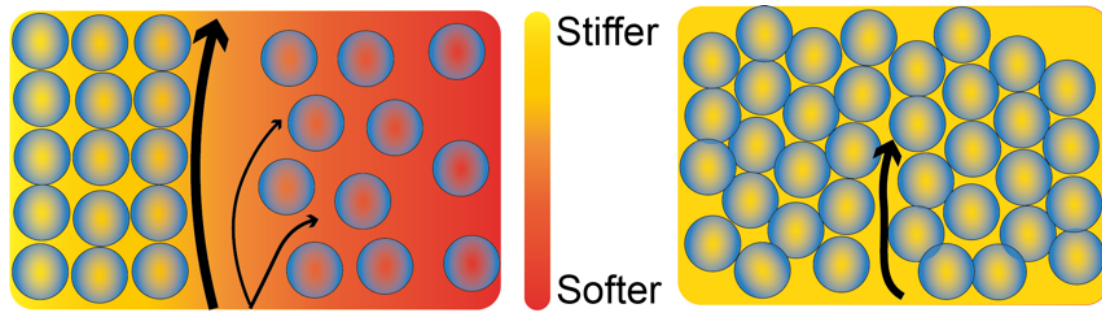


**Figure 8-3 Stiffness and steric hindrance that axons may encounter from the environment.**

*Black arrows indicate the growth path of axons. The colour gradient indicates varying environmental stiffness; red is soft and yellow is stiff. The blue circles indicate cellular or environmental components contributing to steric interference. Left: when a gradient of stiffness is found, axons grow more directionally in stiffer environments and are more exploratory in softer environments. Right: when environmental stiffness is increased, axon stalling occurs. This may be due to steric interference or crosslinking of the axons to the environment.*

### 8.3 Making sense of Piezo1 downregulation

The means by which cells sense and respond to the intricacies of the complex mechanical environment led me to the study of the MSC Piezo1. Piezo1 was discovered under a decade ago and there have been several breakthroughs revealing the structure of this protein since (Lewis and Grandl, 2015; Saotome et al., 2018; Volkers et al., 2014; Wang et al., 2018; Wu et al., 2017; Zhao et al., 2018; Zhao et al., 2019). However, at present, little is known about how Piezo1 is activated or what the downstream signalling cascade induces. Predicting the effects of Piezo1 downregulation is not trivial as the stimuli that control Piezo1 activation *in vivo* is poorly characterized and this MSC is permeant to a number of cations, including  $\text{Ca}^{2+}$  (Coste et al., 2010).  $\text{Ca}^{2+}$ -signalling is implicated in many physiological processes, including gene transcription, differentiation, cell shape and migration, apoptosis, proliferation, and contractility (Clapham, 2007; Tsai et al., 2015). However, one thing that seems to be clear thus far is that Piezo1 is activated purely by mechanical signals (Blumenthal et al., 2014; Coste et al., 2010; Pathak et al., 2014; Ranade

et al., 2014; Syeda et al., 2016), and so far there is no evidence of this MSC responding to chemical molecules in the literature.

The data in this thesis showed that Piezo1 modulates the availability of the chemical guidance cue Sema3A, possibly at least partly through a modification of tissue stiffness. To determine if stiffness is a general signal used to modulate the expression and activity of chemical signals, it would be valuable to investigate, for example, the expression of other guidance cues, and in other systems beyond the CNS, as a function of Piezo1 activity. Furthermore, it would be important to look at signalling cascades upstream of guidance cue expression to identify how Piezo1 signalling might be influencing their expression levels. Atkinson et al. showed that fibroblast growth factor (FGF) signalling to neuroepithelial cells maintains *sema3a* and *slit1* mRNA expression (Atkinson-Leadbetter et al., 2010). If *slit1* is also affected by Piezo1 downregulation, it is possible that FGF signalling, upstream of these guidance cues, has been perturbed. Intracellular signalling downstream of the FGF receptors regulating these guidance cues converge along the PI3K-Akt signalling pathway (Yang et al., 2019), one of the signalling pathways that positively correlates with Piezo1 expression in pathway mapping of gene networks in human glioblastomas (Chen et al., 2018).

## 8.4 Piezo1 and Sema3A in other tissues

I studied Piezo1 and Sema3A in axon guidance and nervous system development; however, expression of these proteins overlaps in numerous tissues, raising the possibility that Piezo1 and Sema3A signalling could interact in other systems as well.

Two systems of particular interest are bones and vasculature, both of which are constantly mechanically stimulated by force- loading on the muscular-skeletal system and shear stresses by fluids flowing in the vessels, respectively. The critical role of physical forces on healthy human physiology is easily demonstrated by the effects of space flights beyond Earth's magnetosphere on astronauts. Due to prolonged mechanical unloading, astronauts on long-term space flights have decreased bone density, with biomarker tests suggesting that bone resorption by osteoclasts exceeded bone formation by osteoblasts, and muscle atrophy upon returning to the surface (Oganov and Bogomolov, 2011; Sibonga et al., 2007; Williams et al., 2009); while in space, the astronauts had increased cardiac output and dilated vasculature from the onset of weightlessness (Norsk et al., 2006). Piezo1 is

expressed in these tissues and plays an important role in their development and maintenance. Additionally, *Sema3A* is also important in bone and vascular development and maintenance. Thus, there may be complimentary or converging interactions between *Piezo1* and *Sema3A*.

In bones, *Sema3A* is critical in bone formation and maintenance, and *Piezo1* has recently been shown to play an important role in similar pathways. *Sema3* mutant mice and *Sema3A* knockout rats had abnormal embryonic bones (Behar et al., 1996; Gomez et al., 2005). Similarly, conditional knockout of *Piezo1* in osteoblasts and/or osteocytes resulted in mice with severely impaired bone formation and reduced bone mass (Li et al., 2019; Sun et al., 2019). In terms of bone maintenance, *Sema3A* was found to suppress bone resorption by osteoclasts while increasing osteoblastic bone formation (Hayashi et al., 2012). Correspondingly, conditional knockout of *Piezo1* in osteocytes resulted in mice that were more prone to fractures due to decreased osteoblastic bone formation (Li et al., 2019). A potential interplay between *Piezo* and *Sema3A* signalling has, however, not been investigated yet.

Both proteins also play an important role in vascular development. *Sema3A* null mice showed vascular defects, with abnormal patterning of vasculature in the head and trunk of embryos (Serini et al., 2003). Endothelial specific depletion of *Piezo1* led to disruption of vascular development in the mouse embryo and yolk sac (Li et al., 2014; Ranade et al., 2014). *Piezo1* depletion has more devastating consequences, suggesting the protein may have more critical functions in other developmental processes that are likely to be upstream of *Sema3A* signalling.

*Sema3A* signalling is highly conserved, and the importance of *Sema3A* signalling in so many systems that are also regulated by mechanical cues raises the intriguing possibility that *Piezo1* signalling may be a very general mechanism by which *Sema3A* signalling, and very likely also many other chemical signalling pathways, are regulated.

### 8.5 Final remarks

In this project, I have shown that *Piezo1* signalling is crucial in axon guidance in both a cell-autonomous and non-cell-autonomous manner. *Piezo1* is not only involved in cellular mechanosensing but it also seems to regulate the mechanical properties of the surrounding tissue. In addition, I have demonstrated *in vivo* that the perturbation of *Piezo1* led to the

alteration of a key chemical signal. Some preliminary results presented in this thesis suggest that tissue stiffness may alter levels of *sema3A*, suggesting that mechanical signals could generally regulate gene transcription *in vivo*. Transcriptional activity, on the other hand, can impact tissue mechanics, as for example Piezo1 downregulation leads to tissue softening. Hence, chemical and mechanical signalling are tightly interconnected, but how the different types of signals are integrated by cells and tissues is currently poorly understood and remains subject to future studies. Here, I have provided first evidence that the presence of a key chemical signal *in vivo* is dependent on appropriate mechanical signalling. This could have major implications for the general understanding of the regulation of many biological processes in development, physiology, and pathophysiology.

ॐ पूर्णमदः पूर्णमिदं पूर्णात्पुर्णमुदच्यते

पूर्णश्च पूर्णमादाय पूर्णमेवावशिष्यते ॥

ॐ शान्तिः शान्तिः शान्तिः ॥

# 9 REFERENCES

- Aizawa, H., Wakatsuki, S., Ishii, A., Moriyama, K., Sasaki, Y., Ohashi, K., Sekine-Aizawa, Y., Sehara-Fujisawa, A., Mizuno, K., Goshima, Y., et al. (2001). Phosphorylation of cofilin by LIM-kinase is necessary for semaphorin 3A-induced growth cone collapse. *Nat. Neurosci.* **4**, 367–373.
- Alto, L. T. and Terman, J. R.** (2017). Semaphorins and their Signaling Mechanisms. In *Methods in Molecular Biology*, pp. 1–25.
- Anava, S., Greenbaum, A., Jacob, E. Ben, Hanein, Y. and Ayali, A.** (2009). The Regulative Role of Neurite Mechanical Tension in Network Development. *Biophys. J.* **96**, 1661–1670.
- Anderson, R. B., Turner, K. N., Nikonenko, A. G., Hemperly, J., Schachner, M. and Young, H. M.** (2006). The Cell Adhesion Molecule L1 Is Required for Chain Migration of Neural Crest Cells in the Developing Mouse Gut. *Gastroenterology* **130**, 1221–1232.
- Atkinson-Leadbetter, K., Bertolesi, G. E., Hehr, C. L., Webber, C. A., Cechmanek, P. B. and McFarlane, S.** (2010). Dynamic Expression of Axon Guidance Cues Required for Optic Tract Development Is Controlled by Fibroblast Growth Factor Signaling. *J. Neurosci.* **30**, 685–693.
- Bae, C., Sachs, F. and Gottlieb, P. A.** (2011). The mechanosensitive ion channel Piezo1 is inhibited by the peptide GsMTx4. *Biochemistry* **50**, 6295–300.
- Bajanca, F., Gougnard, N., Colle, C., Parsons, M., Mayor, R. and Theveneau, E.** (2019). In vivo topology converts competition for cell-matrix adhesion into directional migration. *Nat. Commun.* **10**, 1518.
- Barriga, E. H., Franze, K., Charras, G. and Mayor, R.** (2018). Tissue stiffening coordinates morphogenesis by triggering collective cell migration in vivo. *Nature* **554**, 523–527.
- Behar, O., Golden, J. A., Mashimo, H., Schoen, F. J. and Fishman, M. C.** (1996). Semaphorin III is needed for normal patterning and growth of nerves, bones and heart. *Nature* **383**, 525–528.

- Behar, O., Mizuno, K., Badminton, M. and Woolf, C. J.** (1999). Semaphorin 3A growth cone collapse requires a sequence homologous to tarantula hanatoxin. *Proc. Natl. Acad. Sci.* **96**, 13501–13505.
- Betz, T., Koch, D., Lu, Y.-B., Franze, K. and Kas, J. A.** (2011). Growth cones as soft and weak force generators. *Proc. Natl. Acad. Sci.* **108**, 13420–13425.
- Blumenthal, N. R., Hermanson, O., Heimrich, B. and Shastri, V. P.** (2014). Stochastic nanoroughness modulates neuron-astrocyte interactions and function via mechanosensing cation channels. *Proc. Natl. Acad. Sci. U. S. A.* **111**, 16124–9.
- Bradbury, E. J., McMahon, S. B. and Ramer, M. S.** (2000). Keeping in touch: sensory neurone regeneration in the CNS. *Trends Pharmacol. Sci.* **21**, 389–394.
- Bray, D.** (1979). Mechanical tension produced by nerve cells in tissue culture. *J. Cell Sci.* **37**, 391–410.
- Bray, D.** (1984). Axonal growth in response to experimentally applied mechanical tension. *Dev. Biol.* **102**, 379–389.
- Brose, K. and Tessier-Lavigne, M.** (2000). Slit proteins: key regulators of axon guidance, axonal branching, and cell migration. *Curr. Opin. Neurobiol.* **10**, 95–102.
- Buck, K. B. and Zheng, J. Q.** (2002). Growth Cone Turning Induced by Direct Local Modification of Microtubule Dynamics. *J. Neurosci.* **22**, 9358–9367.
- Cagnetta, R., Frese, C. K., Shigeoka, T., Krijgsveld, J. and Holt, C. E.** (2018). Rapid Cue-Specific Remodeling of the Nascent Axonal Proteome. *Neuron* **99**, 29-46.e4.
- Cahalan, S. M., Lukacs, V., Ranade, S. S., Chien, S., Bandell, M. and Patapoutian, A. (2015). Piezo1 links mechanical forces to red blood cell volume. *Elife* **4**,.
- Campbell, D. S. and Holt, C. E.** (2001). Chemotropic Responses of Retinal Growth Cones Mediated by Rapid Local Protein Synthesis and Degradation. *Neuron* **32**, 1013–1026.
- Campbell, D. S., Regan, A. G., Lopez, J. S., Tannahill, D., Harris, W. A. and Holt, C. E.** (2001). Semaphorin 3A elicits stage-dependent collapse, turning, and branching in *Xenopus* retinal growth cones. *J. Neurosci.* **21**, 8538–47.
- Castellani, V., Chédotal, A., Schachner, M., Faivre-Sarrailh, C. and Rougon, G.** (2000). Analysis of the L1-Deficient Mouse Phenotype Reveals Cross-Talk between Sema3A and L1 Signaling Pathways in Axonal Guidance. *Neuron* **27**, 237–249.

- Castellani, V., De Angelis, E., Kenwrick, S. and Rougon, G.** (2002). Cis and trans interactions of L1 with neuropilin-1 control axonal responses to semaphorin 3A. *EMBO J.* **21**, 6348–6357.
- Castellani, V., Falk, J. and Rougon, G.** (2004). Semaphorin3A-induced receptor endocytosis during axon guidance responses is mediated by L1 CAM. *Mol. Cell. Neurosci.* **26**, 89–100.
- Catalan, A., Caprari, P., Rodilossi, S., Betta, P., Castellucci, M., Casazza, A., Tamagnone, L. and Procopio, A.** (2004). Cross-talk between vascular endothelial growth factor and semaphorin-3A pathway in the regulation of normal and malignant mesothelial cell proliferation. *FASEB J.* **18**, 1–20.
- Chan, C. E. and Odde, D. J.** (2008). Traction Dynamics of Filopodia on Compliant Substrates. *Science (80-. ).* **322**, 1687–1691.
- Chang, K.-C., Chiang, Y.-W., Yang, C.-H. and Liou, J.-W.** (2012). Atomic force microscopy in biology and biomedicine. *Tzu Chi Med. J.* **24**, 162–169.
- Chedotal, A. and Richards, L. J.** (2010). Wiring the Brain: The Biology of Neuronal Guidance. *Cold Spring Harb. Perspect. Biol.* **2**, a001917–a001917.
- Chen, X., Wanggou, S., Bodalia, A., Zhu, M., Dong, W., Fan, J. J., Yin, W. C., Min, H.-K., Hu, M., Draghici, D., et al.** (2018). A Feedforward Mechanism Mediated by Mechanosensitive Ion Channel PIEZO1 and Tissue Mechanics Promotes Glioma Aggression. *Neuron* **100**, 799-815.e7.
- Christ, A. F., Franze, K., Gautier, H., Moshayedi, P., Fawcett, J., Franklin, R. J. M., Karadottir, R. T. and Guck, J.** (2010). Mechanical difference between white and gray matter in the rat cerebellum measured by scanning force microscopy. *J. Biomech.* **43**, 2986–2992.
- Chuntharpursat-Bon, E., Povstyan, O. V, Ludlow, M. J., Gaunt, H. J., Baxter, P. D. and Beech, D. J.** (2019). Cell adhesion molecule interaction with Piezo1 channels is a mechanism for sub cellular regulation of mechanical sensitivity. *bioRxiv* 602532.
- Clapham, D. E.** (2007). Calcium Signaling. *Cell* **131**, 1047–1058.
- Coste, B., Mathur, J., Schmidt, M., Earley, T. J., Ranade, S., Petrus, M. J., Dubin, A. E. and Patapoutian, A.** (2010). Piezo1 and Piezo2 Are Essential Components of Distinct Mechanically Activated Cation Channels. *Science (80-. ).* **330**, 55–60.

Coste, B., Xiao, B., Santos, J. S., Syeda, R., Grandl, J., Spencer, K. S., Kim, S. E., Schmidt, M., Mathur, J., Dubin, A. E., et al. (2012). Piezo proteins are pore-forming subunits of mechanically activated channels. *Nature* 483, 176–81.

Cox, C. D., Bae, C., Ziegler, L., Hartley, S., Nikolova-Krstevski, V., Rohde, P. R., Ng, C.-A., Sachs, F., Gottlieb, P. A. and Martinac, B. (2016). Removal of the mechanoprotective influence of the cytoskeleton reveals PIEZO1 is gated by bilayer tension. *Nat. Commun.* 7, 10366.

**Cox, C. D., Bavi, N. and Martinac, B.** (2019). Biophysical Principles of Ion-Channel-Mediated Mechanosensory Transduction. *Cell Rep.* 29, 1–12.

**Crick, S. L. and Yin, F. C. P.** (2007). Assessing Micromechanical Properties of Cells with Atomic Force Microscopy: Importance of the Contact Point. *Biomech. Model. Mechanobiol.* 6, 199–210.

**Dahlin-Huppe, K., Berglund, E. O., Ranscht, B. and Stallcup, W. B.** (1997). Mutational Analysis of the L1 Neuronal Cell Adhesion Molecule Identifies Membrane-Proximal Amino Acids of the Cytoplasmic Domain That Are Required for Cytoskeletal Anchorage. *Mol. Cell. Neurosci.* 9, 144–156.

**Date, P., Ackermann, P., Furey, C., Fink, I. B., Jonas, S., Khokha, M. K., Kahle, K. T. and Deniz, E.** (2019). Visualizing flow in an intact CSF network using optical coherence tomography: implications for human congenital hydrocephalus. *Sci. Rep.* 9, 6196.

**Davis, J. Q. and Bennett, V.** (1994). Ankyrin binding activity shared by the neurofascin/L1/NrCAM family of nervous system cell adhesion molecules. *J. Biol. Chem.* 269, 27163–27166.

**Deiner, M. S., Kennedy, T. E., Fazeli, A., Serafini, T., Tessier-Lavigne, M. and Sretavan, D. W.** (1997). Netrin-1 and DCC Mediate Axon Guidance Locally at the Optic Disc: Loss of Function Leads to Optic Nerve Hypoplasia. *Neuron* 19, 575–589.

**Eisen, J. S. and Smith, J. C.** (2008). Controlling morpholino experiments: don't stop making antisense. *Development.*

Ellefsen, K. L., Holt, J. R., Chang, A. C., Nourse, J. L., Arulmoli, J., Mekhdjian, A. H., Abuwarda, H., Tombola, F., Flanagan, L. A., Dunn, A. R., et al. (2019). Myosin-II mediated traction forces evoke localized Piezo1-dependent Ca<sup>2+</sup> flickers. *Commun. Biol.* 2, 298.

- Elmore, S.** (2007). Apoptosis: A Review of Programmed Cell Death. *Toxicol. Pathol.* **35**, 495–516.
- Engle, E. C.** (2010). Human Genetic Disorders of Axon Guidance. *Cold Spring Harb. Perspect. Biol.* **2**, a001784–a001784.
- Engler, A. J., Carag-Krieger, C., Johnson, C. P., Raab, M., Tang, H.-Y., Speicher, D. W., Sanger, J. W., Sanger, J. M. and Discher, D. E. (2008). Embryonic cardiomyocytes beat best on a matrix with heart-like elasticity: scar-like rigidity inhibits beating. *J. Cell Sci.* **121**, 3794–3802.
- Erskine, L. and Herrera, E.** (2007). The retinal ganglion cell axon's journey: Insights into molecular mechanisms of axon guidance. *Dev. Biol.* **308**, 1–14.
- Erskine, L., Williams, S. E., Brose, K., Kidd, T., Rachel, R. A., Goodman, C. S., Tessier-Lavigne, M. and Mason, C. A.** (2000). Retinal Ganglion Cell Axon Guidance in the Mouse Optic Chiasm: Expression and Function of Robos and Slits. *J. Neurosci.* **20**, 4975–4982.
- Falk, J., Drinjakovic, J., Leung, K., Dwivedy, A., Regan, A. G., Piper, M. and Holt, C. E.** (2007). Electroporation of cDNA/Morpholinos to targeted areas of embryonic CNS in *Xenopus*. *BMC Dev. Biol.* **7**, 107.
- Fan, J. and Raper, J. A.** (1995). Localized collapsing cues can steer growth cones without inducing their full collapse. *Neuron* **14**, 263–274.
- Foster, S. K.** (2020). Substrate stiffness tunes the neuronal response to the chemical guidance cue semaphorin3A.
- Fournier, A. E., Nakamura, F., Kawamoto, S., Goshima, Y., Kalb, R. G. and Strittmatter, S. M.** (2000). Semaphorin3A enhances endocytosis at sites of receptor-F-actin colocalization during growth cone collapse. *J. Cell Biol.* **149**, 411–22.
- Franze, K.** (2013). The mechanical control of nervous system development. *Development* **140**, 3069–77.
- Franze, K. and Guck, J.** (2010). The biophysics of neuronal growth. *Reports Prog. Phys.* **73**, 094601.
- Franze, K., Janmey, P. A. and Guck, J.** (2013). Mechanics in Neuronal Development and Repair. *Annu. Rev. Biomed. Eng.* **15**, 227–251.
- Fung, Y.-C.** (1993). *Biomechanics*. New York, NY: Springer New York.

- Gaub, B. M. and Müller, D. J.** (2017). Mechanical Stimulation of Piezo1 Receptors Depends on Extracellular Matrix Proteins and Directionality of Force. *Nano Lett.* **17**, 2064–2072.
- Gautier, H. O. B., Thompson, A. J., Achouri, S., Koser, D. E., Holtzmann, K., Moeendarbary, E. and Franze, K. (2015). Atomic force microscopy-based force measurements on animal cells and tissues. pp. 211–235.
- Ge, J., Li, W., Zhao, Q., Li, N., Chen, M., Zhi, P., Li, R., Gao, N., Xiao, B. and Yang, M. (2015). Architecture of the mammalian mechanosensitive Piezo1 channel. *Nature* **527**, 64–69.
- Geiger, B., Spatz, J. P. and Bershadsky, A. D.** (2009). Environmental sensing through focal adhesions. *Nat. Rev. Mol. Cell Biol.* **10**, 21–33.
- Giordano, A., Cesari, P., Capparuccia, L., Castellucci, M. and Cinti, S.** (2003). *Sema3A* and neuropilin-1 expression and distribution in rat white adipose tissue. *J. Neurocytol.* **32**, 345–352.
- Giuditta, A., Kaplan, B. B., Minnen, J. van, Alvarez, J. and Koenig, E.** (2002). Axonal and presynaptic protein synthesis: new insights into the biology of the neuron. *Trends Neurosci.* **25**, 400–404.
- Gnanasambandam, R., Bae, C., Gottlieb, P. A. and Sachs, F.** (2015). Ionic Selectivity and Permeation Properties of Human PIEZO1 Channels. *PLoS One* **10**, e0125503.
- Gnanasambandam, R., Ghatak, C., Yasmann, A., Nishizawa, K., Sachs, F., Ladokhin, A. S., Sukharev, S. I. and Suchyna, T. M. (2017). GsMTx4: Mechanism of Inhibiting Mechanosensitive Ion Channels. *Biophys. J.* **112**, 31–45.
- Gomez, T. M. and Letourneau, P. C.** (2014). Actin dynamics in growth cone motility and navigation. *J. Neurochem.* **129**, 221–234.
- Gomez, C., Burt-Pichat, B., Mallein-Gerin, F., Merle, B., Delmas, P. D., Skerry, T. M., Vico, L., Malaval, L. and Chenu, C.** (2005). Expression of Semaphorin-3A and its receptors in endochondral ossification: Potential role in skeletal development and innervation. *Dev. Dyn.* **234**, 393–403.
- Goodman, C. ., Kolodkin, A. ., Luo, Y., Püschel, A. . and Raper, J. .** (1999). Unified Nomenclature for the Semaphorins/Collapsins. *Cell* **97**, 551–552.
- Gordon, L., Mansh, M., Kinsman, H. and Morris, A. R.** (2010). *Xenopus* sonic hedgehog guides retinal axons along the optic tract. *Dev. Dyn.* **239**, 2921–2932.

- Goshima, Y., Yamashita, N., Nakamura, F. and Sasaki, Y.** (2016). Regulation of dendritic development by semaphorin 3A through novel intracellular remote signaling. *Cell Adh. Migr.* **10**, 627–640.
- Gottlieb, P. A., Bae, C. and Sachs, F.** (2012). Gating the mechanical channel Piezo1. *Channels* **6**, 282–289.
- Goult, B. T., Yan, J. and Schwartz, M. A.** (2018). Talin as a mechanosensitive signaling hub. *J. Cell Biol.* **217**, 3776–3784.
- Gudipaty, S. A., Lindblom, J., Loftus, P. D., Redd, M. J., Edes, K., Davey, C. F., Krishnegowda, V. and Rosenblatt, J. (2017). Mechanical stretch triggers rapid epithelial cell division through Piezo1. *Nature* **543**, 118–121.
- Guillot, C. and Lecuit, T.** (2013). Mechanics of Epithelial Tissue Homeostasis and Morphogenesis. *Science (80- )*. **340**, 1185–1189.
- Guirland, C., Suzuki, S., Kojima, M., Lu, B. and Zheng, J. Q.** (2004). Lipid Rafts Mediate Chemotropic Guidance of Nerve Growth Cones. *Neuron* **42**, 51–62.
- Guo, Y. R. and MacKinnon, R.** (2017). Structure-based membrane dome mechanism for Piezo mechanosensitivity. *Elife* **6**, e33660.
- Gurdon, J. B., Lemaire, P. and Mohun, T. J.** (1997). Chapter 3 Myogenesis in *Xenopus* Embryos. pp. 53–66.
- Hall, A. and Lalli, G.** (2010). Rho and Ras GTPases in Axon Growth, Guidance, and Branching. *Cold Spring Harb. Perspect. Biol.* **2**, a001818–a001818.
- Hans, F. and Dimitrov, S.** (2001). Histone H3 phosphorylation and cell division. *Oncogene* **20**, 3021–3027.
- Harris, W. A.** (1986). Homing behaviour of axons in the embryonic vertebrate brain. *Nature* **320**, 266–269.
- Harris, W. A.** (1989). Local positional cues in the neuroepithelium guide retinal axons in embryonic *Xenopus* brain. *Nature* **339**, 218–221.
- Harrison, R. G.** (1910). The outgrowth of the nerve fiber as a mode of protoplasmic movement. *J. Exp. Zool.* **9**, 787–846.
- Harrison, R. G.** (1914). The reaction of embryonic cells to solid structures. *J. Exp. Zool.* **17**, 521–544.
- Haselwandter, C. A. and MacKinnon, R.** (2018). Piezo’s membrane footprint and its contribution to mechanosensitivity. *Elife* **7**,

- Hayashi, M., Nakashima, T., Taniguchi, M., Kodama, T., Kumanogoh, A. and Takayanagi, H. (2012). Osteoprotection by semaphorin 3A. *Nature* 485, 69–74.
- Heisenberg, C.-P. and Bellaïche, Y.** (2013). Forces in Tissue Morphogenesis and Patterning. *Cell* 153, 948–962.
- Hertz, H. R.** (1882). Über die Berührung fester elastischer Körper und über die Harte. *Verhandlung des Vereins zur Beförderung des Gewerbefleißes, Berlin*.
- Holt, C. E.** (1989). A Single-Cell Analysis of Early Retinal Ganglion Cell Differentiation in *Xenopus*: From Soma to Axon Tip. *J. Neurosci.* 9, 3123–3145.
- Holt, C. E. and Dickson, B. J.** (2005). Sugar Codes for Axons? *Neuron* 46, 169–172.
- Holt, C. E., Bertsch, T. W., Ellis, H. M. and Harris, W. A.** (1988). Cellular determination in the *xenopus* retina is independent of lineage and birth date. *Neuron* 1, 15–26.
- Hong, K., Nishiyama, M., Henley, J., Tessier-Lavigne, M. and Poo, M.** (2000). Calcium signalling in the guidance of nerve growth by netrin-1. *Nature* 403, 93–98.
- Hornberger, M. R., Dütting, D., Ciossek, T., Yamada, T., Handwerker, C., Lang, S., Weth, F., Huf, J., Weßel, R., Logan, C., et al. (1999). Modulation of EphA Receptor Function by Coexpressed EphrinA Ligands on Retinal Ganglion Cell Axons. *Neuron* 22, 731–742.
- Hota, P. K. and Buck, M.** (2012). Plexin structures are coming: opportunities for multilevel investigations of semaphorin guidance receptors, their cell signaling mechanisms, and functions. *Cell. Mol. Life Sci.* 69, 3765–3805.
- Huber, A. B., Kolodkin, A. L., Ginty, D. D. and Cloutier, J.-F.** (2003). Signaling at the Growth Cone: Ligand-Receptor Complexes and the Control of Axon Growth and Guidance. *Annu. Rev. Neurosci.* 26, 509–563.
- Huot, J.** (2004). Ephrin signaling in axon guidance. *Prog. Neuro-Psychopharmacology Biol. Psychiatry* 28, 813–818.
- Hutson, L. D. and Chien, C.-B.** (2002). Pathfinding and Error Correction by Retinal Axons. *Neuron* 33, 205–217.
- Hutter, J. L. and Bechhoefer, J.** (1993). Calibration of atomic-force microscope tips. *Rev. Sci. Instrum.* 64, 1868–1873.
- Ichijo, H. and Kawabata, I.** (2001). Roles of the Telencephalic Cells and their Chondroitin Sulfate Proteoglycans in Delimiting an Anterior Border of the Retinal Pathway. *J. Neurosci.* 21, 9304–9314.

- Irie, A., Yates, E. A., Turnbull, J. E. and Holt, C. E.** (2002). Specific heparan sulfate structures involved in retinal axon targeting. *Development* **129**, 61–70.
- Ito, T., Kagoshima, M., Sasaki, Y., Li, C., Udaka, N., Kitsukawa, T., Fujisawa, H., Taniguchi, M., Yagi, T., Kitamura, H., et al. (2000). Repulsive axon guidance molecule Sema3A inhibits branching morphogenesis of fetal mouse lung. *Mech. Dev.* **97**, 35–45.
- Iwashita, M., Kataoka, N., Toida, K. and Kosodo, Y.** (2014). Systematic profiling of spatiotemporal tissue and cellular stiffness in the developing brain. *Development* **141**, 3793–3798.
- Journey, W. M., Gallo, G., Letourneau, P. C. and McLoon, S. C.** (2002). Rac1-Mediated Endocytosis during Ephrin-A2- and Semaphorin 3A-Induced Growth Cone Collapse. *J. Neurosci.* **22**, 6019–6028.
- Kabayama, H., Nakamura, T., Takeuchi, M., Iwasaki, H., Taniguchi, M., Tokushige, N. and Mikoshiba, K.** (2009). Ca<sup>2+</sup> induces macropinocytosis via F-actin depolymerization during growth cone collapse. *Mol. Cell. Neurosci.* **40**, 27–38.
- Kabayama, H., Takeuchi, M., Taniguchi, M., Tokushige, N., Kozaki, S., Mizutani, A., Nakamura, T. and Mikoshiba, K.** (2011). Syntaxin 1B Suppresses Macropinocytosis and Semaphorin 3A-Induced Growth Cone Collapse. *J. Neurosci.* **31**, 7357–7364.
- Kaczmarek, J. S., Riccio, A. and Clapham, D. E.** (2012). Calpain cleaves and activates the TRPC5 channel to participate in semaphorin 3A-induced neuronal growth cone collapse. *Proc. Natl. Acad. Sci.* **109**, 7888–7892.
- Karimi, K., Fortriede, J. D., Lotay, V. S., Burns, K. A., Wang, D. Z., Fisher, M. E., Pells, T. J., James-Zorn, C., Wang, Y., Ponferrada, V. G., et al. (2018). Xenbase: a genomic, epigenomic and transcriptomic model organism database. *Nucleic Acids Res.* **46**, D861–D868.
- Kashiwagi, H., Shiraga, M., Kato, H., Kamae, T., Yamamoto, N., Tadokoro, S., Kurata, Y., Tomiyama, Y. and Kanakura, Y. (2005). Negative regulation of platelet function by a secreted cell repulsive protein, semaphorin 3A. *Blood* **106**, 913–921.
- Keller, R., Davidson, L. A. and Shook, D. R.** (2003). How we are shaped: The biomechanics of gastrulation. *Differentiation* **71**, 171–205.
- Kerstein, P. C., Jacques-Fricke, B. T., Rengifo, J., Mogen, B. J., Williams, J. C., Gottlieb, P. A., Sachs, F. and Gomez, T. M. (2013). Mechanosensitive TRPC1 Channels Promote Calpain Proteolysis of Talin to Regulate Spinal Axon Outgrowth. *J. Neurosci.* **33**, 273–285.

- Kerstein, P. C., Patel, K. M. and Gomez, T. M.** (2017). Calpain-Mediated Proteolysis of Talin and FAK Regulates Adhesion Dynamics Necessary for Axon Guidance. *J. Neurosci.* **37**, 1568–1580.
- Kinbara, K., Goldfinger, L. E., Hansen, M., Chou, F.-L. and Ginsberg, M. H.** (2003). Ras GTPases: integrins' friends or foes? *Nat. Rev. Mol. Cell Biol.* **4**, 767–777.
- Klapholz, B. and Brown, N. H.** (2017). Talin – the master of integrin adhesions. *J. Cell Sci.* **130**, 2435–2446.
- Ko, J.-A., Akamatsu, Y., Yanai, R. and Nishida, T.** (2010). Effects of semaphorin 3A overexpression in corneal fibroblasts on the expression of adherens-junction proteins in corneal epithelial cells. *Biochem. Biophys. Res. Commun.* **396**, 781–786.
- Kolodkin, A. L., Matthes, D. J., O'Connor, T. P., Patel, N. H., Admon, A., Bentley, D. and Goodman, C. S.** (1992). Fasciclin IV: Sequence, expression, and function during growth cone guidance in the grasshopper embryo. *Neuron* **9**, 831–845.
- Koser, D. E., Moeendarbary, E., Hanne, J., Kuerten, S. and Franze, K.** (2015). CNS Cell Distribution and Axon Orientation Determine Local Spinal Cord Mechanical Properties. *Biophys. J.* **108**, 2137–2147.
- Koser, D. E., Thompson, A. J., Foster, S. K., Dwivedy, A., Pillai, E. K., Sheridan, G. K., Svoboda, H., Viana, M., Costa, L. da F., Guck, J., et al. (2016). Mechanosensing is critical for axon growth in the developing brain. *Nat. Neurosci.* **19**, 1592–1598.
- Koser, D. E., Moeendarbary, E., Kuerten, S. and Franze, K.** (2018). Predicting local tissue mechanics using immunohistochemistry. *bioRxiv* 358119.
- Lacroix, J. J., Botello-Smith, W. M. and Luo, Y.** (2018). Probing the gating mechanism of the mechanosensitive channel Piezo1 with the small molecule Yoda1. *Nat. Commun.* **9**, 2029.
- Lamoureux, P., Ruthel, G., Buxbaum, R. E. and Heidemann, S. R.** (2002). Mechanical tension can specify axonal fate in hippocampal neurons. *J. Cell Biol.* **159**, 499–508.
- Leipzig, N. D. and Shoichet, M. S.** (2009). The effect of substrate stiffness on adult neural stem cell behavior. *Biomaterials* **30**, 6867–6878.
- Lénárt, P., Petronczki, M., Steegmaier, M., Di Fiore, B., Lipp, J. J., Hoffmann, M., Rettig, W. J., Kraut, N. and Peters, J.-M. (2007). The Small-Molecule Inhibitor BI 2536 Reveals Novel Insights into Mitotic Roles of Polo-like Kinase 1. *Curr. Biol.* **17**, 304–315.

- Leung, L. C., Urbančič, V., Baudet, M.-L., Dwivedy, A., Bayley, T. G., Lee, A. C., Harris, W. A. and Holt, C. E.** (2013). Coupling of NF-protocadherin signaling to axon guidance by cue-induced translation. *Nat. Neurosci.* **16**, 166–173.
- Lewis, A. H. and Grandl, J.** (2015). Mechanical sensitivity of Piezo1 ion channels can be tuned by cellular membrane tension. *Elife* **4**, 622–626.
- Li, J., Hou, B., Tumova, S., Muraki, K., Bruns, A., Ludlow, M. J., Sedo, A., Hyman, A. J., McKeown, L., Young, R. S., et al. (2014). Piezo1 integration of vascular architecture with physiological force. *Nature* **515**, 279–282.
- Li, X., Han, L., Nookaew, I., Mannen, E., Silva, M. J., Almeida, M. and Xiong, J.** (2019). Stimulation of Piezo1 by mechanical signals promotes bone anabolism. *Elife* **8**, .
- Liang, G.-P., Xu, J., Cao, L., Zeng, Y.-H., Chen, B.-X., Yang, J., Zhang, Z.-W. and Kang, Y. (2019). Piezo1 induced apoptosis of type II pneumocytes during ARDS. *Respir. Res.* **20**, 118.
- Lindsey, B. W., Hall, Z. J., Heuzé, A., Joly, J.-S., Tropepe, V. and Kaslin, J.** (2018). The role of neuro-epithelial-like and radial-glia stem and progenitor cells in development, plasticity, and repair. *Prog. Neurobiol.* **170**, 99–114.
- Lins, M. P., Silva, E. C. O., Silva, G. R., Souza, S. T., Medeiros, N. C., Fonseca, E. J. S. and Smanioto, S.** (2018). Association between biomechanical alterations and migratory ability of semaphorin-3A-treated thymocytes. *Biochim. Biophys. Acta - Gen. Subj.* **1862**, 816–824.
- Livak, K. J. and Schmittgen, T. D.** (2001). Analysis of Relative Gene Expression Data Using Real-Time Quantitative PCR and the  $2^{-\Delta\Delta CT}$  Method. *Methods* **25**, 402–408.
- Lowery, L. A. and Vactor, D. Van** (2009). The trip of the tip: understanding the growth cone machinery. *Nat. Rev. Mol. Cell Biol.* **10**, 332–343.
- Lu, Y.-B., Franze, K., Seifert, G., Steinhauser, C., Kirchhoff, F., Wolburg, H., Guck, J., Janmey, P., Wei, E.-Q., Kas, J., et al. (2006). Viscoelastic properties of individual glial cells and neurons in the CNS. *Proc. Natl. Acad. Sci.* **103**, 17759–17764.
- Luarte, A., Cornejo, V. H., Bertin, F., Gallardo, J. and Couve, A.** (2018). The axonal endoplasmic reticulum: One organelle-many functions in development, maintenance, and plasticity. *Dev. Neurobiol.* **78**, 181–208.
- Luo, Y., Raible, D. and Raper, J. A.** (1993). Collapsin: A protein in brain that induces the collapse and paralysis of neuronal growth cones. *Cell* **75**, 217–227.

- MacDonald, R. B., Randlett, O., Oswald, J., Yoshimatsu, T., Franze, K. and Harris, W. A.** (2015). Müller glia provide essential tensile strength to the developing retina. *J. Cell Biol.* **210**, 1075–1083.
- Majkut, S., Idema, T., Swift, J., Krieger, C., Liu, A. and Discher, D. E.** (2013). Heart-Specific Stiffening in Early Embryos Parallels Matrix and Myosin Expression to Optimize Beating. *Curr. Biol.* **23**, 2434–2439.
- Mann, F., Ray, S., Harris, W. A. and Holt, C. E.** (2002). Topographic Mapping in Dorsoventral Axis of the *Xenopus* Retinotectal System Depends on Signaling through Ephrin-B Ligands. *Neuron* **35**, 461–473.
- Marzioni, D., Tamagnone, L., Capparuccia, L., Marchini, C., Amici, A., Todros, T., Bischof, P., Neidhart, S., Grenningloh, G. and Castellucci, M. (2004). Restricted innervation of uterus and placenta during pregnancy: Evidence for a role of the repelling signal Semaphorin 3A. *Dev. Dyn.* **231**, 839–848.
- McFarlane, S. and Lom, B.** (2012). The *Xenopus* retinal ganglion cell as a model neuron to study the establishment of neuronal connectivity. *Dev. Neurobiol.* **72**, 520–36.
- McFarlane, S., McNeill, L. and Holt, C. E.** (1995). FGF signaling and target recognition in the developing *xenopus* visual system. *Neuron* **15**, 1017–1028.
- McHugh, B. J., Buttery, R., Lad, Y., Banks, S., Haslett, C. and Sethi, T.** (2010). Integrin activation by Fam38A uses a novel mechanism of R-Ras targeting to the endoplasmic reticulum. *J. Cell Sci.* **123**, 51–61.
- Medeiros, N. A., Burnette, D. T. and Forscher, P.** (2006). Myosin II functions in actin-bundle turnover in neuronal growth cones. *Nat. Cell Biol.* **8**, 216–226.
- Miller, C. J. and Davidson, L. A.** (2013). The interplay between cell signalling and mechanics in developmental processes. *Nat. Rev. Genet.* **14**, 733–744.
- Moeendarbary, E., Weber, I. P., Sheridan, G. K., Koser, D. E., Soleman, S., Haenzi, B., Bradbury, E. J., Fawcett, J. and Franze, K. (2017). The soft mechanical signature of glial scars in the central nervous system. *Nat. Commun.* **8**, 14787.
- Moore, S. W., Tessier-Lavigne, M. and Kennedy, T. E.** (2007). Netrins and Their receptors. In *Axon Growth and Guidance*, pp. 17–31. New York, NY: Springer New York.
- Moshayedi, P., da F Costa, L., Christ, A., Lacour, S. P., Fawcett, J., Guck, J. and Franze, K.** (2010). Mechanosensitivity of astrocytes on optimized polyacrylamide gels analyzed by quantitative morphometry. *J. Phys. Condens. Matter* **22**, 194114.

- Mughal, B. B., Leemans, M., Spirhanzlova, P., Demeneix, B. and Fini, J.-B.** (2018). Reference gene identification and validation for quantitative real-time PCR studies in developing *Xenopus laevis*. *Sci. Rep.* **8**, 496.
- Myers, J. P., Santiago-Medina, M. and Gomez, T. M.** (2011). Regulation of axonal outgrowth and pathfinding by integrin-ecm interactions. *Dev. Neurobiol.* **71**, 901–923.
- Needham, D. and Nunn, R. S.** (1990). Elastic deformation and failure of lipid bilayer membranes. *Biophys. J.* **58**, 997–1009.
- Nicholson, C. and Tao, L.** (1993). Hindered diffusion of high molecular weight compounds in brain extracellular microenvironment measured with integrative optical imaging. *Biophys. J.* **65**, 2277–2290.
- Nieuwkoop, P. D. and Faber, J.** (1958). Normal Table of *Xenopus Laevis* (Daudin). *Copeia* **1958**,.
- Nieuwkoop, P. D. (Pieter D. . and Faber, J.** (1994). Normal table of *Xenopus laevis* (Daudin) : a systematical and chronological survey of the development from the fertilized egg till the end of metamorphosis. Garland Pub.
- Nishiyama, M., Hoshino, A., Tsai, L., Henley, J. R., Goshima, Y., Tessier-Lavigne, M., Poo, M. M. and Hong, K.** (2003). Cyclic AMP/GMP-dependent modulation of Ca<sup>2+</sup> channels sets the polarity of nerve growth-cone turning. *Nature* **423**,.
- Nishiyama, M., Von Schimmelmann, M. J., Togashi, K., Findley, W. M. and Hong, K.** (2008). Membrane potential shifts caused by diffusible guidance signals direct growth-cone turning. *Nat. Neurosci.* **11**,.
- Nonomura, K., Lukacs, V., Sweet, D. T., Goddard, L. M., Kanie, A., Whitwam, T., Ranade, S. S., Fujimori, T., Kahn, M. L. and Patapoutian, A. (2018). Mechanically activated ion channel PIEZO1 is required for lymphatic valve formation. *Proc. Natl. Acad. Sci. U. S. A.* **115**,.
- Norsk, P., Damgaard, M., Petersen, L., Gybel, M., Pump, B., Gabrielsen, A. and Christensen, N. J. (2006). Vasorelaxation in space. *Hypertension* **47**,.
- Nourse, J. L. and Pathak, M. M.** (2017). How cells channel their stress: Interplay between Piezo1 and the cytoskeleton. *Semin. Cell Dev. Biol.* **71**,.
- Nugent, A. A., Kolpak, A. L. and Engle, E. C.** (2012). Human disorders of axon guidance. *Curr. Opin. Neurobiol.* **22**,.

- O'Neill, P., McCole, R. B. and Baker, C. V. H.** (2007). A molecular analysis of neurogenic placode and cranial sensory ganglion development in the shark, *Scyliorhinus canicula*. *Dev. Biol.* **304**,.
- Oganov, V. S. and Bogomolov, V. V.** (2011). The human skeletal system in weightlessness: A review of research data, hypotheses, and the possibility of predicting the state in long-term (Interplanetary) missions. *Hum. Physiol.* **37**, 768–776.
- Ohara, P. T. and Buck, R. C.** (1979). Contact guidance in vitro. *Exp. Cell Res.* **121**, 235–249.
- Ohyama, K., Tan-Takeuchi, K., Kutsche, M., Schachner, M., Uyemura, K. and Kawamura, K.** (2004). Neural Cell Adhesion Molecule L1 Is Required for Fasciculation and Routing of Thalamocortical Fibres and Corticothalamic Fibres. *Neurosci. Res.* **48**, 471–475.
- Osborne, N. J., Begbie, J., Chilton, J. K., Schmidt, H. and Eickholt, B. J.** (2005). Semaphorin/neuropilin signaling influences the positioning of migratory neural crest cells within the hindbrain region of the chick. *Dev. Dyn.* **232**,.
- Pasterkamp, R. J. and Giger, R. J.** (2009). Semaphorin function in neural plasticity and disease. *Curr. Opin. Neurobiol.* **19**, 263–274.
- Pathak, M. M., Nourse, J. L., Tran, T., Hwe, J., Arulmoli, J., Le, D. T. T., Bernardis, E., Flanagan, L. A. and Tombola, F.** (2014). Stretch-activated ion channel Piezo1 directs lineage choice in human neural stem cells. *Proc. Natl. Acad. Sci. U. S. A.* **111**, 16148–53.
- Peyronnet, R., Tran, D., Girault, T. and Frachisse, J.-M.** (2014). Mechanosensitive channels: feeling tension in a world under pressure. *Front. Plant Sci.* **5**,.
- Piper, M., Salih, S., Weinl, C., Holt, C. E. and Harris, W. A.** (2005). Endocytosis-dependent desensitization and protein synthesis-dependent resensitization in retinal growth cone adaptation. *Nat. Neurosci.* **8**,.
- Piper, M., Anderson, R., Dwivedy, A., Weinl, C., van Horck, F., Leung, K. M., Cogill, E. and Holt, C.** (2006). Signaling Mechanisms Underlying Slit2-Induced Collapse of *Xenopus* Retinal Growth Cones. *Neuron* **49**, 215–228.
- Plump, A. S., Erskine, L., Sabatier, C., Brose, K., Epstein, C. J., Goodman, C. S., Mason, C. A. and Tessier-Lavigne, M.** (2002). Slit1 and Slit2 cooperate to prevent premature midline crossing of retinal axons in the mouse visual system. *Neuron* **33**, 219–232.

- Qin, G., Liao, G., Baudry, M. and Bi, X.** (2010). Role of calpain-mediated p53 truncation in semaphorin 3A-induced axonal growth regulation. *Proc. Natl. Acad. Sci. U. S. A.* **107**,.
- Rana, A. A., Collart, C., Gilchrist, M. J. and Smith, J. C.** (2006). Defining synphenotype groups in *Xenopus tropicalis* by use of antisense morpholino oligonucleotides. *PLoS Genet.* **2**,.
- Ranade, S. S., Qiu, Z., Woo, S.-H., Hur, S. S., Murthy, S. E., Cahalan, S. M., Xu, J., Mathur, J., Bandell, M., Coste, B., et al. (2014). Piezo1, a mechanically activated ion channel, is required for vascular development in mice. *Proc. Natl. Acad. Sci.* **111**, 10347–10352.
- Ranade, S. S., Syeda, R. and Patapoutian, A.** (2015). Mechanically Activated Ion Channels. *Neuron* **87**,.
- Retailleau, K., Duprat, F., Arhatte, M., Ranade, S. S., Peyronnet, R., Martins, J. R., Jodar, M., Moro, C., Offermanns, S., Feng, Y., et al. (2015). Piezo1 in Smooth Muscle Cells Is Involved in Hypertension-Dependent Arterial Remodeling. *Cell Rep.* **13**, 1161–1171.
- Rheinlaender, J., Dimitracopoulos, A., Wallmeyer, B., Kronenberg, N. M., Chalut, K. J., Gather, M. C., Betz, T., Charras, G. and Franze, K. (2019). Cortical cell stiffness is independent of substrate mechanics. *bioRxiv* 829614.
- Ridone, P., Pandzic, E., Vassalli, M., Cox, C. D., Macmillan, A., Gottlieb, P. A. and Martinac, B.** (2019). Disruption of membrane cholesterol organization impairs the concerted activity of PIEZO1 channel clusters. *bioRxiv* 604488.
- Ruoslahti, E.** (1996). Brain extracellular matrix. *Glycobiology* **6**, 489–492.
- Sack, I., Beierbach, B., Hamhaber, U., Klatt, D. and Braun, J.** (2008). Non-invasive measurement of brain viscoelasticity using magnetic resonance elastography. *NMR Biomed.* **21**, 265–271.
- Saha, K., Keung, A. J., Irwin, E. F., Li, Y., Little, L., Schaffer, D. V. and Healy, K. E. (2008). Substrate modulus directs neural stem cell behavior. *Biophys. J.* **95**,.
- Sakisaka, T.** (2005). Cell adhesion molecules in the CNS. *J. Cell Sci.* **118**, 5407–5410.
- Saotome, K., Murthy, S. E., Kefauver, J. M., Whitwam, T., Patapoutian, A. and Ward, A. B. (2018). Structure of the mechanically activated ion channel Piezo1. *Nature* **554**,.
- Scarcelli, G. and Yun, S. H.** (2012). In vivo Brillouin optical microscopy of the human eye. *Opt. Express* **20**, 9197.
- Schäfer, M. K. E. and Frotscher, M.** (2012). Role of L1CAM for axon sprouting and branching. *Cell Tissue Res.* **349**, 39–48.

Segel, M., Neumann, B., Hill, M. F. E., Weber, I. P., Viscomi, C., Zhao, C., Young, A., Agle, C. C., Thompson, A. J., Gonzalez, G. A., et al. (2019). Niche stiffness underlies the ageing of central nervous system progenitor cells. *Nature* 573, 130–134.

Serini, G., Valdembri, D., Zanivan, S., Morterra, G., Burkhardt, C., Caccavari, F., Zammataro, L., Primo, L., Tamagnone, L., Logan, M., et al. (2003). Class 3 semaphorins control vascular morphogenesis by inhibiting integrin function. *Nature* 424, 391–397.

**Serwane, F., Mongera, A., Rowghanian, P., Kealhofer, D. A., Lucio, A. A., Hockenbery, Z. M. and Campàs, O.** (2017). In vivo quantification of spatially varying mechanical properties in developing tissues. *Nat. Methods* 14, 181–186.

Session, A. M., Uno, Y., Kwon, T., Chapman, J. A., Toyoda, A., Takahashi, S., Fukui, A., Hikosaka, A., Suzuki, A., Kondo, M., et al. (2016). Genome evolution in the allotetraploid frog *Xenopus laevis*. *Nature* 538,.

Shamah, S. M., Lin, M. Z., Goldberg, J. L., Estrach, S., Sahin, M., Hu, L., Bazalakova, M., Neve, R. L., Corfas, G., Debant, A., et al. (2001). EphA Receptors Regulate Growth Cone Dynamics through the Novel Guanine Nucleotide Exchange Factor Ephexin. *Cell* 105, 233–244.

**Shewan, D., Dwivedy, A., Anderson, R. and Holt, C. E.** (2002). Age-related changes underlie switch in netrin-1 responsiveness as growth cones advance along visual pathway. *Nat. Neurosci.* 5, 955–962.

Shigeoka, T., Jung, H., Jung, J., Turner-Bridger, B., Ohk, J., Lin, J. Q., Amieux, P. S., Holt, C. E., Aakalu, G., Smith, W. B., et al. (2016). Dynamic Axonal Translation in Developing and Mature Visual Circuits. *Cell* 166, 181–92.

Shim, S., Goh, E. L., Ge, S., Sailor, K., Yuan, J. P., Roderick, H. L., Bootman, M. D., Worley, P. F., Song, H. and Ming, G. (2005). XTRPC1-dependent chemotropic guidance of neuronal growth cones. *Nat. Neurosci.* 8, 730–735.

**Shimamura, K., Hirano, S., McMahon, A. P. and Takeichi, M.** (1994). Wnt-1-dependent regulation of local E-cadherin and  $\alpha$ N-catenin expression in the embryonic mouse brain. *Development* 120,.

Sibonga, J. D., Cavanagh, P. R., Lang, T. F., LeBlanc, A. D., Schneider, V. S., Shackelford, L. C., Smith, S. M. and Vico, L. (2007). Adaptation of the skeletal system during long-duration spaceflight. *Clin. Rev. Bone Miner. Metab.* 5,.

- Siechen, S., Yang, S., Chiba, A. and Saif, T.** (2009). Mechanical tension contributes to clustering of neurotransmitter vesicles at presynaptic terminals. *Proc. Natl. Acad. Sci.* **106**, 12611–12616.
- Simitzi, C., Ranella, A. and Stratakis, E.** (2017). Controlling the morphology and outgrowth of nerve and neuroglial cells: The effect of surface topography. *Acta Biomater.* **51**,.
- Singh, T., Meena, R. and Kumar, A.** (2009). Effect of sodium sulfate on the gelling behavior of agarose and water structure inside the gel networks. *J. Phys. Chem. B* **113**,.
- Šmít, D., Fouquet, C., Pincet, F., Zapotocky, M. and Trembleau, A.** (2017). Axon tension regulates fasciculation/defasciculation through the control of axon shaft zippering. *Elife* **6**,.
- Smith, G. M. and Gallo, G.** (2018). The role of mitochondria in axon development and regeneration. *Dev. Neurobiol.* **78**,.
- Song, H., Ming, G. and Poo, M.** (1997). cAMP-induced switching in turning direction of nerve growth cones. *Nature* **388**, 275–279.
- Stone, K. E. and Sakaguchi, D. S.** (1996). Perturbation of the Developing *Xenopus* Retinotectal Projection Following Injections of Antibodies against  $\beta$ 1 Integrin Receptors and N-cadherin. *Dev. Biol.* **180**, 297–310.
- Sugimoto, A., Miyazaki, A., Kawarabayashi, K., Shono, M., Akazawa, Y., Hasegawa, T., Ueda-Yamaguchi, K., Kitamura, T., Yoshizaki, K., Fukumoto, S., et al. (2017). Piezo type mechanosensitive ion channel component 1 functions as a regulator of the cell fate determination of mesenchymal stem cells. *Sci. Rep.* **7**,.
- Sun, W., Chi, S., Li, Y., Ling, S., Tan, Y., Xu, Y., Jiang, F., Li, J., Liu, C., Zhong, G., et al. (2019). The mechanosensitive Piezo1 channel is required for bone formation. *Elife* **8**,.
- Swiercz, J. M., Kuner, R., Behrens, J. and Offermanns, S.** (2002). Plexin-B1 Directly Interacts with PDZ-RhoGEF/LARG to Regulate RhoA and Growth Cone Morphology. *Neuron* **35**, 51–63.
- Syeda, R., Xu, J., Dubin, A. E., Coste, B., Mathur, J., Huynh, T., Matzen, J., Lao, J., Tully, D. C., Engels, I. H., et al. (2015). Chemical activation of the mechanotransduction channel Piezo1. *Elife* **4**,.
- Syeda, R., Florendo, M. N., Cox, C. D., Kefauver, J. M., Santos, J. S., Martinac, B. and Patapoutian, A. (2016). Piezo1 Channels Are Inherently Mechanosensitive. *Cell Rep.* **17**, 1739–1746.

- Tessier-Lavigne, M. and Goodman, C. S.** (1996). The molecular biology of axon guidance. *Science* (80-. ). **274**,.
- Thompson, D. W.** (1917). *On growth and form*. Cambridge, England: Cambridge University Press.
- Thompson, A. J.** (2018). In vivo and in vitro guidance of developing neurons by mechanical cues.
- Thompson, A. J., Pillai, E. K., Dimov, I. B., Foster, S. K., Holt, C. E. and Franze, K.** (2019). Rapid changes in tissue mechanics regulate cell behaviour in the developing embryonic brain. *Elife* **8**,.
- Togashi, K., von Schimmelmann, M. J., Nishiyama, M., Lim, C. S., Yoshida, N., Yun, B., Molday, R. S., Goshima, Y. and Hong, K. (2008). Cyclic GMP-Gated CNG Channels Function in Semaphorin 3A-Induced Growth Cone Repulsion. *Neuron* **58**,.
- Tojima, T., Hines, J. H., Henley, J. R. and Kamiguchi, H.** (2011). Second messengers and membrane trafficking direct and organize growth cone steering. *Nat. Rev. Neurosci.* **12**, 191–203.
- Toyofuku, T., Yoshida, J., Sugimoto, T., Zhang, H., Kumanogoh, A., Hori, M. and Kikutani, H. (2005). FARP2 triggers signals for Semaphorin 3A-mediated axonal repulsion. *Nat. Neurosci.* **8**,.
- Tran, T. S., Kolodkin, A. L. and Bharadwaj, R.** (2007). Semaphorin Regulation of Cellular Morphology. *Annu. Rev. Cell Dev. Biol.* **23**,.
- Trousse, F., Martí, E., Gruss, P., Torres, M. and Bovolenta, P.** (2001). Control of retinal ganglion cell axon growth: A new role for Sonic hedgehog. *Development* **128**,.
- Tsai, F.-C., Kuo, G.-H., Chang, S.-W. and Tsai, P.-J.** (2015). Ca<sup>2+</sup> Signaling in Cytoskeletal Reorganization, Cell Migration, and Cancer Metastasis. *Biomed Res. Int.* **2015**, 1–13.
- Turner, L. J., Nicholls, S. and Hall, A.** (2004). The Activity of the Plexin-A1 Receptor Is Regulated by Rac. *J. Biol. Chem.* **279**, 33199–33205.
- van Horck, F. P. G., Weigl, C. and Holt, C. E.** (2004). Retinal axon guidance: novel mechanisms for steering. *Curr. Opin. Neurobiol.* **14**, 61–6.
- Villegas, G. and Tufro, A.** (2002). Ontogeny of semaphorins 3A and 3F and their receptors neuropilins 1 and 2 in the kidney. *Gene Expr. Patterns* **2**,.
- Volkers, L., Mechiouki, Y. and Coste, B.** (2014). Piezo channels: from structure to function. *Pflügers Arch. Eur. J. Physiol.* **467**,.

- Walz, A., Anderson, R. B., Irie, A., Chien, C. Bin and Holt, C. E.** (2002). Chondroitin sulfate disrupts axon pathfinding in the optic tract and alters growth cone dynamics. *J. Neurobiol.* **53**,.
- Wang, G. X. and Poo, M.-M.** (2005). Requirement of TRPC channels in netrin-1-induced chemotropic turning of nerve growth cones. *Nature* **434**, 898–904.
- Wang, Y., Chi, S., Guo, H., Li, G., Wang, L., Zhao, Q., Rao, Y., Zu, L., He, W. and Xiao, B.** (2018). A lever-like transduction pathway for long-distance chemical- and mechano-gating of the mechanosensitive Piezo1 channel. *Nat. Commun.* **9**,.
- Weber, I. P., Ramos, A. P., Strzyz, P. J., Leung, L. C., Young, S. and Norden, C.** (2014). Mitotic Position and Morphology of Committed Precursor Cells in the Zebrafish Retina Adapt to Architectural Changes upon Tissue Maturation. *Cell Rep.* **7**,.
- Weber, I. P., Yun, S. H., Scarcelli, G. and Franze, K.** (2017). The role of cell body density in ruminant retina mechanics assessed by atomic force and Brillouin microscopy. *Phys. Biol.* **14**,.
- Weiss, P.** (1934). In vitro experiments on the factors determining the course of the outgrowing nerve fiber. *J. Exp. Zool.* **68**, 393–448.
- Weiss, P.** (1945). Experiments on cell and axon orientation in vitro: The role of colloidal exudates in tissue organization. *J. Exp. Zool.* **100**, 353–386.
- Williams, D., Kuipers, A., Mukai, C. and Thirsk, R.** (2009). Acclimation during space flight: Effects on human physiology. *CMAJ* **180**,.
- Wizenmann, A., Brunet, I., Lam, J. S. Y., Sonnier, L., Beurdeley, M., Zarbalis, K., Weisenhorn-Vogt, D., Weinl, C., Dwivedy, A., Joliot, A., et al. (2009). Extracellular Engrailed Participates in the Topographic Guidance of Retinal Axons In Vivo. *Neuron* **64**,.
- Wright, D. E., White, F. A., Gerfen, R. W., Silos-Santiago, I. and Snider, W.** (1995). The guidance molecule Semaphorin III is expressed in regions of spinal cord and periphery avoided by growing sensory axons. *J. Comp. Neurol.* **361**, 321–333.
- Wu, K. Y., Hengst, U., Cox, L. J., Macosko, E. Z., Jeromin, A., Urquhart, E. R. and Jaffrey, S. R. (2005). Local translation of RhoA regulates growth cone collapse. *Nature* **436**, 1020–1024.
- Wu, J., Lewis, A. H. and Grandl, J.** (2017). Touch, Tension, and Transduction – The Function and Regulation of Piezo Ion Channels. *Trends Biochem. Sci.* **42**, 57–71.
- Yang, J. L. J., Bertolesi, G. E., Dueck, S., Hehr, C. L. and McFarlane, S.** (2019). The expression of key guidance genes at a forebrain axon turning point is maintained by

distinct fgfr isoforms but a common downstream signal transduction mechanism. *eNeuro* **6**,.

**Yazdani, U. and Terman, J. R.** (2006). The semaphorins. *Genome Biol.* **7**, 211.

Zhao, Q., Zhou, H., Chi, S., Wang, Y., Wang, J., Geng, J., Wu, K., Liu, W., Zhang, T., Dong, M.-Q., et al. (2018). Structure and mechanogating mechanism of the Piezo1 channel. *Nature* **554**, 487–492.

**Zhao, Q., Zhou, H., Li, X. and Xiao, B.** (2019). The mechanosensitive Piezo1 channel: a three-bladed propeller-like structure and a lever-like mechanogating mechanism. *FEBS J.* **286**, 2461–2470.

**Zheng, J. Q.** (2000). Turning of nerve growth cones induced by localized increases in intracellular calcium ions. *Nature* **403**,.

**Zimmer, G., Schanuel, S. M., Bürger, S., Weth, F., Steinecke, A., Bolz, J. and Lent, R.** (2010). Chondroitin sulfate acts in concert with semaphorin 3A to guide tangential migration of cortical interneurons in the ventral telencephalon. *Cereb. Cortex* **20**,.

**Zivraj, K. H., Tung, Y. C. L., Piper, M., Gumy, L., Fawcett, J. W., Yeo, G. S. H. and Holt, C. E.** (2010). Subcellular profiling reveals distinct and developmentally regulated repertoire of growth cone mRNAs. *J. Neurosci.* **30**,.